

71-3669

HERSHBERGER, Robert Lee, 1941-
PROPERTIES OF ELECTROMAGNETIC TRANSITIONS
IN FLUORINE-20 AND IRON-55.

University of Arizona, Ph.D., 1970
Physics, nuclear

University Microfilms, Inc., Ann Arbor, Michigan

© COPYRIGHTED

BY

ROBERT LEE HERSHBERGER

1971

PROPERTIES OF ELECTROMAGNETIC TRANSITIONS
IN FLUORINE-20 AND IRON-55

by

Robert Lee Hershberger

A Dissertation Submitted to the Faculty of the
DEPARTMENT OF PHYSICS
In Partial Fulfillment of the Requirements
For the Degree of
DOCTOR OF PHILOSOPHY
In the Graduate College
THE UNIVERSITY OF ARIZONA

1 9 7 0

THE UNIVERSITY OF ARIZONA

GRADUATE COLLEGE

I hereby recommend that this dissertation prepared under my direction by Robert Lee Hershberger entitled Properties of Electromagnetic Transitions in Fluorine-20 and Iron-55 be accepted as fulfilling the dissertation requirement of the degree of Doctor of Philosophy

M. J. Norvaluc
Dissertation Director

7/2/70
Date

After inspection of the final copy of the dissertation, the following members of the Final Examination Committee concur in its approval and recommend its acceptance:*

<u><i>John G. Lewitt</i></u>	<u>7/2/70</u>
<u><i>Roy M. Emrick</i></u>	<u>7-3-70</u>
<u><i>Chay-jun Kim</i></u>	<u>7-3-70</u>
<u><i>Arnold C. Sherwood</i></u>	<u>7-3-70</u>
<u> </u>	<u> </u>

*This approval and acceptance is contingent on the candidate's adequate performance and defense of this dissertation at the final oral examination. The inclusion of this sheet bound into the library copy of the dissertation is evidence of satisfactory performance at the final examination.

STATEMENT BY AUTHOR

This dissertation has been submitted in partial fulfillment of requirements for an advanced degree at The University of Arizona and is deposited in the University Library to be made available to borrowers under rules of the Library.

Brief quotations from this dissertation are allowable without special permission, provided that accurate acknowledgment of source is made. Requests for permission for extended quotation from or reproduction of this manuscript in whole or in part may be granted by the copyright holder.

SIGNED: Robert Lee Hershberger

ACKNOWLEDGMENTS

The author is deeply indebted to Professor Douglas J. Donahue for suggesting this research, and for his advice and assistance in all phases of the dissertation. He is also thankful to Professors John D. McCullen and Lawrence C. McIntyre, Jr. for many helpful discussions during the course of this work. In addition, the author wishes to acknowledge the help of Dr. M. J. Wozniak, Jr.; he was a full collaborator in much of the work reported here. The author is also very grateful to Drs. J. E. Cummings and W. S. Smith, and Messrs. C. R. Ceccon, P. L. Carson, A. S. Goodman, and D. L. Barker, all of whom assisted in recording data and participated in many helpful discussions concerning various phases of this research.

TABLE OF CONTENTS

	Page
LIST OF TABLES	vii
LIST OF ILLUSTRATIONS	viii
ABSTRACT	x
I INTRODUCTION	1
II THE DOPPLER-SHIFT ATTENUATION METHOD	6
III EXPERIMENTAL DETAILS	13
Solid Backing	13
The Two-Target Chamber	15
Target Preparation	24
Data Taking and Reduction	28
Analysis of Errors	29
The Error, $\delta(\tau_F)$, Due to $\delta(F_{\text{expt}})$	32
The Error, $\delta(\tau_T)$, Due to Uncertainties in Target Thickness	32
The Error, $\delta(\tau_{sp})$, Due to Uncertainties in Stopping Power	32
Gas Backing	34
The Gas Chamber	38
Target Preparation	38
Analysis of Errors	41
IV RESULTS	48
Excitation Energies in ^{20}F	48
Branching Ratios in ^{20}F	53
Mean Lives of Excited States in ^{20}F	53
Mean Lives and Branching Ratios of Excited States in ^{56}Fe	59
V DISCUSSION OF RESULTS	67
The Extreme Single-Particle Model	70

TABLE OF CONTENTS--Continued

	Page
Measurements on ^{20}F	72
The 0.66-MeV Level	74
The 0.82-MeV Level	74
The 0.98-MeV Level	75
The 1.06-MeV Level	75
The 1.31-MeV Level	76
Measurements on ^{56}Fe	76
VI SUMMARY AND CONCLUSION	85
APPENDIX A: THE CALCULATION OF $\langle \hat{r} \rangle_{\gamma}$	88
APPENDIX B: A COMPARISON OF THE FAST-SLOW AND SLOW-FAST COINCIDENCE SYSTEMS	96
APPENDIX C: A DESCRIPTION OF THE "AND", "OR" AND "ROUTING- TO-MEMORY" BOXES	100
The Routing-to-Memory Box	100
The "AND" and "OR" Boxes	111
APPENDIX D: THE MEAN LIFE CALCULATION FOR A LEVEL WHICH IS POPULATED BY TRANSITIONS FROM ABOVE	117
LIST OF REFERENCES	121

LIST OF TABLES

Table	Page
I	Gamma-ray energies and relative intensities used in calculating relative photo peak efficiency curves 19
II	Target materials and evaporation parameters 27
III	Calculated deviations in the average initial recoil energy, $\langle E_Y \rangle_0$, and average relative full shift, $\Delta \langle E_Y \rangle_0 / E_0$, due to deviations in the parameters of the full shift calculation 31
IV	Energies of some levels in ^{20}F 52
V	Branching ratios of some levels in ^{20}F 54
VI	Doppler shifts and mean lives in ^{20}F 57
VII	Comparison of present results with those published recently . 60
VIII	Doppler shifts and mean lives in ^{55}Fe 65
IX	A summary of M1 and E2 reduced transition probabilities and Weisskopf estimates deduced from experimental measurements 79
X	A comparison of energies, multipole mixing ratios, and reduced E2 transition probabilities for the low-lying levels in ^{63}Cu and ^{55}Fe 81
XI	Comparisons of the mean lives obtained from the results of measurements on ^{55}Fe with those predicted by the unified model 83
XII	Measured and corrected distances traversed by a γ ray in the detector crystal 94
XIII	Results of the numerical integration for the low and high energy limits 95
XIV	Signals with their routing and logical voltage levels 105

LIST OF ILLUSTRATIONS

Figure	Page
1. F_{calc} vs. τ for a solid target with a solid backing	12
2. Experimental arrangement of the two-target chamber	16
3. Photo-peak relative efficiency vs. γ -ray energy	18
4. Block diagram of electronics used with two-target chamber	22
5. Electron gun configuration	26
6. Effects of stopping power uncertainties on F_{calc} for a solid target with a solid backing	33
7. F_{calc} vs. τ for a solid target with a gas backing	36
8. F_{calc} vs. τ for several pressures in the gas backing	37
9. Experimental arrangement of the gas-backing chamber	39
10. $[F_{\text{max}} - F]_{\text{calc}}$ vs. τ for a solid target with a gas backing	44
11. Effects of stopping power uncertainties in the target on $[F_{\text{max}} - F]_{\text{calc}}$	45
12. Effects of stopping power uncertainties in the gas backing on $[F_{\text{max}} - F]_{\text{calc}}$	46
13. Proton spectrum from the $^{19}\text{F}(d,p)^{20}\text{F}$ reaction	49
14. γ -ray spectra from the $^{19}\text{F}(d,p)^{20}\text{F}$ reaction	51
15. Coincidence spectra from the $^{19}\text{F}(d,p)^{20}\text{F}$ reaction	55
16. Proton spectrum from the $^{54}\text{Fe}(d,p)^{55}\text{Fe}$ reaction	61
17. Coincidence spectra from the $^{54}\text{Fe}(d,p)^{55}\text{Fe}$ reaction	62
18. Coincidence spectra from the $^{54}\text{Fe}(d,p)^{55}\text{Fe}$ reaction showing shifts of several transitions	63
19. Energy level diagram for the low-lying states in ^{20}F	73

LIST OF ILLUSTRATIONS--Continued

Figure	Page
20. Energy level diagram for the low-lying states in ^{56}Fe	77
21. A three-dimensional view of the γ -ray detector crystal	90
22. An enlarged top view of the γ -ray detector crystal	92
23. A block diagram of the fast-slow and slow-fast coincidence systems	97
24. Basic logic and logical symbols	101
25. Functional block diagram of routing-to-memory box	102
26. Signal block diagram of routing-to-memory box	104
27. Logic diagram of digital gain conversion selector	106
28. Logic diagram of block address selector	107
29. Logic diagram of external routing selector section I	109
30. Logic diagram of external routing selector section II	110
31. Logic diagrams of the four 2-input AND circuits and the 5-input OR circuit	112
32. Schematic diagrams of a logic-level converter and two integrated circuits	113
33. Schematic diagrams of the AND, OR, and routing-to-memory boxes.	115
34. Top view of circuit boards for the AND, OR, and routing-to-memory boxes	116

ABSTRACT

We have used a Ge(Li) detector in the coincidence version of the Doppler-shift attenuation method to obtain the following information concerning the mean lives of the low-lying states in ^{20}F and ^{56}Fe :

States in ^{20}F

$$\tau(0.66 \text{ MeV}) = (3.57 \begin{smallmatrix} + 0.73 \\ - 0.78 \end{smallmatrix}) \times 10^{-13} \text{ sec}$$

$$\tau(0.82 \text{ MeV}) \geq 4.4 \times 10^{-12} \text{ sec}$$

$$\tau(0.98 \text{ MeV}) = (1.28 \begin{smallmatrix} + 0.62 \\ - 0.41 \end{smallmatrix}) \times 10^{-12} \text{ sec}$$

$$\tau(1.06 \text{ MeV}) \leq 9.2 \times 10^{-14} \text{ sec}$$

$$\tau(1.31 \text{ MeV}) = (1.11 \begin{smallmatrix} + 0.41 \\ - 0.29 \end{smallmatrix}) \times 10^{-12} \text{ sec}$$

$$\tau(2.04 \text{ MeV}) \leq 3.8 \times 10^{-14} \text{ sec}$$

$$\tau(2.19 \text{ MeV}) \leq 4.6 \times 10^{-14} \text{ sec}$$

$$\tau(2.96 \text{ MeV}) \leq 6.2 \times 10^{-14} \text{ sec}$$

$$\tau(3.49 \text{ MeV}) \leq 4.7 \times 10^{-14} \text{ sec}$$

$$\tau(3.53 \text{ MeV}) \leq 3.2 \times 10^{-14} \text{ sec}$$

States in ^{56}Fe

$$\tau(0.41 \text{ MeV}) = (6.7 \begin{smallmatrix} + 10.1 \\ - 3.8 \end{smallmatrix}) \times 10^{-13} \text{ sec}$$

$$\tau(0.93 \text{ MeV}) = (9.8 \begin{smallmatrix} + 7.9 \\ - 3.7 \end{smallmatrix}) \times 10^{-13} \text{ sec}$$

$$\tau(1.32 \text{ MeV}) = (8.7 \begin{smallmatrix} + 9.1 \\ - 4.0 \end{smallmatrix}) \times 10^{-13} \text{ sec}$$

$$\tau(1.41 \text{ MeV}) > 1.0 \times 10^{-12} \text{ sec}$$

$$\tau(1.92 \text{ MeV}) < 3.2 \times 10^{-14} \text{ sec}$$

$$\tau(2.05 \text{ MeV}) < 2.8 \times 10^{-14} \text{ sec}$$

$$\tau(2.15 \text{ MeV}) = (2.8 \begin{smallmatrix} + 1.5 \\ - 0.9 \end{smallmatrix}) \times 10^{-14} \text{ sec}$$

$$\tau(2.21 \text{ MeV}) = (1.05 \begin{smallmatrix} + 1.53 \\ - 0.75 \end{smallmatrix}) \times 10^{-13} \text{ sec}$$

$$\tau(2.30 \text{ MeV}) \approx 1.1 \times 10^{-13} \text{ sec}$$

$$\tau(2.47 \text{ MeV}) = (2.5 \begin{smallmatrix} + 1.5 \\ - 0.8 \end{smallmatrix}) \times 10^{-14} \text{ sec}$$

$$\tau(2.59 \text{ MeV}) = (3.6 \begin{smallmatrix} + 2.1 \\ - 1.2 \end{smallmatrix}) \times 10^{-14} \text{ sec}$$

Slowing down in the target as well as stopping in the backing material is considered. The development of a method which uses a gas as the slowing-down material for the recoiling nucleus and its use as a check on the mean lives of the first three levels in ^{55}Fe is reported.

From our mean life results we have deduced the reduced matrix elements for electromagnetic transitions among some of the low-lying states in ^{20}F and ^{55}Fe . We have made comparisons between these values of the reduced matrix elements and those predicted by the extreme single-particle model and the unified model. On the basis of the above comparisons, a value of $J = 3^+$ is suggested for the spin and parity of the 0.66-MeV state in ^{20}F .

Some information concerning the branching ratios of the states at 0.82, 0.98, and 1.31 MeV in ^{20}F and at 2.05 and 2.59 MeV in ^{55}Fe . A previously unreported branching ratio of the 2.96-MeV level was found to be

$$(2.96 \rightarrow 0.0 \text{ MeV}) \quad 0.24 \pm 0.03 ,$$

$$(2.96 \rightarrow 0.66 \text{ MeV}) \quad 0.14 \pm 0.02 ,$$

and

$$(2.96 \rightarrow 0.82 \text{ MeV}) \quad 0.62 \pm 0.06 .$$

CHAPTER I

INTRODUCTION

The study of nuclear energy levels by observing the emission of gamma rays as the levels decay is not new. However, it is only in the last decade that the instrumentations in nuclear spectroscopy have provided reasonably precise and efficient tools for the study of radiative transitions from excited nuclei. The most striking single improvement was the development of the solid state detectors. Using these new and improved instruments, methods have been developed for investigating the properties of nuclear energy levels. In this dissertation the adaptation of these techniques to the measurement of mean lives of nuclear states is described in detail.

In principle the method of calculating the radiative transition probabilities between two nuclear levels is well understood. The transition probability of a given multipolarity is proportional to the matrix element of the appropriate multipole operator taken between the wavefunctions of the final and initial states. However, in practice, the wavefunctions of the initial and final states are very model-dependent. Hence the transition probability is a very sensitive test of the model which was used to generate the wavefunctions.

The inverse of the mean life of a bound level is equal to the sum of all the possible transition probabilities for that level. In the

cases in which we are interested, photon emission is the only important contribution. However, even with transitions by photon emission only, a given level may branch to more than one other level. In turn, each branch may go by a mixture of multipolarities. Thus the relation between the measured mean life of a level and the calculated transition probability for a given multipole transition from that level can become quite involved. This relationship will be presented in detail in Chapter V.

The Doppler-shift attenuation method (DSAM) is the method we use to measure mean lives. The version of that method which we use defines the direction of the motion of the recoiling nuclei by coincidence measurements and is thus widely applicable. In many cases it is the only method which is practical. In this method a reaction of the form $X(a,b)Y$ is produced by a beam of particles, a , which is incident on a target, X . A particle detector is used to detect particles, b , in order to fix the velocity of the recoiling nuclei, Y . A γ -ray detector detects γ rays emitted by Y as it makes a transition to a lower energy level. The energy of these γ rays depends on the speed of the recoiling nuclei and the angle between the direction of recoil and the direction of emission. A shift in energy can be measured by observing the γ -ray emission at two different angles with respect to the recoiling nuclei. As we will show in Chapter II, the mean life of the upper level can be related to this energy shift.

One way to change the angle between the γ -ray detector and the recoiling nuclei is to move the γ -ray detector from one position to another. This movable γ -ray detector method, which has been described in

detail by Wozniak [1], is very simple to use. However, it has an inherent disadvantage. In order to obtain an energy shift, data must be taken with two different γ -ray detector positions and hence at two different times. Since the measured energy shift is often very small, it is extremely sensitive to energy calibration changes that can occur over a period of time in the γ -ray spectrometer system. In order to remove this source of error, a two-target chamber was designed which contained two identical target-particle detector sets. With this arrangement the energies of γ rays emitted at two different angles can be measured simultaneously.

This two-target method has proved to work quite well and has reduced or eliminated several sources of errors which contributed to uncertainties in the measured energy shift. The most important sources of errors which were eliminated were zero shifts and gain changes produced in the electronic equipment. These are usually slowly time varying, and thus their effect can be completely eliminated. Because the γ -ray detector is not moved in this method, changes in background due to different positions of the γ -ray detector were also completely eliminated. Since the process of positioning only has to be done once there is less possibility for error to be made in the positioning of the γ -ray detector. Another advantage to this method stems from the storage of complete data from the beginning of the experiment. This permits the experiment to be terminated at any time with only loss of statistics and not loss of data.

In both the movable γ -ray detector method and the two-target method a solid target backing is used to slow down the recoiling ions. Because of the narrow range of stopping powers in solids, mean lives can only be measured which fall in the range 10^{-14} sec $< \tau < 5 \times 10^{-12}$ sec. Electronic methods can only measure $\tau > 10^{-10}$ sec. Thus in the range 5×10^{-12} sec $< \tau < 10^{-10}$ sec some other method must be used. To help cover this range we have designed a chamber which uses a gas such as krypton as the stopping medium. By changing the pressure of the gas, this method can be used to measure mean lives in the range 5×10^{-12} sec $< \tau < 5 \times 10^{-8}$ sec.

The experimental part of this dissertation consists of using the above methods to make measurements on the nuclei ^{20}F and ^{56}Fe . It was hoped that by measuring the mean lives and branching ratios of some of the low lying levels in ^{20}F we could clarify some of their quantum numbers and provide the incentive to do calculations on this difficult nucleus. The lack of theoretical calculations done on ^{20}F is largely due to the fact that it is an odd-odd nucleus having one proton and three neutrons outside the closed $p_{\frac{1}{2}}$ shell.

The choice of the nucleus ^{20}F was ideal from an experimental standpoint. It can be easily produced by 2-MeV deuterons in the reaction $^{19}\text{F}(d,p)^{20}\text{F}$ and was thus well suited to be done on the 2-MV Van de Graaff which was available at the beginning of this experiment. In addition, ^{19}F is the naturally occurring isotope and exists in many stable compounds so that targets were easily produced.

The choice of ^{56}Fe as a nucleus for investigation was made because of the possibilities of doing theoretical calculations based upon

existing models and because of the total lack of experimental data on mean lives. Work was begun on ^{55}Fe as part of an investigation of the isotonic series $^{49}_{20}\text{Ca}_{29}$, $^{51}_{22}\text{Ti}_{29}$, $^{53}_{24}\text{Cr}_{29}$, and $^{55}_{26}\text{Fe}_{29}$. All members of this series have one neutron outside a closed $f_{7/2}$ shell. The nucleus ^{49}Ca has a closed $d_{3/2}$ proton shell, ^{51}Ti has two protons in the $f_{7/2}$ shell, and ^{55}Fe has two proton holes in the $f_{7/2}$ shell. Hence there are many possibilities for comparisons among members of this series.

Calculations have been done on three members of this series: ^{51}Ti , ^{53}Cr , and ^{55}Fe , using the unified model [2] and the shell model [3,4,5]. However, the correspondence to experimental results has not been good. More recently, Lerner [6] has obtained much better results using a version of the unified model developed and extended by Thankappan and True [7]. Comparisons of the experimental results with the appropriate calculations will be made in Chapter V.

CHAPTER II

THE DOPPLER-SHIFT ATTENUATION METHOD

Complete descriptions of the Doppler-shift attenuation method are now numerous in the literature. Thus only a brief outline of the method will be given here. In the version we use, a nuclear level is populated by a reaction and decays by γ -ray emission. This γ ray is emitted by a nucleus recoiling in some stopping medium. The Doppler-shifted energy of the γ ray is dependent on the instantaneous velocity of the recoiling nucleus at the time of emission of the γ ray. Hence the average Doppler shift is related to the mean life of the nuclear level and to the slowing-down properties of the medium through which the nucleus is recoiling. If these properties can be measured or calculated, the mean life of the nuclear level can be inferred from the mean Doppler shift of the γ rays from that level.

The Doppler-shifted energy of a γ ray, to first order in v/c , is

$$E_{\gamma}(t) = E_0 \left(1 + \frac{\vec{v}(t)}{c} \cdot \hat{r}_{\gamma} \right) \quad (1)$$

E_0 is the energy of the γ ray in the rest frame of the recoiling nucleus. The instantaneous velocity of the recoiling nucleus is $\vec{v}(t)$ where $(v(t)/c) \ll 1$. The unit vector, \hat{r}_{γ} , represents the direction of the emitted γ ray.

The mean energy of many such γ rays is

$$\langle E_{\gamma}(\tau) \rangle_t = \int_0^{\infty} dt E(t) W(t, \tau). \quad (2)$$

The weighting function, $W(t, \tau)$, is the number of excited nuclei which decay per unit time. This weighting function is given by

$$W(t, \tau) = \frac{1}{N_0} \frac{dN(t, \tau)}{dt} = \frac{1}{\tau} e^{-t/\tau}, \quad (3)$$

where τ is the mean life of the nuclear level. The difference in the mean Doppler-shifted energy of the γ ray from E_0 is thus

$$\Delta \langle E_{\gamma}(\tau) \rangle_t = \langle E_{\gamma}(\tau) \rangle_t - E_0 = \frac{E_0}{c} \int_0^{\infty} \frac{dt}{\tau} e^{-t/\tau} \vec{v}(t) \cdot \hat{r}_{\gamma} \quad (4)$$

This equation shows explicitly the relationship of the shift in the mean energy of the γ ray to the mean life of the nuclear level which produced it.

It is convenient to remove the energy dependence from Eq. (4) by taking the ratio of the measured energy shift to the maximum energy shift. This ratio, called the Doppler-shift attenuation factor, is defined by

$$F(\tau) \equiv \frac{\frac{E_0}{c} \int_0^{\infty} \frac{dt}{\tau} e^{-t/\tau} \vec{v}(t) \cdot \hat{r}_{\gamma}}{\frac{E_0}{c} \vec{v}(0) \cdot \hat{r}_{\gamma}}, \quad (5)$$

which can be reduced to

$$F(\tau) = \int_0^{\infty} \frac{dt}{\tau} e^{-t/\tau} \frac{v(t)}{v_0}, \quad (6)$$

where $v_0 \equiv v(t=0)$. Eq. (6) is strictly true only when all the recoiling nuclei have the same \vec{v}_0 . However, Wozniak [1] has shown that even if there is a spread in the initial velocities of the recoiling nuclei, \vec{v}_0 may be replaced by an average of \vec{v}_0 , with negligible error in the final results.

The remaining problem, that of finding a suitable function for $v(t)$, is not an easy or straightforward one. To greatly simplify the problem of finding a functional form for $v(t)$, we ignore nuclear collisions as a first approximation. We further assume, in the velocity region in which we are interested, that the electronic slowing down is velocity dependent [8]. This electronic stopping power is given by

$$-\left(\frac{dE}{dx}\right)_e = -M \frac{dv}{dt} = M \frac{v}{\alpha}, \quad (7)$$

where M is the mass of the recoiling nucleus and α is the characteristic electronic slowing-down time of the stopping material. Upon integration Eq. (7) becomes

$$v(t) = v_0 e^{-t/\alpha}. \quad (8)$$

Substitution of Eq. (8) into Eq. (6) gives

$$F(\tau) = \int_0^{\infty} \frac{dt}{\tau} e^{-t(\frac{1}{\tau} + \frac{1}{\alpha})} = \frac{\alpha}{\alpha + \tau} \quad (9)$$

Eq. (9) is useful not only because it is simple, but also because it is a fairly good approximation even though it ignores the effects of nuclear collisions. A very useful rule of thumb is provided by Eq. (9). To make $F(\tau)$ most sensitive to τ , the stopping power constant, α , must be made approximately equal to τ .

At the low recoil velocities encountered in our Doppler-shift measurements, nuclear as well as electronic collisions must be considered. Nuclear collisions affect the Doppler shift in two ways. In each nuclear collision the recoiling nucleus loses part of its kinetic energy. In addition, its direction of motion can be drastically altered. Blaugrund [9] has shown that these effects can be taken into account by replacing $v(t)$ in Eq. (5) with $\overline{v(t) \cos \varphi(t)}$. The $\overline{(\quad)}$ indicates an average of the quantity (\quad) over nuclear scattering. With little error [9], $\overline{v(t) \cos \varphi(t)}$ can be replaced by $v(t) \overline{\cos \varphi(t)}$. Here $v(t)$ includes both nuclear and electronic slowing down, and $\overline{\cos \varphi(t)}$ represents the deviation of the recoiling nucleus from its initial direction as a function of time. Both of these functions, as well as a generalization of the method to include more than one type of atom in the stopping material, have been given by Blaugrund [9]. In his calculations he used the nuclear and electronic stopping power equations of Lindhard, Scharff, and Schiott [8]. Wozniak [1] has extended the lower energy limit as presented by Blaugrund [9] by about a factor of ten. With these

modifications Eq. (6) becomes.

$$F(\tau)_{\text{calc}} = \int_0^{\infty} \frac{dt}{\tau} e^{-t/\tau} \frac{v(t)}{v_0} \overline{\cos \varphi(t)}, \quad (10)$$

where it is assumed that $\hat{v}(t) = \dot{\hat{v}}_0$.

Some evidence has been presented which indicates that the results of stopping powers as calculated by Lindhard et al. [8] may disagree with experimental measurements by as much as 20% [10]. Because the evidence is not conclusive we have adopted the approach of quoting two errors. The first includes all experimental errors. The second, in addition to all experimental errors, includes an error due to a $\pm 20\%$ uncertainty assigned to the stopping powers.

The experimental procedure requires that a modification of Eq. (10) be made to allow for finite target thickness. Because the recoiling nuclei are produced throughout the thickness of the target, they have progressively less target material to traverse before reaching the backing material. Thus variation in stopping mediums can be taken care of by dividing the target into N strips each of thickness ΔT , calculating $F_i(\tau)$ for the i^{th} strip using Eq. (10), and averaging over the N strips. Each $F_i(\tau)$ is calculated for a nucleus recoiling through a target thickness, $T = (i - \frac{1}{2}) \Delta T$, and into an infinitely thick backing. In this process the functions $v(t)$ and $\overline{\cos \varphi(t)}$ are required to be continuous at the target-backing interface. The $F(\tau)$ to be compared with experimental measurements is the average,

$$F(\tau)_{\text{calc}} = \frac{1}{N} \sum_{i=1}^N F_i(\tau) . \quad (11)$$

In practice, the mean life, τ , is determined in the following way. Using Eq. (11), $F(\tau)_{\text{calc}}$ is calculated for several values of τ and a plot of F vs. τ is made as shown in Fig. 1. The value of $F(\tau)_{\text{expt}}$ is read into these calculated curves and the corresponding mean life, τ_{expt} , is read out. A detailed discussion of the determination of $F(\tau)_{\text{expt}}$ will be given in Chapter III.

The integral in Eq. (10) is integrated numerically by the method of Gaussian quadratures. Since the weighting function, $e^{-t/\tau}$, is very small for $t \geq 10 \tau$, the limits of integration are unrealistic when doing a numerical integration. To improve the form of this integral for numerical integration we can rewrite Eq. (10) as

$$F(\tau) = \int_0^{\infty} \frac{dt}{\tau} e^{-t/\tau} f\left(\frac{t}{\tau}\right) , \quad (12)$$

where $f\left(\frac{t}{\tau}\right) = (v(t)/v_0) \overline{\cos \varphi(t)}$. Eq. (12) suggests a change of variables of the form $y = e^{-t/\tau}$. Making this change of variables in Eq. (12) gives

$$F(\tau) = - \int_1^0 dy f(-\ln y) . \quad (13)$$

This form of the integral is now quite amenable to a numerical integration. In practice the change of variables permits a drastic reduction of the number of integration points used and thus results in a significant savings in computer time.

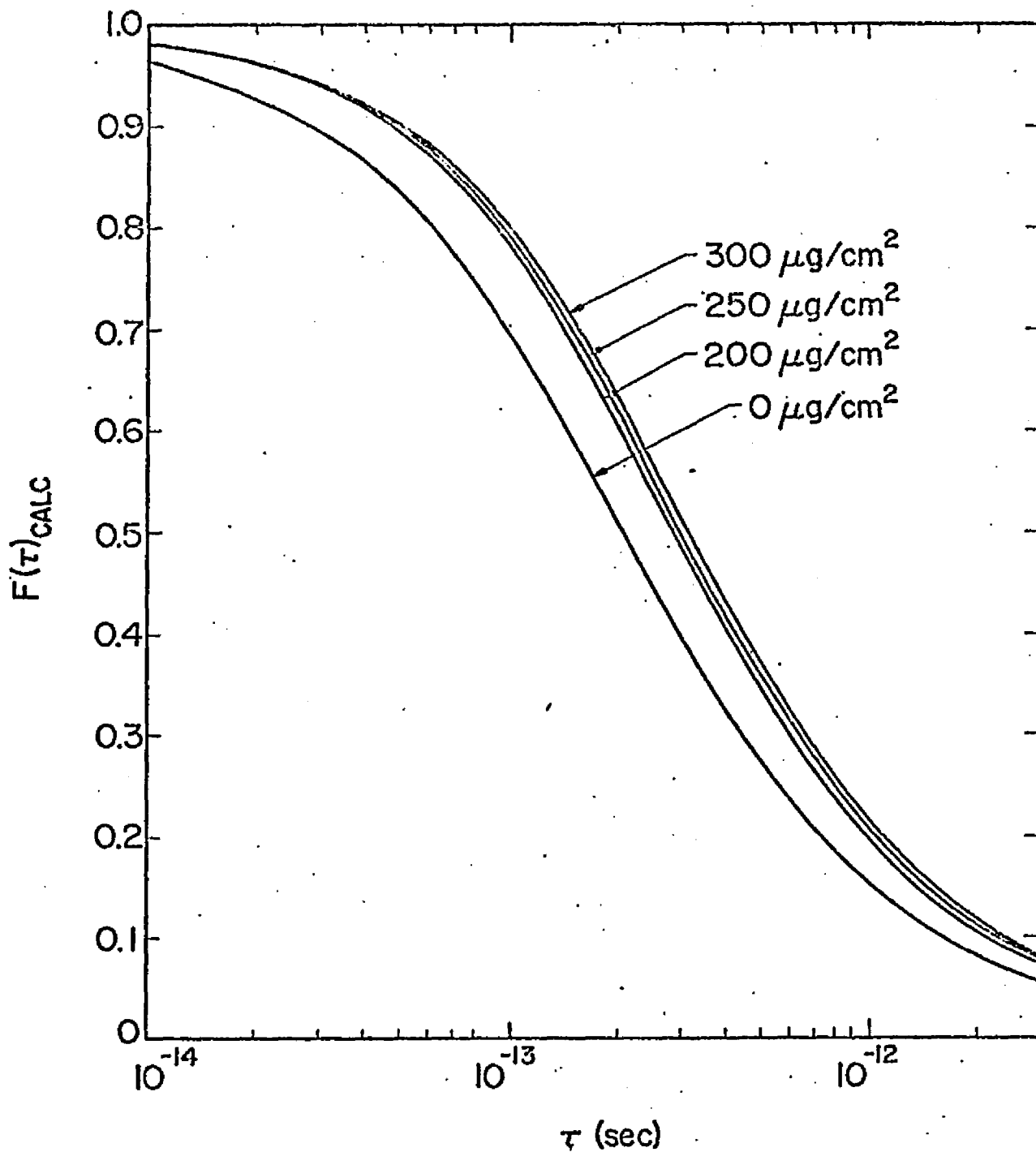


Fig. 1. F_{calc} vs. τ for a solid target with a solid backing.

$F_{\text{calc}}(\tau, |\vec{v}_0|)$ is plotted vs. τ for four thicknesses of natural calcium fluoride on a thick copper backing. $|\vec{v}_0|/c = 0.00831$ for the recoiling ^{20}F nuclei.

CHAPTER III

EXPERIMENTAL DETAILS

The coincidence version of the Doppler-shift attenuation method as we use it, must have a reaction of the form $X(a,b)Y$. A beam of particles, a , having a well-defined energy which, together with a counter that detects the reaction particles, b , serves to fix the direction and energy of the recoiling nuclei, Y . As these nuclei slow down in some material they decay by γ -ray emission. A γ -ray detector is used to fix the energy and direction of these emissions.

The mean energy of these γ rays is dependent on the energy of the nuclear level, on the angle between the direction of the recoiling nuclei and the direction of the γ -ray detector, and on the mean velocity of the recoiling nuclei. The mean velocity is in turn dependent on the stopping power of the material through which the nuclei recoil and on the mean life of the nuclear level. Therefore, to produce an experimental shift in the mean energy of γ rays from a level with a given mean life, either the stopping power of the material through which the nuclei recoil, or the position of the γ -ray detector must be changed.

Solid Backing

In the greater part of our work we keep the recoil material constant and change the position of the γ -ray detector. When this is done, the experimental attenuation factor is given by

$$F_{\text{expt}} \equiv \frac{\Delta \langle E_{\gamma} \rangle_{\text{meas}}}{\Delta \langle E_{\gamma} \rangle_0} = \frac{[\langle E_{\gamma 1} \rangle - \langle E_{\gamma 2} \rangle]_{\text{meas}}}{\frac{E_0}{c} \langle \vec{v}_0 \rangle_p \cdot [\langle \hat{r} \rangle_{\gamma 1} - \langle \hat{r} \rangle_{\gamma 2}]}, \quad (14)$$

where the subscripts, 1 and 2, refer to the two positions of the γ -ray detector. The numerator, $\Delta \langle E_{\gamma} \rangle_{\text{meas}}$, is the experimental value of the attenuated Doppler shift. This shift is found by taking the difference of the mean γ -ray energies, $\langle E_{\gamma i} \rangle_{\text{meas}}$, measured at two detector positions. Each of these mean energies is the result of three averages folded together. The first of these is the inherent spread in energy due to Doppler shifting of the γ -ray energy. This spread approaches zero only for $\tau \gg \alpha$ where $\langle E_{\gamma} \rangle = E_0$ or $\tau \ll \alpha$ where $\langle E_{\gamma} \rangle = E_0 \pm \frac{1}{2} \Delta \langle E_{\gamma} \rangle_0$. Folded in with this average is the space average due to finite geometry and the statistical average due to the finite resolution of the γ -ray detector. The average due to finite geometry is accounted for in the denominator of Eq. (14). The denominator, $\Delta \langle E_{\gamma} \rangle_0$, is the calculated full, or unattenuated, Doppler shift. This is the shift that would be measured if the nuclei recoiled into a vacuum with an average velocity $\langle \vec{v}_0 \rangle_p$. The vector $\langle \vec{v}_0 \rangle_p$ is the space average of \vec{v}_0 , the initial velocity of the recoiling nuclei. A spread in \vec{v}_0 is caused by the finite size of the particle detector. The direction of the emitted γ ray is represented by the unit vector \hat{r} . Its average, over the finite γ -ray detector at the i^{th} position, is $\langle \hat{r} \rangle_{\gamma i}$. This vector must be evaluated for each detector at each position. Wozniak [1] has given the method for use when $\langle \hat{r} \rangle_{\gamma i}$ is perpendicular to the face of the γ -ray

detector. Appendix A gives a method for use in a more general case when the detector face is not perpendicular to $\langle \hat{r} \rangle_{\gamma i}$. Wozniak [1] has discussed in detail the calculation of $\Delta \langle E_{\gamma} \rangle_o$, the denominator in Eq. (14). He has shown that under typical experimental conditions $\langle \vec{v}_o \rangle_p \cdot \langle \hat{r} \rangle_{\gamma} \approx 0.95 (\vec{v}_o \cdot \hat{r})_{\text{point detectors}}$. That is, the finite size of the detectors causes approximately a 5% reduction in the unattenuated Doppler shift from that calculated using point detectors.

The Two-Target Chamber

Fig. 2 shows the two-target Doppler-shift chamber. This chamber employs two target-particle-detector sets to produce the two γ -ray detector positions in Eq. (14). Since the ratio in Eq. (14) involves differences, it is desirable to make these differences as large as possible. This can be done by making $\langle \vec{v}_o \rangle_p$ and $|\langle \vec{v}_o \rangle_p \cdot \langle \hat{r} \rangle_{\gamma i}|$ as large as possible. The average initial velocity, $\langle \vec{v}_o \rangle_p$, was maximized by positioning the center of the annular particle detector at 180° with respect to the beam direction. With this arrangement, $\langle \vec{v}_o \rangle_p$ was in the direction of the beam. Once $\langle \vec{v}_o \rangle_p$ had been fixed the dot product was maximized by positioning the γ -ray detector as close to 0° and 180° with respect to the beam as possible.

The γ -ray detectors used were of the solid state p-i-n type. They were made from an ingot of p-type germanium drifted from five sides with lithium. The crystal was cooled to liquid nitrogen temperatures to maintain the p-i-n structure. A reverse bias of from -1500 to -2000 V was applied across the crystal to sweep out the electrons and holes produced by energy losses of the γ rays to electrons in the crystal.

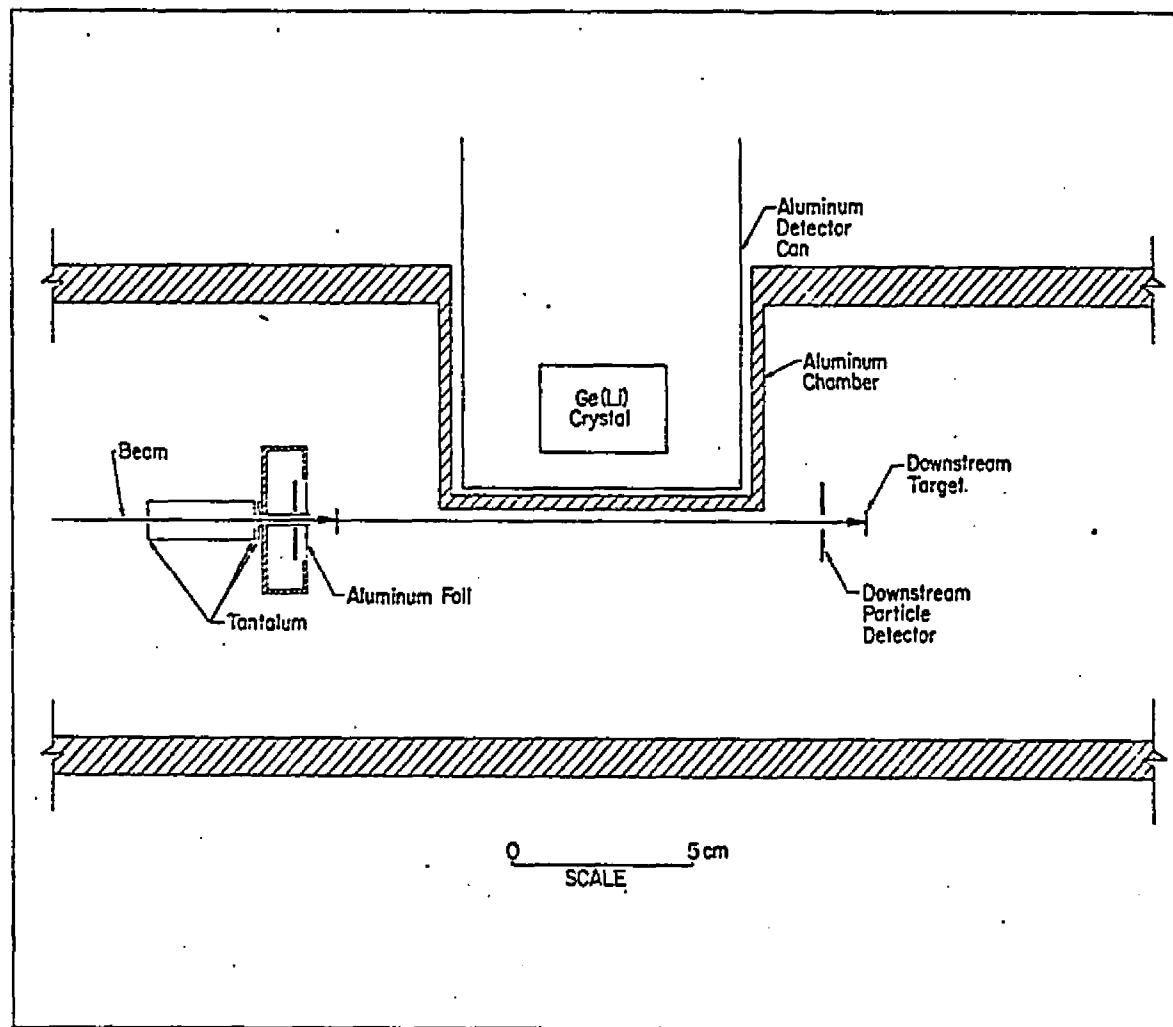


Fig. 2. Experimental arrangement of the two-target chamber.

The collimator arrangement for the downstream detector is identical to that shown for the upstream detector. The aluminum foil was 0.001 in. thick for 2-MeV deuterons and 0.003 in. thick for 3.5-MeV deuterons.

Crystals were used which had volumes of 20 to 40 cm³, and a ratio of photo peak to total efficiency of approximately 3% at 1.33 MeV. The relative efficiency as a function of γ -ray energy was measured up to approximately 3 MeV for each detector. A typical curve is shown in Fig. 3. The procedure for obtaining such a curve is as follows. Several γ -ray sources, each of which produced at least two γ rays of known relative intensities, were selected to cover the energy range up to approximately 3.0 MeV. Energy spectra were taken using the same geometrical setup as in the target chamber with the source replacing the target. The relative area under each peak vs. the energy of that peak was then fitted to a smooth curve corresponding to Fig. 3. The sources with their γ rays and respective relative intensities are listed in Table I.

The detector resolution is related to the energy needed to create a hole-electron pair in the detector crystal and is the limiting factor on the system resolution. The capacitance of the detector and cable at the preamplifier input determines the noise in the preamplifier. These two effects together with other noise sources determine the system resolution. Under typical conditions in coincidence experiments the system resolution varied from approximately 4 keV to greater than 10 keV full width at half maximum (FWHM). The broadening of resolution could be caused by pulse pileup due to high count rates. However, after a period of time, all detectors exhibited irreparable broadening of resolution due to neutron damage in the germanium crystal.

Timing information from lithium-drifted germanium, Ge(Li), γ -ray detectors is dependent in a large part on their charge collection time.

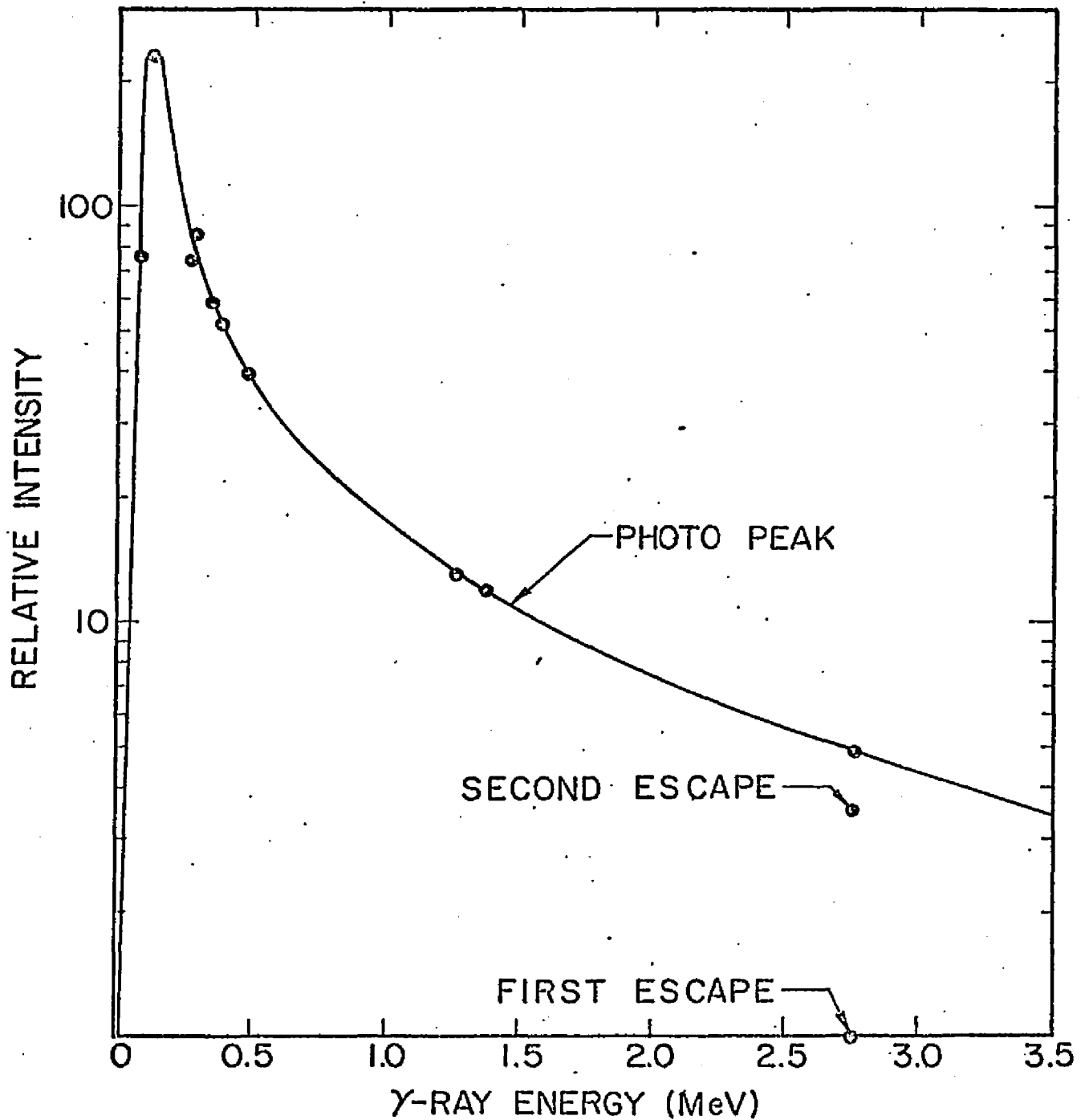


Fig. 3. Photo-peak relative efficiency vs. γ -ray energy.

One point on the first-escape and one point on the second-escape curves are also plotted.

Table I. Gamma-ray energies and relative intensities used in calculating relative photo peak efficiency curves.

Source	Energy (keV) ^a	Relative Intensity
¹³³ Ba ^b	30.89 ± 0.18	129.0 ± 9.0
	35.29 ± 0.18	33.9 ± 2.3
	53.18 ± 0.04	3.78 ± 0.09
	79.60 ± 0.05	64.7 ± 4.2
	80.997 ± 0.006	
	160.66 ± 0.06	1.21 ± 0.05
	223.37 ± 0.23	0.803 ± 0.042
	276.46 ± 0.20	11.61 ± 0.17
	303.08 ± 0.20	29.75 ± 0.29
	356.27 ± 0.14	100
384.10 ± 0.18	14.18 ± 0.26	
²² Na ^c	511.006 ± 0.002	100
	1274.55 ± 0.04	55.25 = 100/(2 x 0.905)
⁶⁰ Co ^d	1173.23 ± 0.04	100
	1332.49 ± 0.04	100
²⁴ Na ^c	1368.526 ± 0.044	100
	2753.92 ± 0.12	100

^aJerry B. Marion, University of Maryland Department of Physics and Astronomy, Technical Report 656 (unpublished) [11].

^bRelative intensities (from Ref. a).

^cRelative intensities from P. M. Endt and C. van der Leun, Nucl. Phys. A105, 1 (1967) [12].

^dRelative intensities from Nuclear Data Sheets, Sheet NRC 60-5-24, Printing and Publishing Office of the National Academy of Sciences, National Research Council [13].

Their collection time is in turn determined in part by the applied voltage and the geometry of the drifted region in the crystal. In practice the best timing resolution which we could obtain was on the order of 30 nsec FWHM.

The particle detectors used were of the silicon surface barrier type. They were typically 300 mm^2 annular detectors depleted to a depth of 1000μ . This depth was sufficient to stop 10 MeV protons. The detectors required typically +300 V bias, required no cooling, and had a very short charge-collection time. This short collection time meant that the timing resolution was almost entirely due to the charge-collection time in the γ -ray detector. The resolution of the particle detector was much better than that realized under experimental conditions. A broadening by a factor of five of the particle peaks was caused by kinematic broadening and by straggling of the particles in the protective covering over the face of the detector. Resolutions obtained under experimental conditions were at best on the order of 100 keV FWHM.

The collimation of the beam and the shielding of the particle detector are shown in Fig. 2. The beam was collimated to less than 0.1 inches in diameter by the series of apertures through which the beam passed. The final aperture in each case was a length of tubing which passed through the annular detector and made contact with the aluminum covering over the face of the detector. The tubing collimator and aluminum covering served to keep both light and elastically-scattered beam particles from the detector itself. The two apertures which preceded the tube collimator were slightly smaller than the inside diameter of

the tube. They were grounded so that any charge collected by collimating the beam would not be grounded through the shielding of the signal cable to the particle detector. The collimation by one particle detector configuration limited the maximum uncertainty in beam direction to approximately $\pm 2.5^\circ$. However, when two such collimations were used in the chamber shown in Fig. 2, the maximum uncertainty in beam direction was reduced to approximately $\pm 0.65^\circ$.

A block diagram of the electronics arrangement is shown in Fig. 4. Because of symmetry only one particle detector together with its electronics is shown.

In the linear γ -ray leg, a low noise charge-sensitive Tennelec 135 preamplifier converted the charge from the detector to a low impedance voltage output. A Tennelec 203 linear amplifier with a 0.5 to 1 μ sec integration time-constant shaped and amplified the pulses from the preamp to prepare them for the analog-to-digital converter (ADC). The amplifier also contained a pole zero cancellation and a base line restoration circuit to reduce pileup effects at high counting rates. The unipolar output was automatically delayed 2.5 μ sec to permit the logic signals to be formed and to arrive at the linear gate before the linear pulse. A Northern Scientific 401 digital stabilizer, which employed an internal and external precision pulser, was used to provide both zero and gain stabilization in the electronics of the linear γ -ray leg. The pulse-height analyzer consisted of a Nuclear Data 161F 4096-channel ADC and a Nuclear Data 180M 1024-channel memory unit.

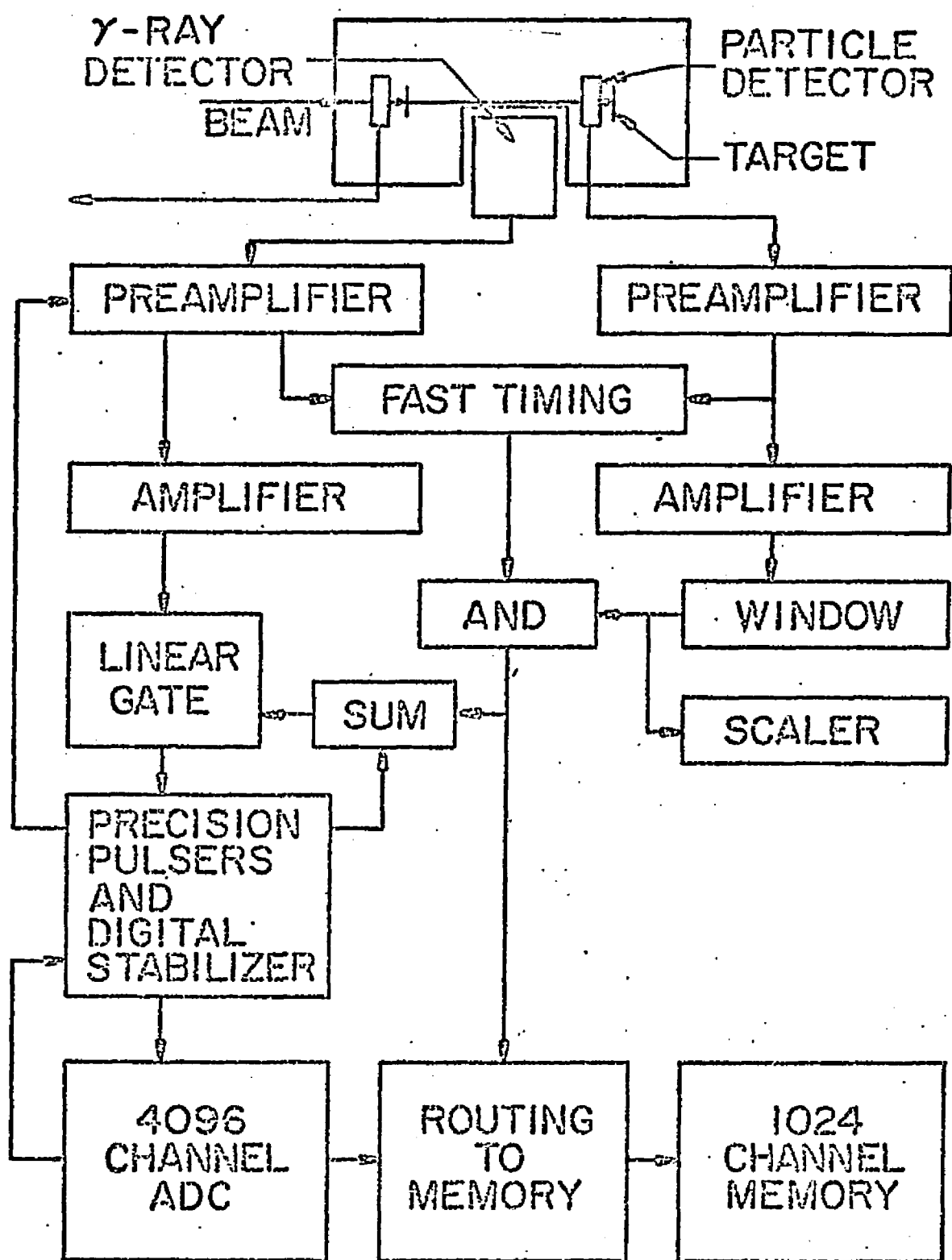


Fig. 4. Block diagram of electronics used with two-target chamber.

Only the electronics associated with one particle detector are shown.

An Ortec 109 preamplifier and an Ortec 410 linear amplifier in the linear particle leg served essentially the same functions as the respective components in the linear γ -ray leg. However, the Ortec amplifier did not have pole zero cancellation or base line restoration. The energy of the particle was analyzed by an Ortec 420 timing single channel analyzer (TSCA) which set a window over a portion of the particle energy spectrum. The resulting logic signal was used to gate and route the pulses in the linear γ -ray leg.

The coincidence setup presented in Fig. 4 is of the fast-slow type. The use of low-level leading-edge timing on both the γ -ray and particle pulses produced logic pulses with the smallest deviation in time caused by variations in amplitude and rise time. These pulses were put into fast coincidence using a time-to-amplitude converter (TAC). A strobed single channel analyzer with a window width of typically 60 to 100 nsec, was used to determine the coincidence interval and to convert the TAC output to a logic signal. This fast coincidence signal was then put into slow coincidence with each of the outputs of the windows over the particle energy spectra. The two-target chamber required one or more of these windows for each particle detector. For each window there had to be a corresponding logical AND box. The outputs of the AND boxes were summed to open the linear gate and were sent separately to the memory routing box.

Before the recent developments in low-level leading-edge timing, we employed cross-over-pick-off (CPO) timing and a coincidence method of the slow-fast type. In this method a fast timing logic signal was

produced by setting the window of a TSCA over a portion of the particle spectrum. This logic signal was then put into fast coincidence with a γ -ray timing signal. The fast-slow and slow-fast methods are, in principle, not the same. A relative comparison depends on ratios of signal to background and particle to γ -ray counting rates. This comparison is made in Appendix B using typical experimentally-determined values of the above ratios.

With the addition of the two-target chamber it was mandatory to have a routing box to sort out the γ rays which belonged to each target. In addition, the use of more than one window in each particle spectrum required a routing box to sort out the γ rays from a given target which corresponded to a given particle peak. Such a routing-to-memory box was designed and built by M. J. Wozniak, Jr. and the author. Complete details of the logic and electronic schematics are given in Appendix C.

Target Preparation

Targets were prepared by the author using various evaporation techniques on a variety of target materials and backings. The choice of target material for naturally occurring isotopes was made considering ease of evaporation, stability of the target material compound at high evaporation temperatures, and lack of isotopes in the target material with atomic numbers comparable to or lower than the target isotope. The target backing was chosen because of the stopping power of the material and the necessity of having a material with a high atomic number. Backing materials most commonly used were copper and tantalum. The copper backings were cleaned in a dilute solution of nitric acid. Tantalum

backings were cleaned in a commercial chromic acid solution prepared for cleaning laboratory glassware.

All target evaporations were done inside a bell jar pumped down to approximately 10^{-6} Torr. The more abundant target materials were evaporated from a tantalum boat using resistive heating in the tantalum. Rare isotopes required the use of a Materials Research Corporation model V4-200 electron gun. A cross-section of the electron gun configuration found to be most generally satisfactory is shown in Fig. 5. This configuration permitted the tantalum dish to become extremely hot with the carbon crucible heating only by conduction from the tantalum dish. Thus materials, which could not be done on the copper pedestal because of their high heat conduction and high melting point, could be evaporated easily with very little carbon contamination. When a rare target material reacted with the tantalum during evaporation, the material loss was held to a minimum by placing a tantalum ring, approximately 1/4 inches in diameter x 3/32 inches in height, in the center of the tantalum dish and placing the target material inside this ring. Cleaning of the tantalum dish and ring was accomplished by heating them up to working temperature under vacuum with no target material in the dish. Table II lists the various target materials and evaporation parameters used by the author.

The target thickness in $\mu\text{g}/\text{cm}^2$ was determined by evaporating the target onto a backing of known mass and dividing the difference in the mass of the backing after evaporation by the area of the target. This method of determining the thickness of a target from its mass and area

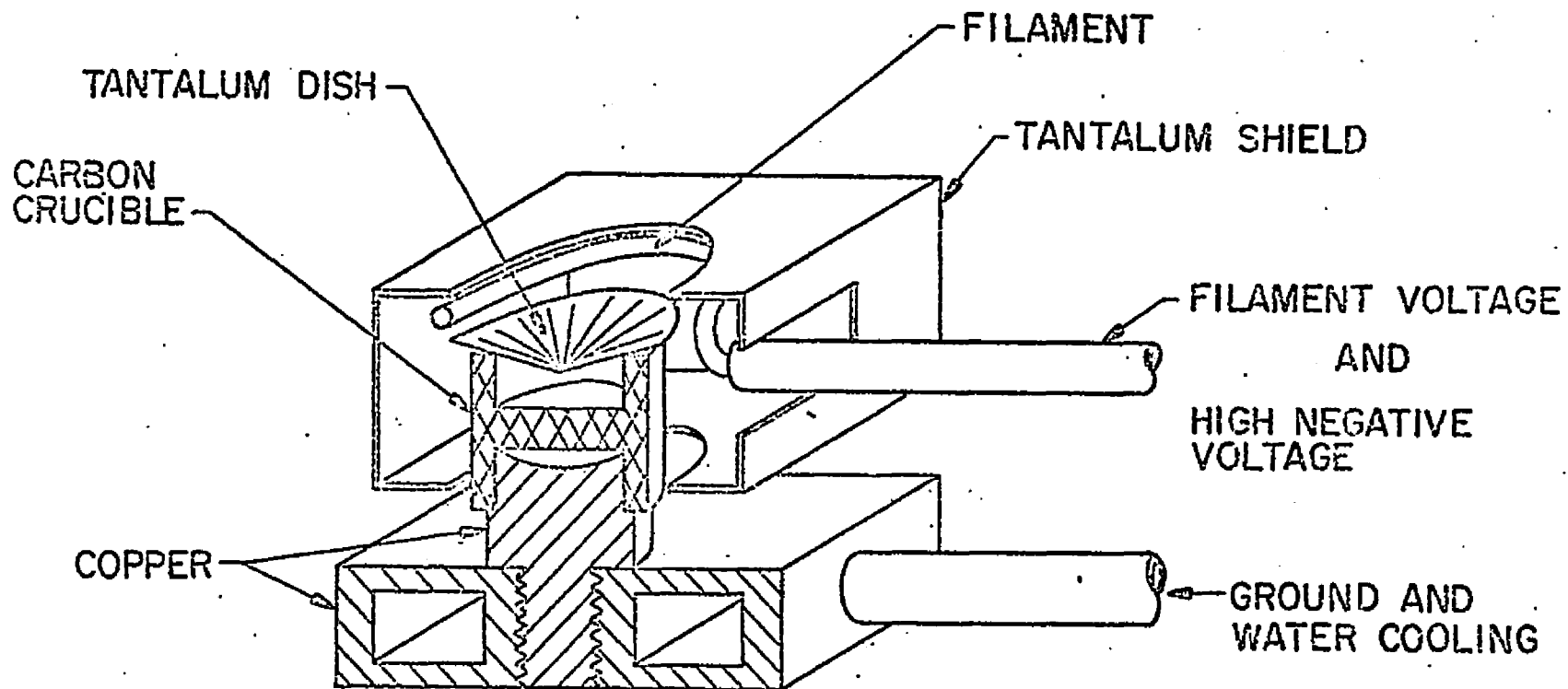


Fig. 5. Electron gun configuration.

The electron gun configuration, used to evaporate high melting point, high heat conduction materials, is shown in detail.

Table II. Target materials and evaporation parameters.

Tar- get	Target Material	Form	Method	Filament		Beam		Time (sec)	Height of Back- ing (cm)	Weight of Target Ma- terial (mg)	Target Thick- ness ($\mu\text{g}/\text{cm}^2$)
				Volt- age (volts)	Cur- rent (amps)	Volt- age (volts)	Cur- rent (amps)				
¹¹ B	98.6% en- riched Boron-11	Amor- phous	Boat ^a	10	150 pulsed to 500			25	2.5	Large	100
¹⁹ F	Natural Calcium- Fluoride	Powder	Boat ^a	10	200			10	15	Large	100
					200			25			450
					250			25			1000
²⁰ Mg	Natural Magnesium	Metal Turnings	Boat ^a	10	100			10	15	Large	30
					110			15			60
¹⁸ O	Natural Silicon- dioxide	Fused Quartz	Gun ^b		0.56	2000	0.15	20	10	Large	130
								10			20
⁵⁴ Fe	98.2% enriched Iron-54	Metal reduced from iron oxide	Gun ^b		0.60	1000	0.35	Com- plete Evap- ora- tion	2.5	8 20	135 375

^aBoats were made from approximately 1 x 2.25 x 0.005 inch tantalum. (Thickness and area affect the temperature for a given current).

^bGun configuration shown in Fig. 5.

assumes a uniform thickness. It is therefore accurate only when the distance from the source of evaporation is larger than the diameter of the target. Accuracies as good as $\pm 5 \mu\text{g}/\text{cm}^2$ were achieved using a target backing with an area of 10 cm^2 and a Mettler precision balance which was capable of weighing to better than 50 μgrams .

Data Taking and Reduction

A beam of accelerated particles was provided by the 2 MV and 6 MV Van de Graaff accelerators of the University of Arizona's Van de Graaff laboratory. The beam was energy-analyzed by passing it through a 90° bending magnet. The magnetic field was monitored with a gaussmeter which was calibrated to energy units by using the 1.881-MeV threshold of the ${}^7\text{Li}(p,n){}^7\text{Be}$ reaction.

The particle counting rates were monitored by scaling the counts through a window in the particle spectrum. For the two-target chamber this had to be done for both particle detectors using identical windows. Since the γ -ray counting rate was proportional to the particle counting rate at a given angle, equalizing the particle counting rates from the two detectors served to equalize the γ -ray counting rates from the two targets. The counting rates were adjusted by changing the ratio of the beam on the two targets. This was accomplished by first stopping the beam with the downstream target and then moving the upstream target into the beam until the desired counting rate was achieved. The intensity of the beam was then adjusted until the γ -ray counting rate reached a maximum permissible value.

Data accumulation was made in sets of not less than three runs. After each run the data which were stored in the pulse-height analyzer were printed, plotted, and punched onto paper tape. The paper tape was later converted to punched cards which were fed into a CDC 6400 computer for data reduction. After completion of the readout, the memory of the pulse-height analyzer was erased and a new set of data was accumulated. This procedure permitted us to do an experimental statistical-error analysis of the results of the runs to compare with a calculated statistical error.

In practice the background in the region of a peak was fitted to a quadratic function by the method of least squares. After the background was subtracted out the centroid of the remainder, within a small interval around the peak, was found. The centroid obtained in this way is proportional to $\langle E_Y \rangle_{\text{meas}}$.

Analysis of Errors

Wozniak [1] has given a complete description of the calculated error of the centroid difference, $\delta(\Delta \langle E_Y \rangle_{\text{meas}})$. The results of these calculations were compared with an experimental statistical deviation by computing the mean $\Delta \langle E_Y \rangle_{\text{meas}}$ from three or more runs and then finding the standard deviation of the mean $\Delta \langle E_Y \rangle_{\text{meas}}$. The calculated statistical error was computed using the sum of all runs. In general the two errors in $\Delta \langle E_Y \rangle_{\text{meas}}$ were approximately equal. In all cases the larger error was used.

The error in the denominator of Eq. (14), $\delta(\Delta \langle E_Y \rangle_0)$, has six possible sources: (1) the beam energy; (2) the position and subtended

solid angle of the particle detector; (3) the position and subtended solid angle of the γ -ray detector; (4) the angular distribution of the particles; (5) the Q-value of reaction $X(a,b)Y$; and (6) the masses of X, a, b, and Y. Errors due to the last two parameters are negligible compared to the others, and will therefore not be considered further. The error due to each parameter was obtained by finding the maximum possible deviation in each parameter and then calculating the corresponding deviation in $\Delta\langle E_Y \rangle_0$. This deviation was assumed to be approximately two standard deviations. The standard deviation of $\Delta\langle E_Y \rangle_0$ was taken to be the square root of the sum of the squares of the standard deviations produced by deviations in the first four parameters. Table III gives typically adopted deviations in these four parameters and the resultant deviation in $\Delta\langle E_Y \rangle_0$. In practice $\delta(\Delta\langle E_Y \rangle_0) \approx 2\% \Delta\langle E_Y \rangle_0$. Half of the error is due to the possibility of an angular distribution. This 1% represents a change by a factor of five in the particle counting rate across the face of the detector.

Finally, the relative error in F_{expt} is given by

$$\frac{\delta(F_{\text{expt}})}{F_{\text{expt}}} = \left\{ \left[\frac{\delta(\Delta\langle E_Y \rangle_{\text{meas}})}{\Delta\langle E_Y \rangle_{\text{meas}}} \right]^2 + \left[\frac{\delta(\Delta\langle E_Y \rangle_0)}{\Delta\langle E_Y \rangle_0} \right]^2 \right\}^{\frac{1}{2}} \quad (15)$$

When finding the centroids to calculate $\Delta\langle E_Y \rangle_{\text{meas}}$, the interval around the peak was varied in width to see what effect this would have on the shift of the centroid. The width was varied from approximately the full width at one-tenth maximum on the peak, to a width which included all that could reasonably be ascribed to the peak. When this change in

Table III. Calculated deviations in the average initial recoil energy, $\langle E_Y \rangle_0$, and average relative full shift, $\Delta \langle E_Y \rangle_0 / E_0$, due to deviations in the parameters of the full shift calculation.^a

Parameter	Maximum Deviation	$\langle E_Y \rangle_0$ (MeV)	Full Shift $\frac{\Delta \langle E_Y \rangle_0}{E_0}$	Percent Deviation in Full Shift
Normal Calculation with no deviations.	None	0.861	0.01659	0.0
Beam energy = 2.25 MeV.	± 50 keV	0.873 0.848	0.01672 0.01646	± 0.8
Inner radius of annular particle detector = 2 mm.	+ 1 mm	0.857	0.01651	- 0.4
Distance of one particle detector to target = 11.43 mm.	± 0.5 mm	0.857 0.864	0.01655 0.01662	- 0.2 + 0.25
Angle between beam and γ -ray detector = 24°	$\pm 1^\circ$	0.861	0.01645 0.01672	- 0.8 + 0.8
Angular distribution function (Outside of particle detector weighted).	0.2 to 1.2 (factor of 6)	0.851	0.01640	- 1.1
Angular distribution function (Inside of particle detector weighted).	1.2 to 0.2 (factor of 6)	0.873	0.01684	+ 1.5

^aThe calculations were done for the fourth excited state in ^{20}F produced by the $^{19}\text{F}(d,p)^{20}\text{F}^*$ reaction which has a Q_4 -value of (4.374 - 1.309) MeV.

width had a significant effect on the shift of the centroid, a corresponding error was included in $\delta(\Delta\langle E_Y \rangle_{\text{meas}})$.

The Error, $\delta(\tau_F)$, Due to $\delta(F_{\text{expt}})$. We will treat the error, $\delta(F_{\text{expt}})$, as a wholly statistical error even though, as was seen previously, there are components of $\delta(F_{\text{expt}})$ which are systematic in nature. The resulting error $\delta(\tau_F)$ can be found directly from the curves in Fig. 1 by reading the values of τ corresponding to $F_{\text{expt}} \pm \delta(F_{\text{expt}})$ from the correct target thickness curve.

The Error, $\delta(\tau_T)$, Due to Uncertainties in Target Thickness, $\delta(T)$. The uncertainties in target thickness have been discussed in the section on target preparation. The curves in Fig. 1 show the effect of $\pm 50 \mu\text{g}/\text{cm}^2$ on a $250 \mu\text{g}/\text{cm}^2$ thick target of ^{19}F . The error $\delta(\tau_T)$ is the difference in τ for a given F_{expt} as read from the different target thickness curves in Fig. 1. This $\delta(\tau_T)$ will also be treated as being wholly statistical.

The Error, $\delta(\tau_{\text{sp}})$, Due to Uncertainties in Stopping Power.

Blaugrund et al. [10] have suggested that the nuclear and electronic stopping powers be multiplied by the constants f_n and f_e respectively. This was done to permit a better fit between calculations and experimental data. It was suggested that these constants might vary by as much as 20% from unity. The evidence is not conclusive so that we have taken $f_e = f_n = 1$ to give the correct stopping power. A variation in F_{calc} results by letting f_e and f_n vary by 20%. These curves are shown in Fig. 6. As is generally the case,

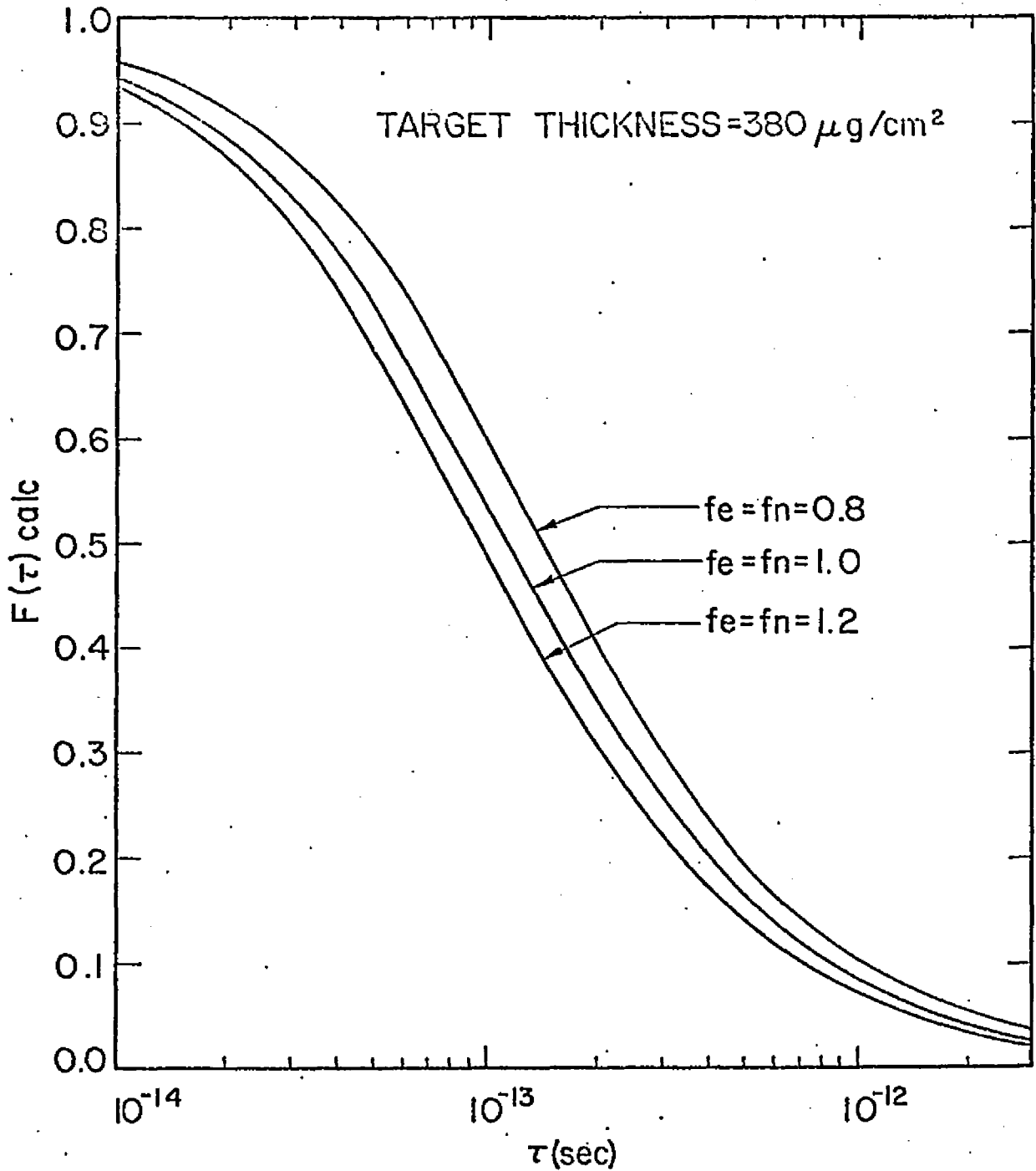


Fig. 6. Effects of stopping power uncertainties on F_{calc} for a solid target with a solid backing.

Effect of a 20% uncertainty in stopping power on $F(\tau, |\vec{v}_0|)$ is plotted vs. τ for a $375 \mu\text{g}/\text{cm}^2$ target of ^{54}Fe on a thick tantalum backing. $|\vec{v}_0|/c = 0.00453$ for the recoiling ^{56}Fe nuclei.

$f_e = f_n = 0.8$ and $f_e = f_n = 1.2$ produce the largest variation in τ for a given F . The error $\delta(\tau_{sp})$ is obtained from the curves of Fig. 6 in exactly the same way as $\delta(\tau_T)$ is obtained from the curves in Fig. 1. The error $\delta(\tau_{sp})$ is treated as being wholly systematic.

Thus the total error $\delta(\tau)$ is given by

$$\delta(\tau) = \left\{ \left[\delta(\tau_F) \right]^2 + \left[\delta(\tau_T) \right]^2 \right\}^{\frac{1}{2}} + \delta(\tau_{sp}) . \quad (16)$$

Generally the statistical errors in the mean lives are less than 10%, whereas the errors due to uncertainties assigned to the stopping powers are about 15 to 25%.

Gas Backing

In order to measure mean lives in the range 5×10^{-12} sec $< \tau < 10^{-8}$ sec, it was decided to develop a method which used a gas backing instead of a solid material to slow down the recoiling nuclei. Because of experimental conditions it was necessary to have only one target and particle detector. However, instead of moving the γ -ray detector, a shift in energy was produced by changing the stopping power of the gas by varying the gas pressure.

As before, the Doppler-shift attenuation factor, F , is given by the ratio of the attenuated Doppler shift to the unattenuated Doppler shift. In the case where the mean energy, $\langle E_Y(P) \rangle_{\text{meas}}$, is a function of the pressure, we can write F as

$$F(\tau, P) = \frac{\langle E_Y(P) \rangle - E_0}{\Delta \langle E_Y \rangle_0} . \quad (17)$$

The unattenuated Doppler shift, $\Delta\langle E_\gamma \rangle_0$, can be calculated from the denominator of Eq. (14), where position 1 is the position of the γ -ray detector, and position 2 is taken to be 90° with respect to $\langle \vec{v}_0 \rangle_p$, the average direction of recoil.

A family of $F(\tau)$ curves, calculated in the manner described in Chapter II, is shown in Fig. 7. Each curve represents a different target thickness at a fixed gas pressure. The pressure was taken to be small in order to emphasize the difference in stopping powers of the target and the gas backing. Because of this, these $F(\tau)$ curves look "normal" only for zero target thickness or for very large target thicknesses. For intermediate thicknesses, the curves become a composite of the two extremes.

From these curves and Eq. (17), it is clear that for a finite target thickness and for $\tau > 10^{-11}$ sec, $F(\tau)$ is less than 1. For example, from Fig. 8, the curve for a $100 \mu\text{g}/\text{cm}^2$ thick target of ^{54}Fe has a maximum $F(\tau > 10^{-11} \text{ sec}) \approx 0.7$. If we define $F_{\text{max}} \equiv F(\tau > 10^{-11} \text{ sec})_{P=0}$ then Eq. (17) can be rewritten as

$$F_{\text{max}} - F(\tau, P) = \frac{[\langle E_\gamma(P=0) \rangle - \langle E_\gamma(P) \rangle]_{\text{meas}}}{\Delta\langle E_\gamma \rangle_0} = \frac{\Delta\langle E_\gamma(P) \rangle_{\text{meas}}}{\Delta\langle E_\gamma \rangle_0} \quad (18)$$

To be concise, we define $\Delta F_{\text{expt}} \equiv (\Delta\langle E_\gamma(P) \rangle_{\text{meas}}) / (\Delta\langle E_\gamma \rangle_0)$. The procedure then is to measure ΔF_{expt} , calculate the $F_{\text{max}} - F(\tau, P)$ curves, read ΔF_{expt} into the appropriate curve, and read out the experimental mean life.

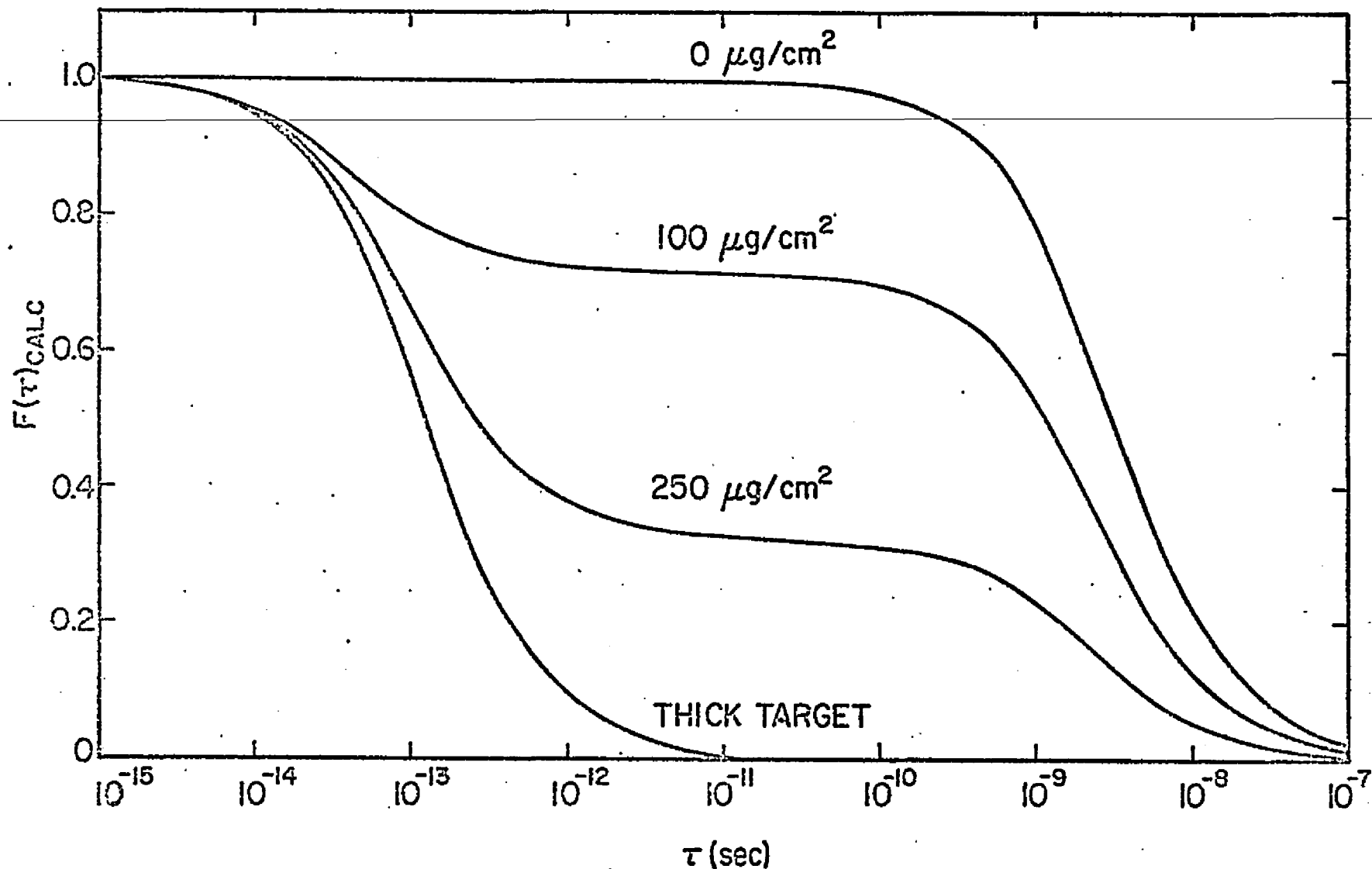


Fig. 7. F_{calc} vs. τ for a solid target with a gas backing.

$F_{\text{calc}}(\tau, |\vec{v}_0|)$ is plotted vs. τ for four thicknesses of ^{54}Fe with a 0.1 atmosphere krypton backing. $|\vec{v}_0|/c = 0.00463$ for recoiling ^{56}Fe nuclei.

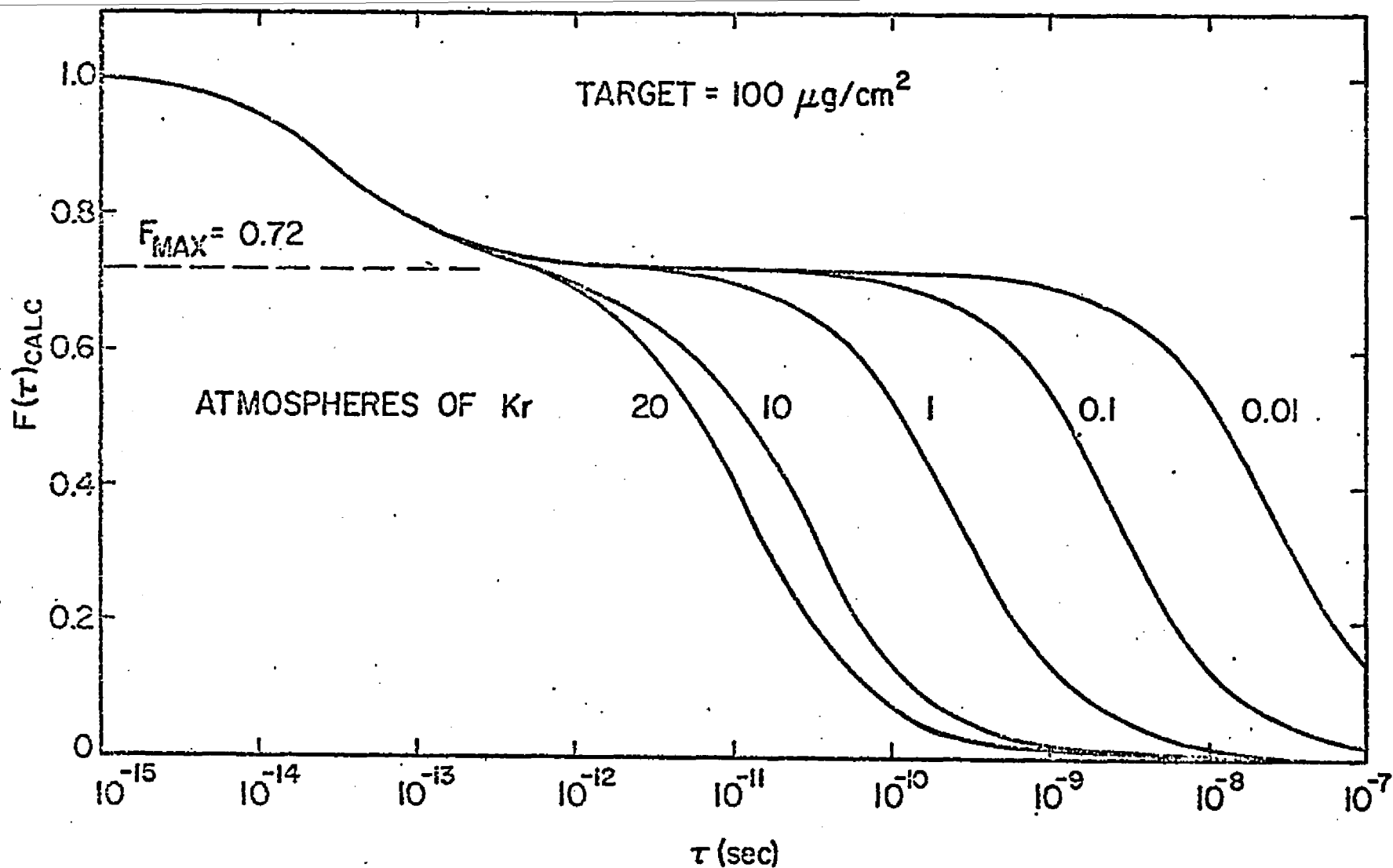


Fig. 8. F_{calc} vs. τ for several pressures in the gas backing.

$F_{\text{calc}}(\tau, |\vec{v}_0|)$ is plotted vs. τ for a $100 \mu\text{g}/\text{cm}^2$ target of ^{54}Fe and for five different pressures of the gas backing. $|\vec{v}_0|/c = 0.00463$ for the recoiling ^{56}Fe nuclei.

The Gas Chamber

The geometry for the gas chamber is shown in Fig. 9. The particle-detector-target arrangement with beam collimators is the same as that for one-half of the two-target chamber in Fig. 2. However, the γ -ray detector has been moved onto the beam axis to maximize the Doppler shift of the γ rays. The targets for gas backings were typically four times thinner than those used with solid backings. However, the γ -ray detector was placed almost twice as close to the target, thus making up the difference in counting rates. The electronics setup is identical to that shown in Fig. 4 for the two-target chamber. Because $\langle E_{\gamma}(P=0) \rangle$ and $\langle E_{\gamma}(P) \rangle$ were taken at different times, some care was taken in setting up the stabilizer and monitoring it for zero or gain changes.

Target Preparation

An important difference between the gas backing and solid backing methods is in the preparation and mounting of the targets. The gas chamber requires that the target be on the downstream side of the foil which serves as the beam window to the gas cell. In practice the target was evaporated directly onto the downstream side of the window.

The cleaning of the pressure foil, evaporation of the target materials, and weighing of the target are discussed in the section on solid backings.

The choice of materials for the beam window to the gas cell, while having to be of a higher atomic number than the target, involved two additional contradictory considerations. The window had to be thin enough for the beam to pass through without extreme attenuation, and yet

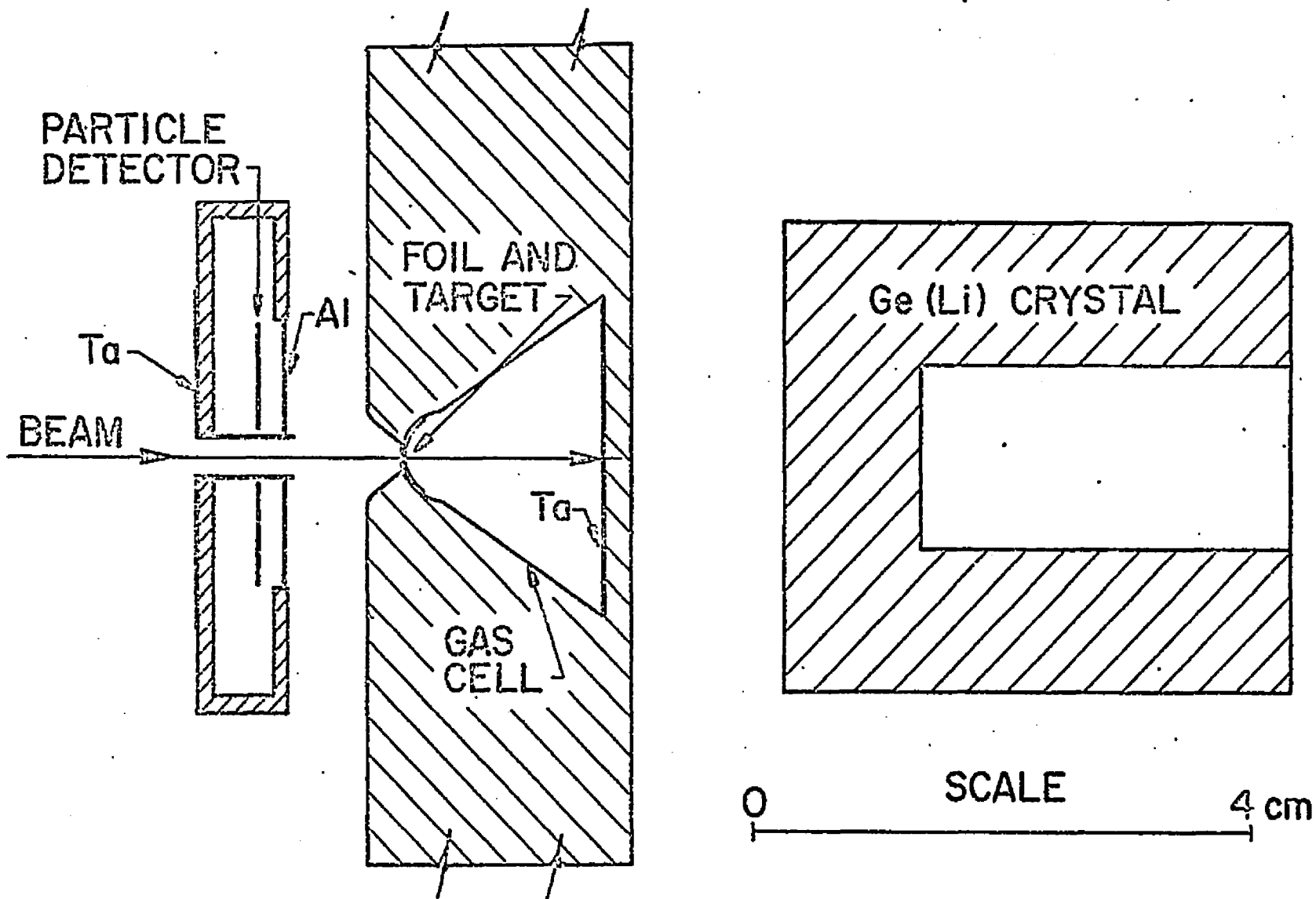


Fig. 9. Experimental arrangement of the gas-backing chamber.

Aluminum particle detector covering was varied from 0.001 to 0.003 in. in thickness as the deuteron beam was varied from 2 to 3.5 MeV.

it had to be strong enough to withstand a pressure of up to approximately 20 atmospheres. The two materials chosen were tantalum with a tensile strength of approximately 150,000 lbs/in², and havar, an iron-cobalt-nickel alloy, with a tensile strength of approximately 250,000 lbs/in². Havar is manufactured by the Precision Metals Division of the Hamilton Watch Company.

Mounting the foils to withstand the maximum pressure was critical. When no shear forces are involved, the bursting pressure of a vessel is given by

$$P_{\max} = \frac{A_{\text{wall}}}{A_{\text{section}}} T, \quad (19)$$

where A_{wall} is the cross-sectional area of the wall, A_{section} is the cross-sectional area of the vessel, and T is the tensile strength of the material. For a spherically- and a cylindrically-shaped vessel, Eq.

(19) becomes respectively

$$(P_{\max})_{\text{spherical}} = \frac{2\pi r t T}{\pi r^2} = \frac{2tT}{r}, \quad (20a)$$

and

$$(P_{\max})_{\text{cylindrical}} = \frac{2ltT}{2lr} = \frac{tT}{r}, \quad (20b)$$

where t is the thickness of the wall. Unfortunately, it was not feasible to form a spherical foil. However, it was rather easy to form a flat foil into a cylindrical shape.

Destructive tests were made with various foils and curvatures to test Eq. (20b). The test consisted of epoxying the foil to a cylindrical surface which had a 1/8 inch hole drilled in it, and then applying pressure until the foil burst. It was soon found that the best and most consistent results were obtained when the foil was epoxyed to a concave surface and the pressure was applied so as to push the foil against the surface. The results of the tests were in good agreement with Eq. (20b). Using a 1/8 inch radius of curvature, 0.0001 inch havar foil held better than 225 lbs/in² and 0.0005 inch tantalum foil held better than 450 lbs/in².

Analysis of Errors

The data reduction and error analysis for $\Delta F_{\text{expt}} = \frac{(\Delta \langle E_Y(P) \rangle_{\text{meas}})}{(\Delta \langle E_Y \rangle_0)}$ is the same as for F_{expt} described in the section for solid backings. Thus the contributions to ΔF_{expt} from statistical errors and from uncertainties in the calculations of the full shift are given by Eq. (15), which can be rewritten as

$$\frac{\delta(\Delta F_{\text{expt}})}{\Delta F_{\text{expt}}} = \left\{ \left[\frac{\delta(\Delta \langle E_Y \rangle_{\text{meas}})}{\Delta \langle E_Y \rangle_{\text{meas}}} \right]^2 + \left[\frac{\delta(\Delta \langle E_Y \rangle_0)}{\Delta \langle E_Y \rangle_0} \right]^2 \right\}^{\frac{1}{2}} \quad (21)$$

However, the use of the gas backing requires that a third term be added to Eq. (21) to account for uncertainties in the pressure of the gas backing.

Using the approximation of $F(\tau)$ for electronic stopping only, given by Eq. (9), we can write for the gas backing

$$F(\tau) \approx \frac{\alpha}{\alpha + \tau} \quad , \quad (22)$$

where the product of α times the density is approximately a constant. However, Eq. (22) is true only for zero target thickness. We can correct for this in the region of $\tau > 10^{-11}$ sec with the approximation

$$F(\tau) \approx \frac{\alpha}{\alpha + \tau} F_{\max} \quad , \quad (23)$$

where F_{\max} has been indicated in Fig. 8. Since the pressure of the stopping gas is proportional to the density, we can write $\alpha P = C$, where α is the stopping power constant of the gas, P is the pressure of the gas, and C is some constant. Substitution of this in Eq. (23) for α gives

$$F(\tau, P) \approx \frac{C}{C + P\tau} F_{\max} \quad . \quad (24)$$

Thus

$$\delta(F)_P = \frac{\partial F}{\partial P} \delta P \approx - \frac{C\tau F_{\max}}{(C + P\tau)^2} \delta P \approx - \frac{[F(\tau)]^2}{F_{\max}} \frac{\tau}{\alpha} \frac{\delta P}{P} \quad . \quad (25)$$

From the definition of ΔF we can deduce $\delta(\Delta F)$ to be $\delta(\Delta F) = \delta(F_{\max}) - \delta(F)$, where $\delta(F_{\max})_P = 0$. Therefore, using Eq. (25) we can write

$$\frac{\delta(\Delta F)_P}{\Delta F} = \frac{[F(\tau)]^2}{\Delta F(\tau) F_{\max}} \frac{\tau}{\alpha} \frac{\delta P}{P} \quad . \quad (26)$$

In practice $\delta P/P$ is at most approximately 2%. Thus for a measurement where $\tau = \alpha$, so that $F(\tau) = \frac{1}{2} F_{\max} = \Delta F(\tau)$, $\delta(\Delta F)_P/\Delta F$ is less than 1% and can usually be neglected. Therefore Eq. (21) is usually sufficient with no correction added for uncertainties in pressure.

The errors in τ , $\delta(\tau_{\Delta F})$ and $\delta(\tau_T)$, resulting from uncertainties in ΔF and in target thickness, can be obtained graphically from the $F_{\max} - F(\tau)$ curves shown in Fig. 10. Errors in τ , $\delta(\tau_{sp})$, due to uncertainties in the stopping powers of the target and backing are obtained from Figs. 11 and 12. The errors in τ are obtained from these curves in the same manner as they were obtained from corresponding curves for a solid backing, as discussed in the first section of this chapter.

Because of the normalization to F_{\max} , variations in the stopping power constants, f_e and f_n , have opposite effects in the backing from those in the target, as can be seen in Figs. 11 and 12. We have therefore chosen to split the errors in τ , due to uncertainties in the stopping power, into two parts, $\delta(\tau_{sp})_{\text{target}}$, obtained from Fig. 11, and $\delta(\tau_{sp})_{\text{backing}}$, obtained from Fig. 12. The maximum error in τ is thus obtained by combining errors in τ from the target and backing which result from varying the stopping power constants in opposite directions.

The total error in τ is then

$$\delta(\tau) = \{[\delta(\tau_{\Delta F})]^2 + [\delta(\tau_T)]^2\}^{\frac{1}{2}} + \delta(\tau_{sp})_{\text{target}} + \delta(\tau_{sp})_{\text{backing}} \quad (27)$$

As was the case with the solid backings, the statistical errors in the mean lives are generally less than 10%, whereas the errors due to uncertainties assigned to the stopping powers are about 15 to 25%.

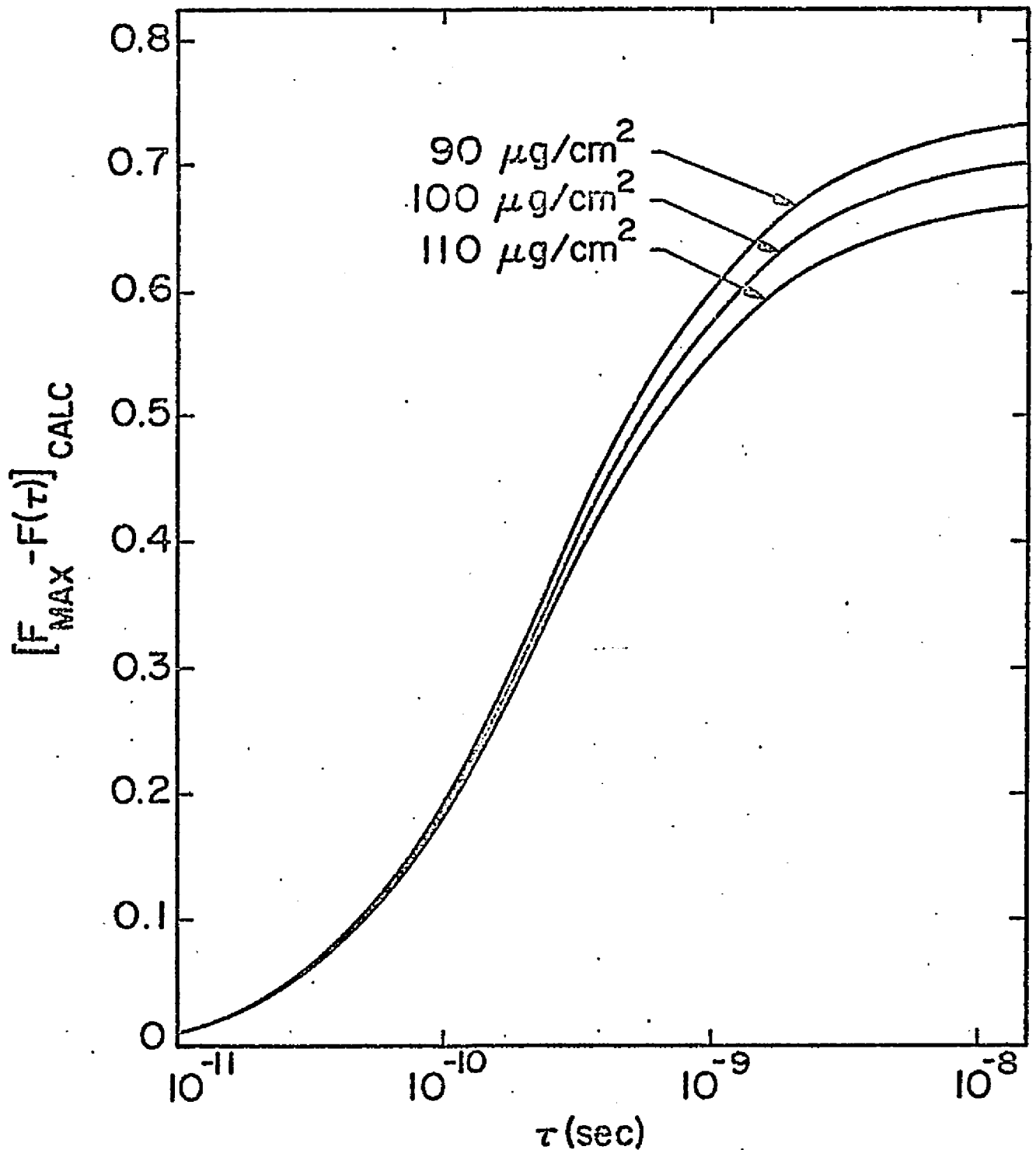


Fig. 10. $[F_{\text{max}} - F]_{\text{calc}}$ vs. τ for a solid target with a gas backing.

$[F_{\text{max}}(|\vec{v}_0|) - F(\tau, |\vec{v}_0|)]_{\text{calc}}$ is plotted vs. τ for three thicknesses of ^{54}Fe . Plots are for a pressure of 1 atmosphere in the krypton backing and $|\vec{v}_0|/c = 0.00463$ for the recoiling ^{55}Fe nuclei.

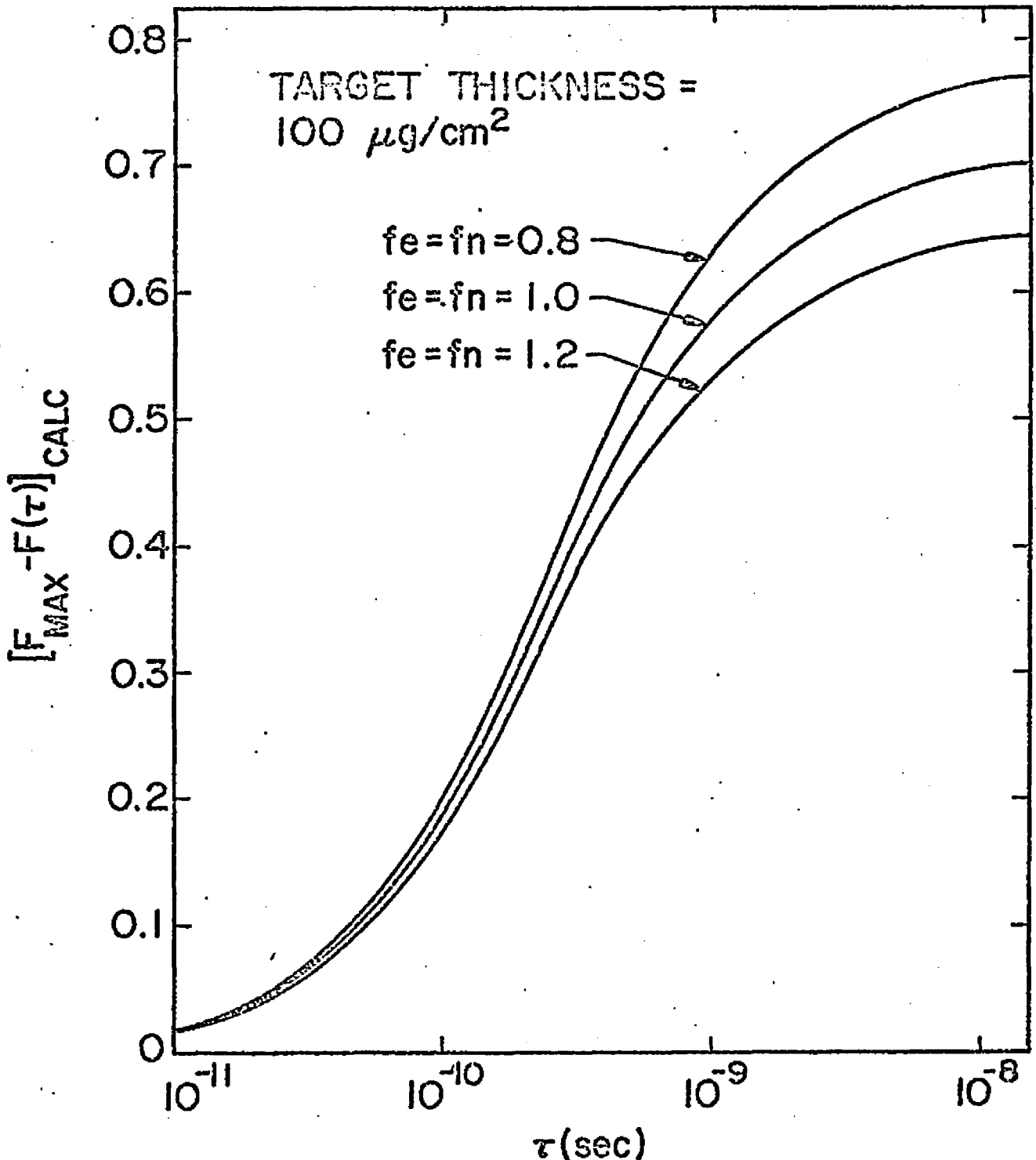


Fig. 11. Effects of stopping power uncertainties in the target on $[F_{\text{max}} - F]_{\text{calc}}$.

Effect of 20% uncertainty in stopping power of the target on $[F_{\text{max}}(|\vec{v}_0|) - F(\tau, |\vec{v}_0|)]$ is plotted vs. τ for a $100 \mu\text{g}/\text{cm}^2$ target of ^{54}Fe . Plots are for a pressure of 1 atmosphere in the krypton backing and $|\vec{v}_0|/c = 0.00463$ for the recoiling ^{56}Fe nuclei.

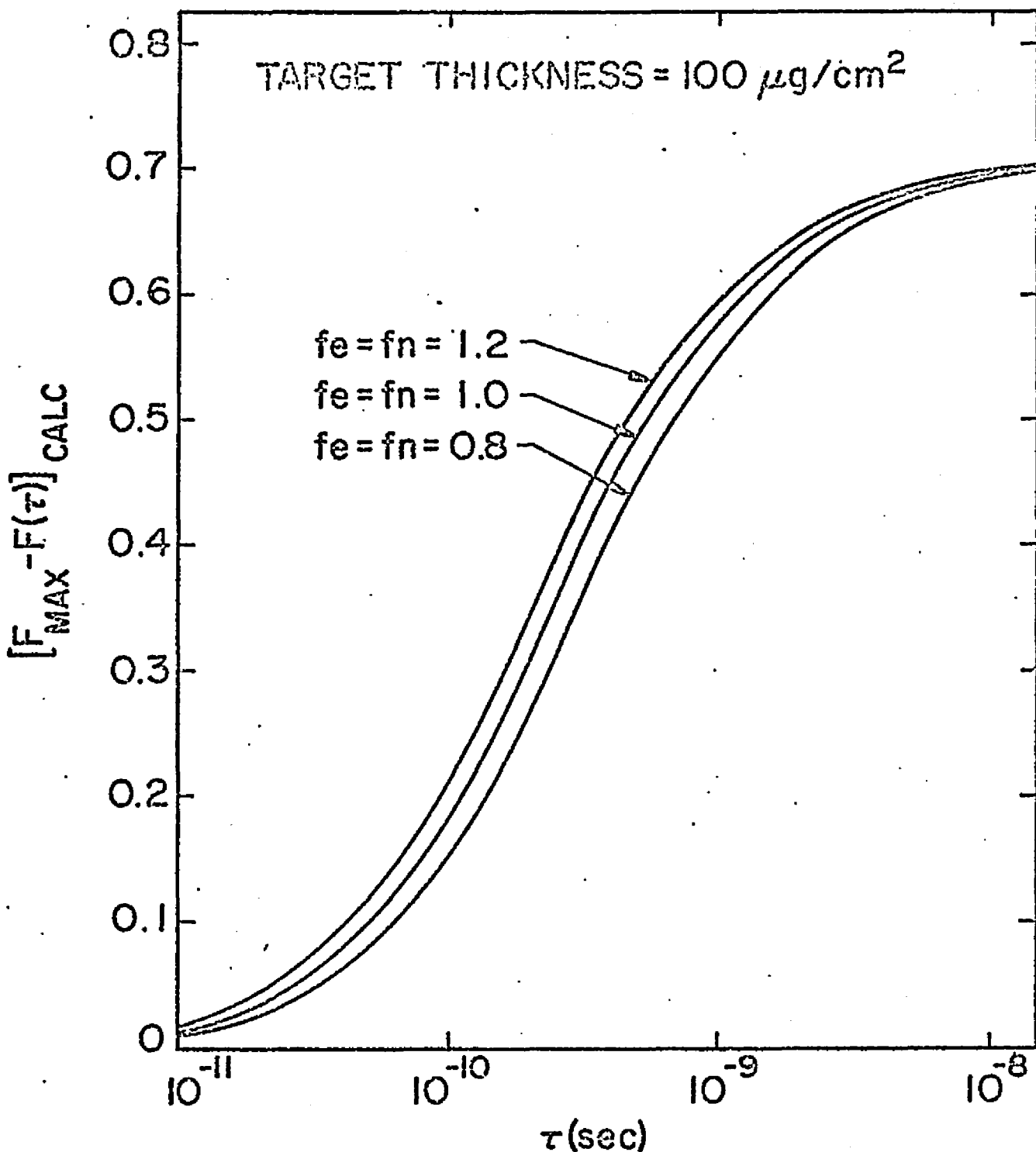


Fig. 12. Effects of stopping power uncertainties in the gas backing on $[F_{\text{max}} - F]_{\text{calc}}$.

Effect of 20% uncertainty in stopping power of the gas backing on $[F_{\text{max}}(|\vec{v}_0|) - F(\tau, |\vec{v}_0|)]_{\text{calc}}$ is plotted vs. τ for a $100 \mu\text{g}/\text{cm}^2$ target of ^{54}Fe . Plots are for a pressure of 1 atmosphere in the krypton backing and for $|\vec{v}_0|/c = 0.00463$ for the recoiling ^{55}Fe nuclei.

The gas chamber has been tested on the 2.6×10^{-10} sec mean life of the first excited state in ^{17}O , and on the 5×10^{-9} sec and 7×10^{-12} sec mean lives of the first two excited states in ^{25}Mg . Preliminary results show good agreement with the accepted mean lives of these states. Tests using the mean life of ^{17}O indicate that there was negligible effect on the measured mean life when the beam current was varied by a factor of more than 10.

CHAPTER IV

RESULTS

The results of the measurements on ^{20}F and ^{55}Fe will be presented in the following sections. The mean-life measurements were made using the Doppler-shift attenuation method outlined in the previous chapters. A summary of the results can be found in Tables IV, V, VI, VII, and VIII.

Excitation Energies in ^{20}F

A spectrum of protons obtained with a 2.25-MeV deuteron beam incident on a $250 \mu\text{g}/\text{cm}^2$ CaF_2 target is shown in Fig. 13. We have studied γ -rays in coincidence with protons to the 0.66-, 0.82-, 0.98-, 1.06-, 1.31-, 2.04-, 2.19-, 2.96-, 3.49-, and 3.53-MeV states in ^{20}F . The energies of these states are known to about ± 10 keV from magnetic analyses of proton spectra from (d,p) reactions. Recently the energies of some of the γ -ray transitions among these states have been measured with uncertainties of less than 1 keV [14]. Protons to all of these states could not be resolved individually, and in fact γ rays in coincidence with protons to a cluster of states were usually observed. However, the good resolution of the γ -ray detector enabled us to identify the individual states from which the γ rays originate. The requirement that γ rays be in time coincidence with protons to a given state or a given cluster of states greatly simplifies the resulting spectrum, so that

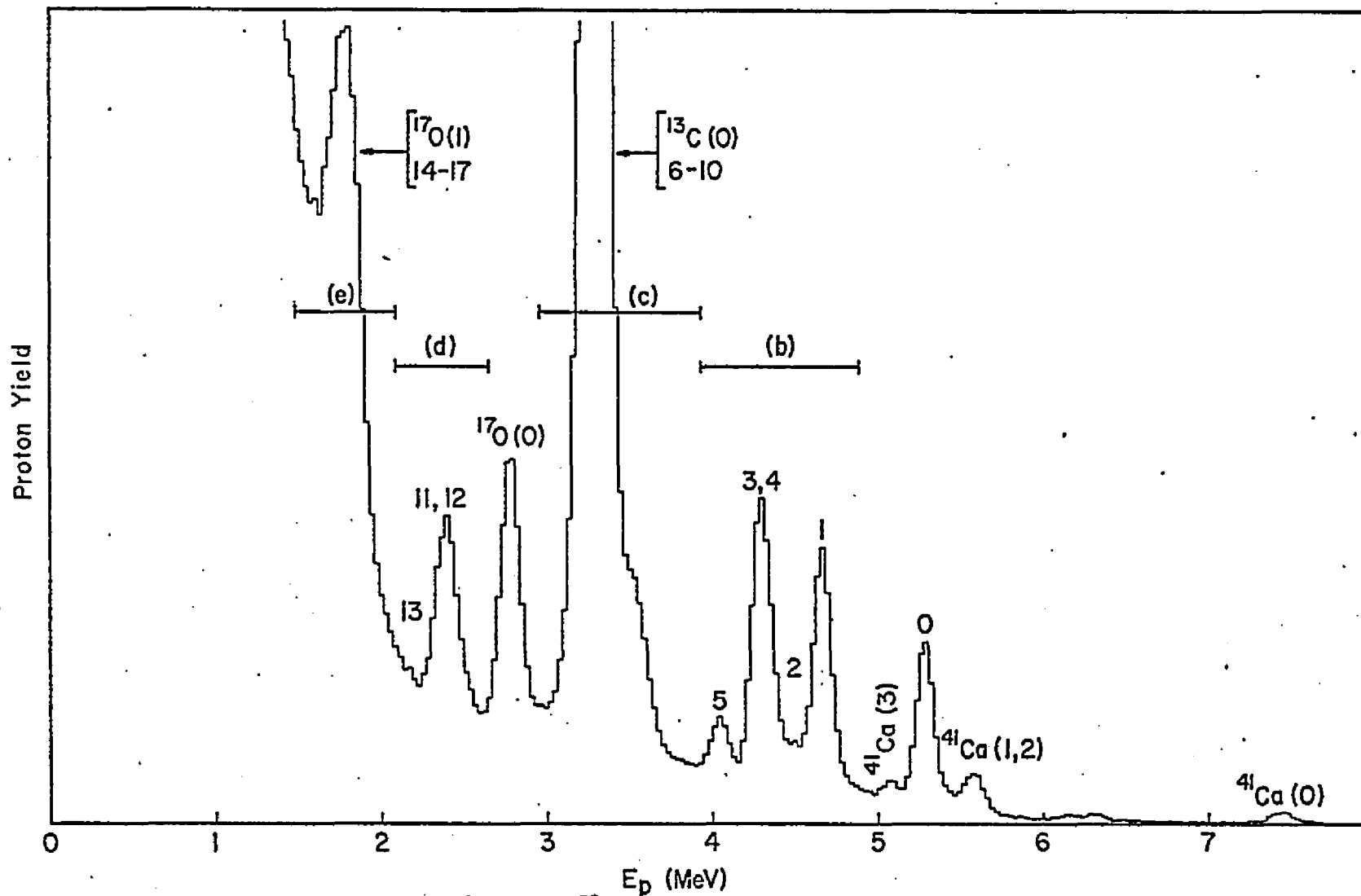


Fig. 13. Proton spectrum from the $^{19}\text{F}(d,p)^{20}\text{F}$ reaction.

This spectrum was obtained with the experimental arrangement of Fig. 2. Those proton groups resulting from calcium and from carbon and oxygen impurities in the target are also shown.

identification of γ rays with a given transition is relatively easy. For example, Fig. 14a shows the very complex singles γ -ray spectrum obtained with 2-MeV deuterons on CaF_2 , and Figs. 14b, 14c, 14d, and 14e show spectra in coincidence with protons in windows labeled b, c, d, and e respectively in Fig. 13. From spectra such as those in Fig. 14 the energies of some of the states in ^{20}F have been obtained with a precision of from 0.5 to 2.0 keV. The γ -ray energies were obtained from measurements made at 90° to the moving nuclei, and from the average of γ -ray energies measured at forward and backward direction with respect to the moving nuclei, so that no Doppler-shift correction was necessary in going from γ -ray energy to the energy difference between states of the transition. Also, in all cases, the decrease in γ -ray energy due to the recoil of the ^{20}F nucleus on emission of the γ ray was small compared to experimental errors, and was neglected. Energies of some states in ^{20}F are listed in Table IV.

The energy calibration of our system was obtained by locating the peaks from ^{22}Na and ^{60}Co sources in the singles spectrum. To check the accuracy of the energy calibration, the energies of annihilation radiation and of the 0.871-MeV γ rays from ^{17}O were determined from peaks which appeared as chance counts in the coincidence spectrum. From a number of such measurements we conclude that the energy calibration could be in error by as much as 0.3 keV for a γ ray with an energy of 900 keV. We have added this uncertainty directly to the statistical errors in determining centroids in order to obtain the errors quoted in Table IV.

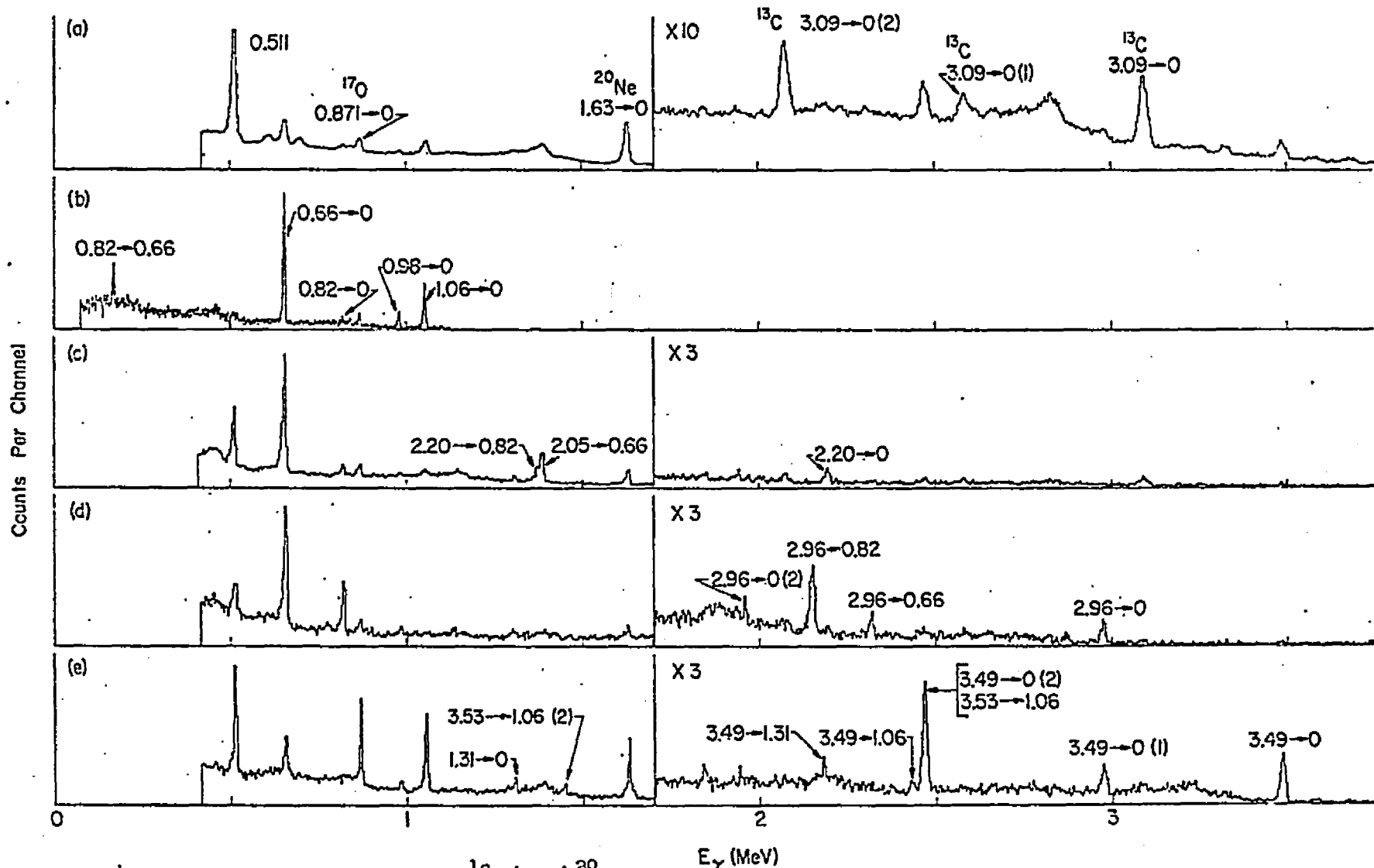


Fig. 14. γ -ray spectra from the $^{19}\text{F}(d,p)^{20}\text{F}$ reaction.

(a) γ -ray singles spectrum with labeled impurity transitions. (b) - (e) γ -ray coincidence spectra corresponding to the proton windows shown in Fig. 13. The observed transitions in ^{20}F are labeled when they first appear. Each ordinate scale is from zero to an arbitrary number of counts.

Table IV. Energies of some levels in ^{20}F .

Level	Energy (keV)	
	This work	Reference 14
0.66	655.4 ± 0.5	656.3 ± 0.5
0.82	822.6 ± 0.7	
0.98	983.4 ± 0.7	983.5 ± 0.7
1.06	1055.2 ± 0.6	1056.9 ± 1.0
1.31	1308.0 ± 0.9	1309.1 ± 0.7
2.96	2964.5 ± 2.0	2966.0 ± 2.0

Branching Ratios in ^{20}F

Table V shows our results for the branching in the decay of several states in ^{20}F . These results were obtained at only two or three angles, with respect to the recoiling nuclei, and are not true angular averages. However, none of the results quoted appeared to be sensitive to angle. The uncertainties are simply calculated standard deviations in the areas under individual peaks. The spectrum in coincidence with protons to the 1.31-MeV state showed a peak at 0.66 MeV which seems to indicate that a small fraction of the time this state may decay through the 0.66-MeV state. However, as indicated in Table V, this conclusion is quite uncertain.

Mean Lives of Excited States in ^{20}F

Fig. 15 illustrates the spectra, measured at about 24° and 156° with respect to recoiling ^{20}F nuclei, of γ rays in coincidence with protons to the 0.66-, 0.98-, 1.06-, and 1.31-MeV states in ^{20}F . These spectra were obtained with the collinear arrangement shown in Fig. 2. Doppler shifts of γ rays from those states were deduced directly from these and similar spectra. However, the direct yield of the 0.82-MeV state in the (d,p) reaction with 2-MeV deuterons was so low that for this state Doppler shifts were measured for γ rays from the cascade $2.96 \rightarrow 0.82 \rightarrow 0.0$ MeV. The Doppler shift attenuation factors so measured were then related to mean lives of the 0.82- and 2.96-MeV states by

$$F_{\text{measured}} = \frac{\tau_{0.82} F(\tau_{0.82}) - \tau_{2.96} F(\tau_{2.96})}{\tau_{0.82} - \tau_{2.96}} \quad (28)$$

Table V. Branching ratios of some levels in ^{20}F .

Level	Branch	Present work	Previous results	
0.82	0.82 \rightarrow 0	0.42 ± 0.04	0.37^a	0.25^b
	0.82 \rightarrow 0.66	0.58 ± 0.06	0.63^a	0.75^b
0.98	0.98 \rightarrow 0	≥ 0.95	$\geq 0.90^c$	
	0.98 \rightarrow 0.66	≤ 0.05	$\leq 0.10^c$	
1.31	1.31 \rightarrow 0	≥ 0.86		
	1.31 \rightarrow 0.66	≤ 0.14		
2.96	2.96 \rightarrow 0	0.24 ± 0.03		
	2.96 \rightarrow 0.66	0.14 ± 0.02		
	2.96 \rightarrow 0.82	0.62 ± 0.06		

^aReference 15.

^bReference 16.

^cReference 17.

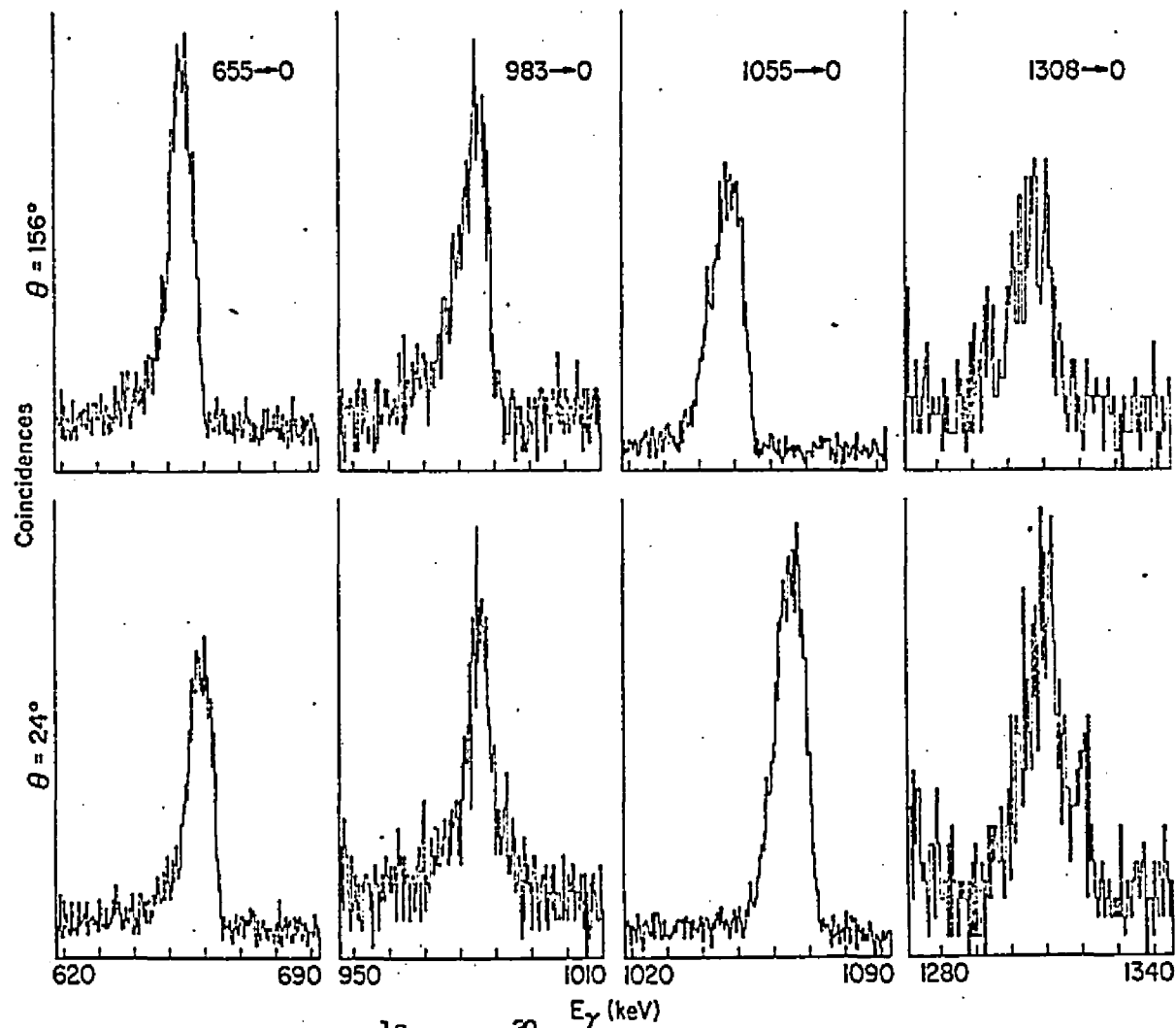


Fig. 15. Coincidence spectra from the $^{19}\text{F}(d,p)^{20}\text{F}$ reaction.

These spectra show the Doppler shifts of several transitions in ^{20}F . Shifts such as these were used to determine the mean lives of the various levels in ^{20}F . Each ordinate is from zero to an arbitrary number of counts. Spectra for the same transition have the same scale.

The derivation of this equation is given in Appendix D. As can be seen, to obtain information about the 0.82-MeV state from this equation it was necessary for us first to measure the Doppler shift attenuation factor for the γ rays emitted in the $2.96 \rightarrow 0.82$ -MeV transition. For the particular case considered, $\tau_{2.96}/\tau_{0.82} < 10^{-2}$, so that the application of Eq. (28) is trivial.

Since Doppler-shift measurements on the five lowest states were made with the proton window over all five states a small correction was made to the results for the 0.66-MeV γ rays to account for cascades from the 0.82-MeV level. This correction was made using Eq. (28) and its magnitude was determined from the area under the 0.82-MeV peak in the coincidence spectrum, the measured branching ratio of that state, and the variation with energy of the efficiency of the Ge(Li) crystal. The correction was about 4% of the attenuation factor of the 0.66-MeV peak. In addition, the Doppler shifts of 0.66-MeV γ rays were measured in the case where they were produced in the cascade $2.04 \rightarrow 0.66 \rightarrow 0.0$ MeV. This measurement was subject to a 12% correction similar to the one described above because γ rays from the cascade $2.19 \rightarrow 0.82 \rightarrow 0.66 \rightarrow 0.0$ MeV were also present.

Results of the Doppler-shift measurements are presented in Table VI. The initial average velocities of recoiling ^{20}F nuclei are listed in column 3; column 4 shows the measured energy differences between γ rays emitted in and opposite to the direction of these recoiling nuclei, and column 5, the Doppler-shift attenuation factor, is the ratio of column 4 to the calculated unattenuated shift. The errors in column 5

Table VI. Doppler shifts and mean lives in ^{20}F .

Energy Level (MeV)	Method of Population	$\frac{\langle \vec{v}_0 \rangle_p}{c}$	ΔE (keV)	F	τ_1^a	τ_2^b
					(10^{-13} sec)	(10^{-13} sec)
0.66	Direct	0.00850	4.50 ± 0.15	0.448 ± 0.021	$3.59^{+0.51}_{-0.39}$	
	Direct	0.00951	4.95 ± 0.11	0.473 ± 0.017	$3.40^{+0.35}_{-0.35}$	
	2.04	0.00784	3.29 ± 0.17	0.406 ± 0.026	$4.10^{+0.70}_{-0.55}$	
	Ave				$3.57^{+0.27}_{-0.24}$	$3.57^{+0.73}_{-0.78}$
0.82	2.96	0.00859	0.17 ± 0.18	0.014 ± 0.016	≥ 50	≥ 44
0.98	Direct	0.00834	3.02 ± 0.73	0.204 ± 0.051	$10.3^{+4.2}_{-2.8}$	
	Direct	0.00936	1.65 ± 0.38	0.102 ± 0.024	$22.5^{+8.5}_{-5.0}$	
	Ave				$12.8^{+3.8}_{-2.4}$	$12.8^{+6.2}_{-4.1}$
1.06	Direct	0.00831	16.52 ± 0.23	1.046 ± 0.028		
	Direct	0.00932	15.32 ± 0.26	0.888 ± 0.029		
	Direct	0.00959	17.33 ± 0.30	0.993 ± 0.030		
	Value Used			$F \geq 0.83$	≤ 0.86	≤ 0.92
1.31	Direct	0.00819	3.76 ± 0.54	0.195 ± 0.029	$10.6^{+2.9}_{-2.0}$	
	Direct	0.00946	2.74 ± 0.58	0.128 ± 0.028	$17.7^{+6.3}_{-4.2}$	

Table VI. Doppler shifts and mean lives in ^{20}F (continued).

Energy Level (MeV)	Method of Population	$\frac{\langle \vec{v}_0 \rangle_p}{c}$	ΔE (keV)	F	τ_1^a (10^{-13} sec)	τ_2^b (10^{-13} sec)
1.31 (cont.)	3.49	0.00704	3.27 ± 0.62	0.201 ± 0.040	$10.0 \begin{matrix} + 3.3 \\ - 2.3 \end{matrix}$	
				Ave	$11.1 \begin{matrix} + 2.0 \\ - 1.4 \end{matrix}$	$11.1 \begin{matrix} + 4.1 \\ - 2.9 \end{matrix}$
2.04 \rightarrow 0.66	Direct	0.00784	19.40 ± 0.22	0.992 ± 0.028	≤ 0.32	≤ 0.38
2.19 \rightarrow 0.82	Direct	0.00776	19.09 ± 0.50	1.007 ± 0.040	≤ 0.39	≤ 0.46
2.96	Direct	0.00859	42.8 ± 1.6	0.967 ± 0.048		
2.96 \rightarrow 0.82	Direct	0.00859	30.27 ± 0.70	0.946 ± 0.033		
			Ave	0.952 ± 0.027	≤ 0.51	≤ 0.62
3.49	Direct	0.00704	> 40	> 0.92	< 0.38	< 0.47
3.53 \rightarrow 1.06	Direct	0.00702	31.35 ± 0.48	1.024 ± 0.029	≤ 0.28	≤ 0.32

^aThe errors in the column marked τ_1 are the sum of uncertainties in τ due to errors in the measurement of F and the measurement of the target thickness.

^bThe errors in the column marked τ_2 include assumed uncertainties of 20% in the atomic and nuclear slowing down powers of the targets and backings.

include both the statistical errors in column 4 and a 2.0% uncertainty in the calculated full shift. Each of the values of F listed is the average of several individual measurements. Column 6 shows the mean lives or limits, and their errors, obtained from our values for F. These errors result from the errors in F and from an uncertainty of $\pm 50 \mu\text{g}/\text{cm}^2$ in the target thickness. Column 7 shows the increased errors which include a 20% uncertainty in the calculated electronic and nuclear stopping powers used to obtain the mean lives from the F-values. Where limits are quoted, they correspond to an F-value two standard deviations away from our measured value. For the three measurements on the 1.06-MeV level, the spread in results is much greater than the errors on the individual measurements. Since we do not understand this large spread, the limit to the mean life of this state was deduced by using a value of F two standard deviations below the lowest of these measurements. Recently a measurement of the mean lives of ^{20}F has been published [18]. A comparison of their results with those presented here is made in Table VII.

Mean Lives and Branching Ratios of
Excited States in ^{56}Fe

A spectrum of protons obtained with a 3.50-MeV deuteron beam incident on a $375 \mu\text{g}/\text{cm}^2$ thick ^{54}Fe target is shown in Fig. 16. Doppler shifts have been measured for all but the 11th of the first twelve excited states in ^{56}Fe . The measurements were made with the two-target chamber shown in Fig. 2 using $375 \mu\text{g}/\text{cm}^2$ thick targets of ^{54}Fe enriched to 98.2%. Figs. 17 and 18 illustrate some of the spectra, measured at

Table VII. Comparison of present results with those published recently.

Energy Level (MeV)	DSAM ^a (10 ⁻¹³ sec) Arizona	DSAM ^a (10 ⁻¹³ sec) Reference 18
0.66	3.57 + 0.73 - 0.78	3.7 ± 0.6
0.82	≥ 44	9 + 9 - 4
0.98	12.8 + 6.2 - 4.1	18 ± 4
1.06	≤ 0.92	0.45 ± 0.13
1.31	11.1 + 4.1 - 2.9	8 ± 3
2.04	≤ 0.38	0.37 ± 0.16
2.19	≤ 0.46	< 0.12
2.96	≤ 0.62	0.6 ± 0.4
3.49	< 0.47	0.44 ± 0.11
3.53	≤ 0.32	0.30 ± 0.15

^aDoppler-shift attenuation method.

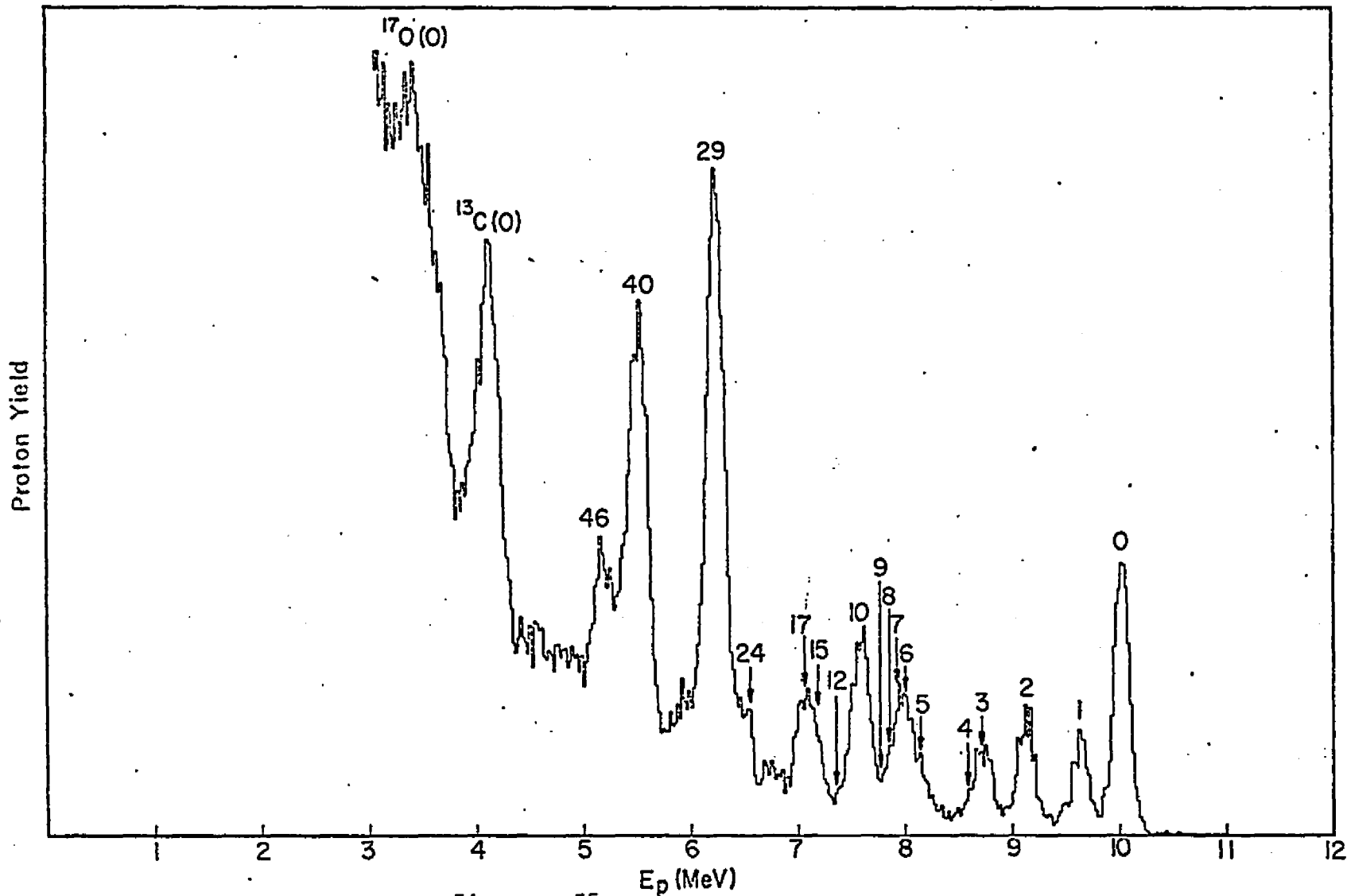


Fig. 16. Proton spectrum from the $^{54}\text{Fe}(d,p)^{55}\text{Fe}$ reaction.

This spectrum was obtained with the experimental arrangement of Fig. 2. Those proton groups resulting from carbon and oxygen impurities in the target are also shown.

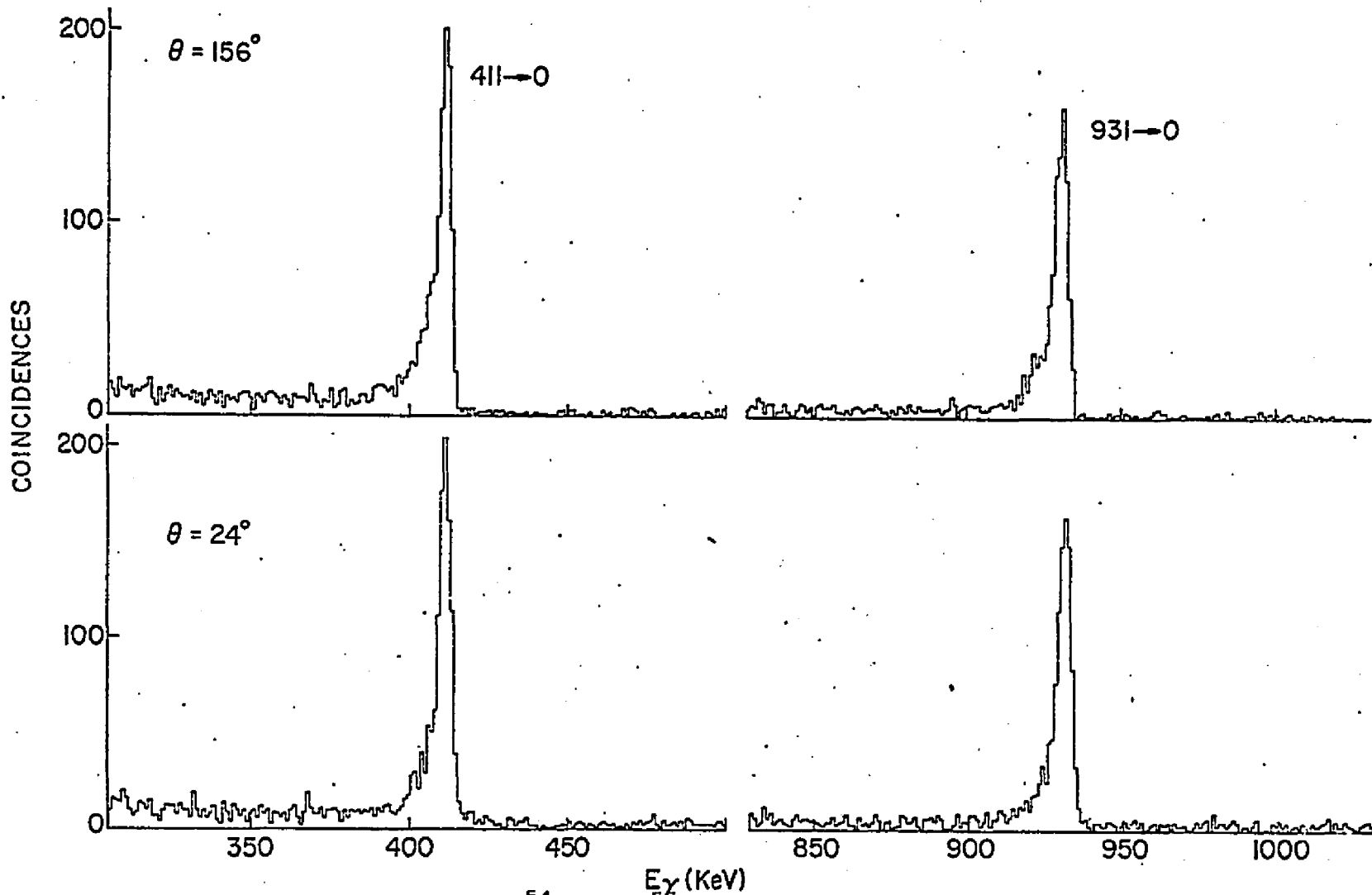


Fig. 17. Coincidence spectra from the $^{54}\text{Fe}(d,p)^{55}\text{Fe}$ reaction.

These spectra show the Doppler shifts of transitions from the first two excited states. Shifts such as these were used to determine the mean lives of the various levels in ^{55}Fe .

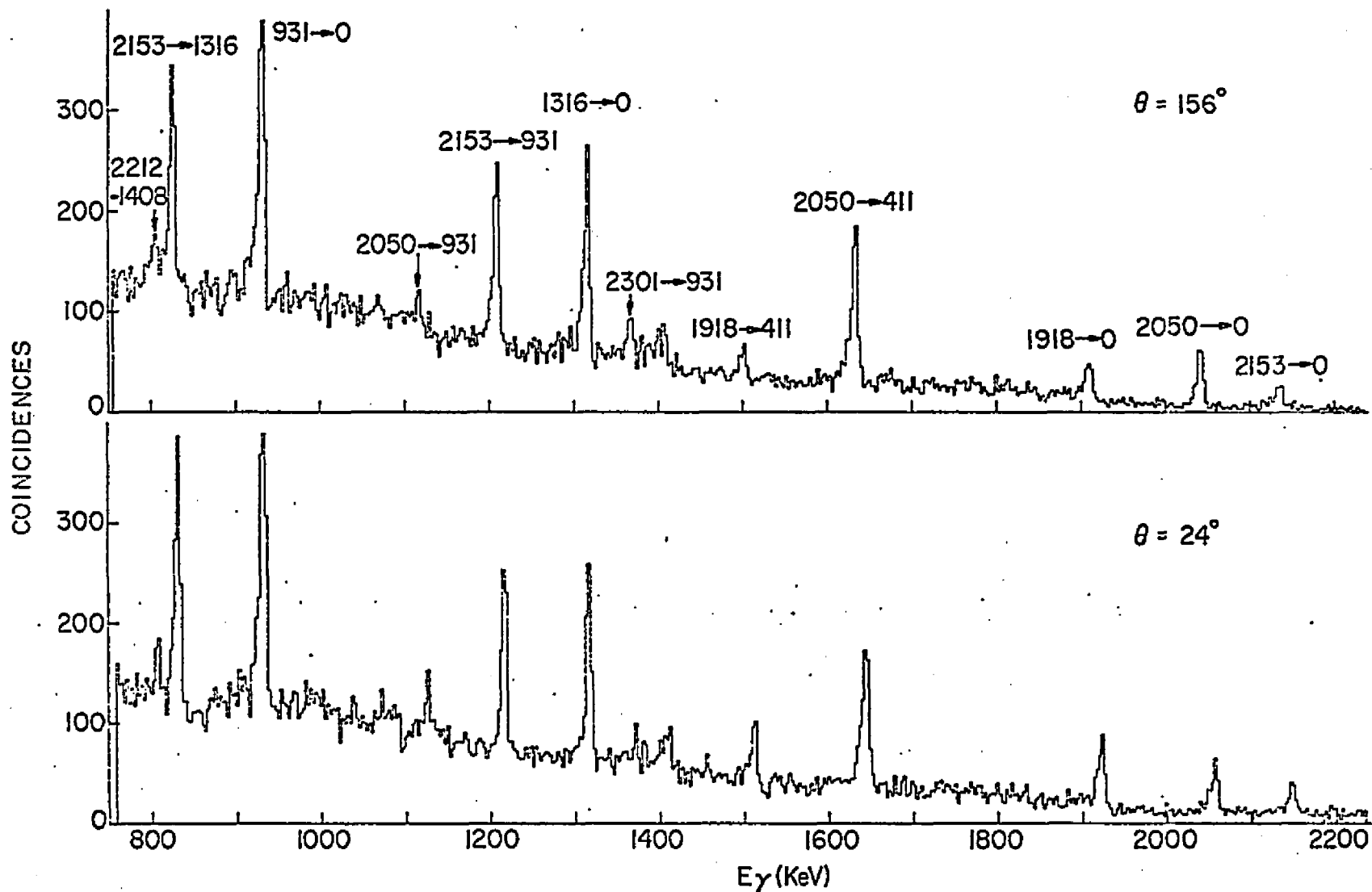


Fig. 18. Coincidence spectra from the $^{54}\text{Fe}(d,p)^{55}\text{Fe}$ reaction showing shifts of several transitions.

Doppler shifts such as these were used to determine the mean lives of the various levels in ^{55}Fe .

about 24° and 156° with respect to recoiling ^{56}Fe nuclei, of γ rays in coincidence with protons from respectively the first and second, and fifth through the ninth excited states in ^{56}Fe . The results are presented in Table VIII. As mentioned previously, each value of F listed is the average of several individual measurements. The errors in column 6 are a result of the errors in F and from an uncertainty of $\pm 25 \mu\text{g}/\text{cm}^2$ in the target thickness, whereas the errors in column 7 include a 20% uncertainty assigned to the calculated electronic and nuclear stopping powers. Where limits are quoted, they correspond to an F-value two standard deviations away from our measured value.

Because the first four levels were either zero shifted or very close to it, it was decided to measure these levels with the gas backing chamber, using a $50 \mu\text{g}/\text{cm}^2$ thick target of ^{54}Fe . Unfortunately because of low counting rates and resolution problems the 1408-MeV level could not be measured. The limits on τ of the first three levels were set at $\tau < 5$ psec. These results are entirely consistent with the results of Table VIII using solid backings.

While we did not make detailed measurements of branching ratios, the following information can be derived from the Doppler-shift data:

1. The 2050-keV level has approximately a 10% branch to the 931-keV level.
2. The 2589-keV level has approximately a 30% branch to the 931-keV level.

Table VIII. Doppler shifts and mean lives in ^{55}Fe .

Energy Level (MeV)	Transition	$\frac{\langle \vec{v}_0 \rangle_p}{c}$	ΔE (keV)	F	τ_1^a (10^{-13} sec)	τ_2^b (10^{-13} sec)
411	411 \rightarrow 0	0.00470	0.41 \pm 0.23	0.13 \pm 0.07	6.7 $\begin{matrix} + 8.8 \\ - 2.6 \end{matrix}$	6.7 $\begin{matrix} + 10.1 \\ - 3.8 \end{matrix}$
931	931 \rightarrow 0	0.00463	0.67 \pm 0.19	0.09 \pm 0.03	9.8 $\begin{matrix} + 5.7 \\ - 2.5 \end{matrix}$	9.8 $\begin{matrix} + 7.9 \\ - 3.7 \end{matrix}$
1316	1316 \rightarrow 0	0.00458	1.00 \pm 0.40	0.10 \pm 0.04	8.7 $\begin{matrix} + 6.8 \\ - 2.6 \end{matrix}$	8.7 $\begin{matrix} + 9.1 \\ - 4.0 \end{matrix}$
1408	1408 \rightarrow 931	0.00456	-0.8 \pm 0.4	0.0 \pm 0.12		
	1408 \rightarrow 0		-0.5 \pm 0.5	0.0 \pm 0.04		
	Ave			0.0 \pm 0.038		
1918	1918 \rightarrow 411	0.00449	10.96 \pm 1.12	0.96 \pm 0.10		
	1918 \rightarrow 0		13.83 \pm 0.69	0.94 \pm 0.05		
	Ave			0.944 \pm 0.044		
2050	2050 \rightarrow 931	0.00448	8.60 \pm 1.9	1.00 \pm 0.22		
	2050 \rightarrow 411		11.57 \pm 0.56	0.93 \pm 0.05		
	2050 \rightarrow 0		14.64 \pm 0.58	0.94 \pm 0.04		
	Ave			0.937 \pm 0.031		
2153	2153 \rightarrow 1316	0.00446	4.81 \pm 0.43	0.77 \pm 0.07		
	2153 \rightarrow 931		8.12 \pm 0.68	0.88 \pm 0.08		
	2153 \rightarrow 0		13.78 \pm 0.67	0.85 \pm 0.05		
	Ave			0.835 \pm 0.036		

Table VIII. Doppler shifts and mean lives in ^{55}Fe (continued).

Energy Level (MeV)	Transition	$\frac{\langle \vec{v}_0 \rangle_p}{c}$	ΔE (keV)	F	τ_1^a (10^{-13} sec)	τ_2^b (10^{-13} sec)
2212	2212 \rightarrow 1408	0.00445	3.1 ± 1.2	0.52 ± 0.21	$1.05 \begin{matrix} + 1.25 \\ - 0.58 \end{matrix}$	$1.05 \begin{matrix} + 1.53 \\ - 0.75 \end{matrix}$
2301	2301 \rightarrow 931	0.00444	≈ 5	≈ 0.50	≈ 1.1	
2470	(2470 \rightarrow 0) ^{2nd}	0.00442	17.6 ± 1.2	0.94 ± 0.07		
	2470 \rightarrow 0		15.2 ± 0.64	0.82 ± 0.04		
			Ave	0.850 ± 0.034	$0.25 \begin{matrix} + 0.06 \\ - 0.05 \end{matrix}$	$0.25 \begin{matrix} + 0.15 \\ - 0.08 \end{matrix}$
2589	2589 \rightarrow 931	0.00440	9.0 ± 2.3	0.73 ± 0.19		
	2589 \rightarrow 0		15.2 ± 0.88	0.79 ± 0.05		
			Ave	0.786 ± 0.048	$0.36 \begin{matrix} + 0.09 \\ - 0.08 \end{matrix}$	$0.36 \begin{matrix} + 0.21 \\ - 0.12 \end{matrix}$

^aThe errors in the column marked τ_1 are the sum of uncertainties in τ due to errors in the measurement of F and the measurement of the target thickness.

^bThe errors in the column marked τ_2 include assumed uncertainties of 20% in the atomic and nuclear slowing down powers of the targets and backings..

CHAPTER V

DISCUSSION OF RESULTS

The measurement of the mean life of a nuclear state, as was mentioned in the introduction, is a sensitive test of the matrix element which connects its initial state to the final state of the transition. This matrix element is usually expressed through the reduced matrix element which is defined by

$$B(\sigma\lambda) = (2J_i + 1)^{-1} \sum_{M_i, M_f} |\langle f | \mathcal{O}_{\lambda\mu} | i \rangle|^2, \quad (29)$$

where σ is the type of transition, electric or magnetic, and $\mathcal{O}_{\lambda\mu}$ is the corresponding operator; λ is the angular momentum carried away by the photon and μ is its projection on the z-axis; J_i is the angular momentum of the initial state and M_i is its projection on the z-axis; and M_f is the z-component of angular momentum of the final state. The angular momenta, and their z projections and parities must satisfy the following selection rules:

$$J_i + J_f \geq \lambda \geq |J_i - J_f|, \quad (30)$$

$$M_i - M_f = \mu \quad (31)$$

$$\pi_i \pi_f = (-1)^\lambda \quad \text{for } \sigma\lambda = E\lambda \quad (32a)$$

$$= -(-1)^\lambda \quad \text{for } \sigma\lambda = M\lambda \quad (32b)$$

The transition probability of a given type between two states is related to the corresponding reduced matrix element by [19]

$$T(\sigma\lambda)\downarrow = \frac{8\pi(\lambda + 1)}{\lambda[(2\lambda+1)!!]^2} \frac{1}{\hbar} \left(\frac{E_\gamma}{\hbar c}\right)^{2\lambda+1} B(\sigma\lambda)\downarrow, \quad (33)$$

where E_γ is the energy of the γ -ray transition in units of eV, \hbar is Planck's constant in units of eV sec divided by 2π , and c is the speed of light in units of cm/sec.

Now, if we restrict ourselves to γ -ray decay only, the measurement of the mean life, τ^k , of level k is equivalent to measuring the total transition probability, T^k , of that level. In particular,

$$\tau^k = \frac{1}{T^k} \quad (34)$$

and

$$T^k = \sum_{i=0}^{k-1} T_i^k, \quad (35)$$

where the T_i^k are the partial transition probabilities of level k to the lower lying levels. A measurement of the branching ratios is a relative measurement of the T_i^k . If these ratios are defined in terms of the transition of level k to level ℓ , they can be written as

$$R_{i\ell}^k = \frac{T_i^k}{T_\ell^k} \quad (36)$$

Thus T^k can be expressed in terms of only one partial transition probability and the branching ratios by substituting Eq. (36) into Eq. (35). The result is

$$T^k = T_{\ell}^k \sum_{i=0}^{k-1} R_{i\ell}^k \quad (37)$$

The T_{ℓ}^k are in turn sums of all the electric and magnetic multipole transition probabilities, $T_{\ell}^k(E\lambda)$ and $T_{\ell}^k(M\lambda)$. However, in practice, the intensity falls off rapidly with increasing λ . Therefore only the lowest order in λ , consistent with the selection rules given by Eqs. (30) to (32) for each type, is considered. The multipole mixing ratio is defined as the ratio of these two transition probabilities by

$$|\delta_{\ell}^k|^2 \equiv \frac{T_{\ell}^k(\sigma', \lambda+1)}{T_{\ell}^k(\sigma\lambda)} \quad (38)$$

Therefore,

$$T_{\ell}^k = T_{\ell}^k(\sigma\lambda) [1 + |\delta_{\ell}^k|^2] \quad (39)$$

Substitution of Eqs. (37) and (39) into Eq. (34), with some rearrangement, gives

$$T_{\ell}^k(\sigma\lambda) = \left\{ \tau^k [1 + |\delta_{\ell}^k|^2] \sum_{i=0}^{k-1} R_{i\ell}^k \right\}^{-1} \quad (40)$$

as the σ -type 2^{λ} multipole transition probability of level k to level ℓ . All quantities in Eq. (40) can be measured; the τ^k are measured by a method such as the one described in this work, the δ_{ℓ}^k are obtained from angular correlation studies, and the branching ratios are obtained by observing the transitions in a γ -ray spectrum and comparing the areas

under the respective peaks. It is these experimentally determined transition probabilities from Eq. (40) which will be compared with the theoretical predictions from Eq. (33). For both ^{20}F and ^{56}Fe these comparisons will be made to the extreme single-particle model or Weisskopf estimates. Also, in the case of ^{56}Fe more realistic calculations of the transition probabilities have been done. These were made by Lerner [6], using a version of the unified model.

The Extreme Single-Particle Model

The extreme single-particle model assumes that the total momentum of the nucleus is $J = l \pm \frac{1}{2}$, where l and $\frac{1}{2}$ are the orbital angular momentum and spin of the odd nucleon. Since only the lowest possible order of multipole is important we limit the discussion to $\lambda = \Delta J$ or $\Delta l = \lambda$, $\lambda \pm 1$. Parity considerations dictate that $\Delta l = \lambda$ for $E\lambda$, transitions and $\Delta l = \lambda - 1$ for $M\lambda$ transitions. The resulting $T(\sigma\lambda)$ thus determined contain two undetermined factors, one of which is an integral which depends on the nuclear radial wavefunctions and the other is a statistical factor. To approximate the first factor, the wavefunctions are assumed constant over the nucleus so that the integral can be evaluated explicitly. For the statistical factor the usual convention is to set it equal to 1, which is equivalent to assuming $l_f = 0$ so that $\lambda = l_i$. The resulting $E\lambda$ transition probability is called the Weisskopf estimate. The corresponding $M\lambda$ transition probabilities are found by multiplying the $T_w(E\lambda)$ by an inhibition factor which is the same for all multipole orders.

Because in the calculation of the Weisskopf estimates the radial wavefunctions are assumed to be constant, we expect that the resulting transition probabilities will be too large. For M1 transitions this has proved to be the case. Typical measured M1 transition probabilities are about one-seventh of the Weisskopf estimates [20]. Measured E2 transition probabilities, however, are generally equal to or greater than the Weisskopf estimates [20]. This indicates that electric-quadrupole transitions are not, in general, single-particle transitions, but result from collective motion of several particles.

While the Weisskopf estimates are admittedly crude, they do make it possible to compare the experimental results of one nucleus with those of another. D. H. Wilkinson [20] has tabulated much experimental data on transition probabilities and has plotted histograms of the ratios of $T_{\text{expt}}(\sigma\lambda)$ to $T_W(\sigma\lambda)$. This ratio, defined as

$$|M(\sigma\lambda)|^2 \equiv \frac{T_{\text{expt}}(\sigma\lambda)}{T_W(\sigma\lambda)} = \frac{B_{\text{expt}}(\sigma\lambda)}{B_W(\sigma\lambda)}, \quad (41)$$

is referred to as the transition probability in Weisskopf units. These histograms, plotted in Weisskopf units, permit the physicist to make a quick comparison of experimental results and to see systematic variations of transition probabilities between different regions of the periodic table. Comparisons with these histograms will be made in the discussion of the results of measurements on ^{20}F and ^{56}Fe .

Measurements on ^{20}F

Information about the properties of the low-lying energy levels of ^{20}F has been obtained mainly from angular distributions of protons produced in the $^{19}\text{F}(\text{d,p})^{20}\text{F}$ reaction [21,22,23], from γ -ray spectra produced by neutron capture in ^{19}F [14,16], and from particle- γ -ray correlations of radiations from the reactions $^{19}\text{F}(\text{d,p})^{20}\text{F}$ and $^{18}\text{O}(\text{}^3\text{He,p})^{20}\text{F}$ [15,17]. The latter reference contains a summary of most of the previous experimental information concerning ^{20}F . However, as discussed in detail by Bissinger et al. [17], the interpretations of these experiments are sufficiently ambiguous that spin and parity assignments for some of these states cannot be made with confidence. Attempts at theoretical interpretations of the structure of ^{20}F are rare, and have not been strikingly successful. Kurath [24] concluded that, in order to explain the magnetic moment of its ground state, the low-lying levels of ^{20}F must be rotational states which have a mixture of $K = 1$ and $K = 2$ rotational quantum numbers. More recently, Gunye and Warke [25], using a Hartree-Fock calculation, predict a low-lying rotational band of states with spins of $J = 2, 3, 4,$ and 5 . Halbert, McGrory, and Wildenthal [26] have estimated the quadrupole transition probability for the $0.66 \rightarrow 0.0$ -MeV transition from a shell-model calculation with effective interactions. Their result is approximately the same as obtained from the Nilsson rotational model.

Fig. 19 shows the energy level diagram of ^{20}F with known quantum numbers and branching ratios. A quantity which is uncertain is indicated by parentheses. Information concerning the properties of some of these states in ^{20}F is presented below.

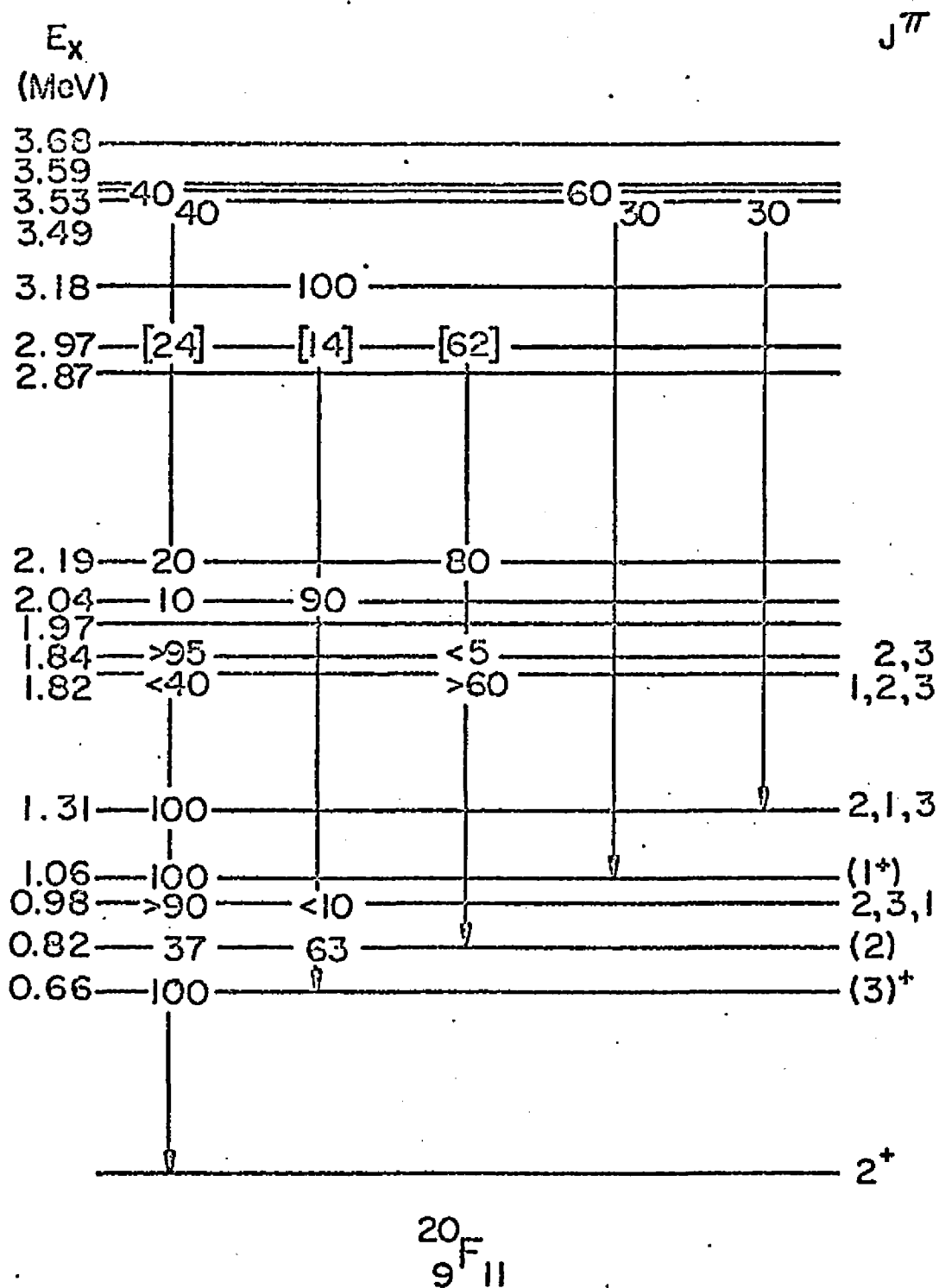


Fig. 19. Energy level diagram for the low-lying states in ^{20}F .

This diagram summarizes the known γ -ray decay schemes, spins, and parities. Branching ratios in brackets are from our measurements.

The 0.66-MeV Level

According to Bissinger et al. [17] particle- γ -ray correlations and (d,p) angular distributions limit the choice of quantum numbers for this state to 1^+ , 2^+ , and 3^+ . A recent, and as yet unpublished, measurement [27] of the vector analyzing power of $^{19}\text{F}(d,p)$ reaction leaving ^{20}F in its first excited state shows that the transferred neutron has $j_n = \frac{5}{2}$, and therefore that the spin of the 0.66-MeV state is 2 or 3. From the angular-correlation data, the most probable values of multipole mixing ratios are: for $J = 2$, $-1 \geq \delta \geq -3$, and for $J = 3$, $\delta = -0.015$. Combining our measured mean life for the 0.66-MeV state with a value of $\delta \leq -1$ yields an experimental E2 radiation width for which

$\Gamma_{\text{expt}}(E2)/\Gamma_W(E2) \equiv |M(E2)|^2 \geq 3000$, where Γ_W is the single-particle width calculated from the equations tabulated by Wilkinson [20]. This ratio is unrealistic, and leaves only the choice $J^\pi(0.66 \text{ MeV}) = 3^+$. The transition 0.66 MeV \rightarrow ground is then nearly pure M1, and $|M(M1)|^2 = 0.3$.

Bergqvist et al. [16] found some indication that the 1^- state in ^{20}F at 6.6 MeV decays through the 0.66-MeV state. The observation of this transition would be in contradiction with the conclusion that the 0.66-MeV state is 3^+ . However, the γ rays from transitions from the 1^- state to several low excited states in ^{20}F were not resolved, leaving the possibility that the spectrum produced by neutron capture in this state could be interpreted in another way.

The 0.82-MeV Level

From previous work [17] and from recent, as yet unpublished, extensions of that work [28], the most likely assignments for the spin of

this level and the multipole mixture of its transition to ground are $J = 2$, $\delta = 2.1$, or $J = 4$. An assignment of $J = 4$ to this level is not consistent with the (d,p) data [21]. These (d,p) data also favor a positive parity for this state. For $J = 2^+$, $\delta = 2$, our limit to the mean life gives $|M(E2)|^2 \leq 100$ and $|M(M1)|^2 \leq 2 \times 10^{-3}$. For $J = 4^+$ the ground state transition would be pure E2 and $|M(E2)|^2 \leq 120$.

The 0.98-MeV Level

As indicated in Table V, we were unable to observe a previously reported transition from this level to that at 0.66 MeV. We find the limit for this transition to be $\leq 5\%$. The spin of this level and the multipolarity mixture of the transition to the ground state in order of preference [17] are: $J = 2$, $\delta = +14.3$; $J = 3$, $\delta = -11.4$; and $J = 1$ with a wide range of possible mixing ratios. If $J = 2$ or 3 and if the parity of the state is positive, the transition would be nearly pure E2 and $|M(E2)|^2 \approx 200$. This is a very large enhancement. If the quantum numbers of the 0.98-MeV state were 1^+ we could obtain $|M(E2)|^2 \leq 200$, or $|M(M1)|^2 \leq 2.5 \times 10^{-2}$. If it were 1^- , $|M(E1)|^2 \approx 10^{-2}$ could be obtained. No definitive conclusions can be reached.

The 1.06-MeV Level

The quantum numbers of this level are most probably 1^+ [17], and a wide range of multipole mixtures are possible for its transition to the ground state. If the transition were all M1 the $|M(M1)|^2 \geq \frac{1}{3}$, and if it were all E2; $|M(E2)|^2 \geq 2.5 \times 10^3$. The latter number is huge, and indicates that the multipolarity of the transition is predominantly M1.

The 1.31-MeV Level

Again in order of preference [17], for this level, (a) $J = 2$, $\delta = 0.04$ or 1.9 ; (b) $J = 1$, $\delta = -0.7$, or (c) $J = 3$, $\delta = 0.42$. A strong transition observed to this state following thermal neutron capture rules out choice (c). Results of (d,p) angular distributions agree and show that the parity of this state is positive. Alternative (a) gives $|M(M1)|^2 = 1.3 \times 10^{-2}$ or $|M(E2)|^2 = 47$ and $|M(M1)|^2 = 2.8 \times 10^{-3}$. For alternative (b), $|M(E2)|^2 = 20$ and $|M(M1)|^2 = 9 \times 10^{-3}$.

For the excited states above 1.31 Mev only limits to mean lives were measured and hence not much information concerning the properties of these levels could be deduced. However, the observation that the 2.96-MeV level decays to the 0.0-, 0.66-, and 0.82-MeV levels with comparable intensities suggests that the spin of this level is 2 or 3.

Measurements on ^{55}Fe

Information about the low-lying levels of ^{55}Fe has been obtained mainly from angular distributions of protons produced in the $^{54}\text{Fe}(d,p)^{55}\text{Fe}$ reaction [3,29,30], from angular distributions of neutrons produced in the $^{55}\text{Mn}(p,n)^{55}\text{Fe}$ reaction [31], and from particle- γ -ray correlations of radiations from the reactions $^{54}\text{Fe}(d,p)^{55}\text{Fe}$ [32] and $^{55}\text{Mn}(p,n\gamma)^{55}\text{Fe}$ [33]. A summary of the experimental work published on ^{55}Fe can be found in Nuclear Data Sheets [34]. The energy level diagram of ^{55}Fe with known quantum numbers and branching ratios is shown in Fig. 20. Quantities which are uncertain are indicated by parentheses.

Because of the lack of experimental multipole mixing ratios for the transitions in ^{55}Fe , it is difficult to make meaningful comparisons

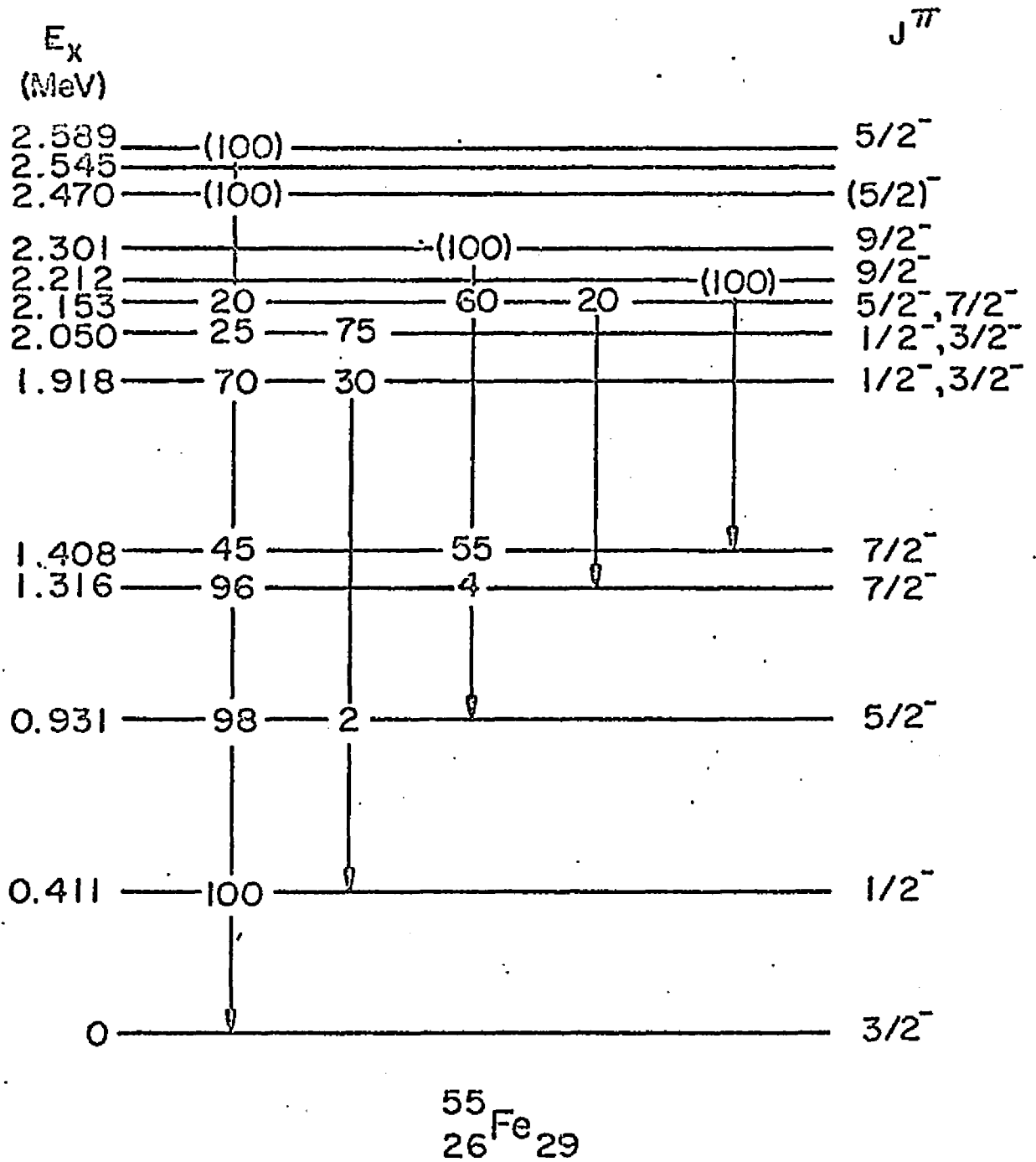


Fig. 20. Energy level diagram for the low-lying states in ^{55}Fe .

This diagram summarizes the known γ -ray decay schemes, spins, and parities.

with theoretical calculations. Where these mixing ratios are available, we have obtained the reduced M1 and E2 transition probabilities and Weisskopf estimates for those M1 and E2 transitions. These results are presented in Table IX. This table shows that except for the 2.212 \rightarrow 1.408-MeV transition the M1 transitions are inhibited by a factor of approximately 30. This is greater than the usual inhibition by about a factor of three. Except for perhaps the 1.408 \rightarrow 0.0-MeV transition, the E2 transition probabilities are enhanced over the Weisskopf estimates by about a factor of five to ten.

In contrast to ^{20}F , there have been many calculations made for ^{55}Fe and other isotopes with N or $Z = 29$. Since these isotopes all have a closed shell plus one in either neutrons or protons, they are all suitable for shell-model-type calculations. Shell-model calculations [3,4,5] and unified-model calculations [2,6], on ^{55}Fe have been reasonably successful in predicting spins, energies, and single-particle stripping widths. A comparison of the results of Refs. 2, 3, and 5 with experimental results has been made in Ref. 5.

The more successful of these calculations were done using some version of the unified model. The model, as will be discussed here, was introduced by de-Shalit [35]. In this model an odd-A nucleus is formed by weakly coupling the nearest even-even nucleus to a single particle in its lowest orbit. To keep the model general, the wavefunctions of the core states were unspecified in nature. The purpose of this model was to provide a general formalism which would be applicable to any type of core excitation and would predict both the single particle and collective properties of odd A nuclei.

Table IX. A summary of M1 and E2 reduced transition probabilities and Weisskopf estimates deduced from experimental measurements.

Transition (keV)	$10^{-13} \tau$ Arizona	$\delta \left(\frac{E2}{M1} \right)$ Ref. 31	$[\sum R_i]^{-1}{}^a$	$B(M1)_{\text{meas}}$ ($e^2 f_m^{-2}$)	$B(E2)_{\text{meas}}$ ($e^2 f_m^{-4}$)	$\frac{B(M1)_{\text{expt}}}{B(M1)_W}$	$\frac{B(E2)_{\text{expt}}}{B(E2)_W}$
931 \rightarrow 0	9.8 $^{+7.9}$ - 3.7	+ 0.40	0.98	6.7 $^{+4.1}$ - 3.0 $\times 10^{-4}$	161 $^{+97}$ - 70	0.033 $^{+0.021}$ - 0.019	13 $^{+7}$ - 6
1316 \rightarrow 0	8.7 $^{+9.1}$ - 4.0	=	0.96		228 $^{+195}$ - 116		18 $^{+15}$ - 9
1408 \rightarrow 0	> 10.0	=	0.45		< 66.4		< 5.2
2212 \rightarrow 1408	1.05 $^{+1.53}$ - 0.75	+0.12 $^{+0.15}$ - 0.12	1.0	1.1 $^{+2.7}$ - 0.7 $\times 10^{-2}$		0.57 $^{+1.41}$ - 0.34	
2470 \rightarrow 0	0.25 $^{+0.15}$ - 0.08	-0.70 $^{+0.55}$ - 1.40	1.0	1.1 $^{+0.6}$ - 0.8 $\times 10^{-3}$	117 $^{+174}$ - 112	0.056 $^{+0.029}$ - 0.042	9.3 $^{+13.8}$ - 8.9
2.589 \rightarrow 0	0.36 $^{+0.21}$ - 0.12	-0.84 $^{+0.28}$ - 0.35	1.0	6 $^{+7}$ - 3 $\times 10^{-4}$	80.5 $^{+52.3}$ - 45.3	0.03 $^{+0.04}$ - 0.01	6.4 $^{+4.2}$ - 3.6

^aEq. (36), and branching ratios from Ref. 33.

The simplest application of this model to ^{56}Fe would be to couple a $2p_{\frac{3}{2}}$ neutron to the 0^+ and 2^+ perfect vibrator core states of ^{54}Fe . This simple application predicts that the ground-state spin of ^{56}Fe is $\frac{3}{2}^-$ and that a multiplet of states with spins $\frac{1}{2}^-$, $\frac{3}{2}^-$, $\frac{5}{2}^-$, and $\frac{7}{2}^-$ will have an average energy equal to that of the 2^+ core state in ^{54}Fe . Furthermore, it predicts that an M1 transition from any member of the multiplet to the ground state is absolutely forbidden and that the reduced E2 transition probability for these same transitions is identical to that for the $2^+ \rightarrow 0^+$ transition in ^{54}Fe . It is indeed encouraging that trends in ^{56}Fe seem to follow these predictions. However, the existence of M1 transitions to the ground state from most levels indicates that the core and particle states are more complicated than assumed in this example.

Thankappan and True [7] have applied the model to $^{63}_{29}\text{Cu}_{34}$ where the coupling is no longer weak. They used an interaction Hamiltonian with dipole-dipole and quadrupole-quadrupole terms. However, because of the closeness in energy of the $2p_{\frac{3}{2}}$, $1f_{\frac{5}{2}}$, and $2p_{\frac{1}{2}}$ orbits, they included all three as possible orbits for the odd proton. Using this model, they accounted for both the single-particle and collective properties of ^{63}Cu , i.e., for both the single-particle stripping strengths and E2 transition rates.

Because ^{56}Fe has the same number of neutrons as ^{63}Cu has protons, and since the unified model has worked so well for ^{63}Cu , we have made a comparison of several of the low-lying levels of these two nuclei. The results, which are presented in Table X, show a number of interesting

Table X. A comparison of energies, multipole mixing ratios, and reduced E2 transition probabilities for the low-lying levels in ^{63}Cu and ^{55}Fe .

J_i	J_f	^{63}Cu			^{55}Fe		
		Transition Energy (keV)	δ^a	B(E2) ($e^2 f_m^4$) Ref. 7	Transition Energy (keV)	δ Ref. 31	B(E2) ($e^2 f_m^4$) Arizona
$\frac{1}{2}$	$\frac{3}{2}$	668	0.1	169	411		
$\frac{5}{2}$	$\frac{3}{2}$	961	0.47	166	931	± 0.40	$161 + 97$ $- 70$
$\frac{7}{2}$	$\frac{3}{2}$	1327	∞	153	1316	∞	$228 + 195$ $- 116$
$(\frac{5}{2})\frac{7}{2}$	$\frac{3}{2}$	1412		42	1408	∞	< 66

^aH. E. Gove, Phys. Letters 4, 249 (1963) [36].

similarities, namely, that the $B(E2)$ of the transitions from these levels to the ground state are all quite similar. As mentioned below the second $\frac{7}{2}$ state is believed to be found by lifting a neutron out of the $f_{7/2}$ shell, and thus has a different character than the other low-lying states.

Larner [6], using the same procedure as Thankappan and True [7], has calculated single-particle stripping strengths and reduced E2 transition probabilities for levels in ^{56}Fe . For core states he used the 0^+ and 2^+ states of ^{54}Fe . The odd neutron he considered to be in the $2p_{3/2}$, $1f_{5/2}$, or $2p_{1/2}$ orbits. The details of the formalism can be found in Refs. 6, 7, and 37. Using this model, he has obtained good fits with the experimental data to the energies, spins, and single-particle stripping widths for the low-lying levels in ^{56}Fe . Unfortunately, because many multipole mixing ratios have not been measured, the only $B_{\text{expt}}(E2)$ which we can calculate to compare with the calculations of Larner [6] is that of the $0.931 \rightarrow 0.0$ -MeV transitions.

However, Larner [38] has recently used his model to calculate multipole mixing ratios and branching ratios. Using these together with his calculated reduced transition probabilities, he has calculated mean lives for some of the low-lying levels in ^{56}Fe . These calculated mean lives together with our experimentally determined mean lives are presented in Table XI. In view of the difficulty of the calculations, the agreement of the calculated with the experimental mean lives is remarkable.

Because the calculations predict only one $\frac{7}{2}^-$ level at approximately 1.2 MeV, and only one $\frac{9}{2}^-$ level at approximately 2.4 MeV,

Table XI. Comparisons of the mean lives obtained from the results of measurements on ^{56}Fe with those predicted by the unified model.

Level (keV)	τ_{expt} (10^{-13} sec) Arizona	τ_{calc} (10^{-13} sec) Ref. 38
411	$6.7 \begin{smallmatrix} + 10.1 \\ - 3.8 \end{smallmatrix}$	4.10
931	$9.8 \begin{smallmatrix} + 7.9 \\ - 3.7 \end{smallmatrix}$	186.
1316	$8.7 \begin{smallmatrix} + 9.1 \\ - 4.0 \end{smallmatrix}$	16.7
1918	< 0.32	0.67
2050	< 0.28	1.27
2153	$0.28 \begin{smallmatrix} + 0.05 \\ - 0.06 \end{smallmatrix}$	0.20

Larner [6] has presented arguments that the 1.408-MeV level and the 2.212-MeV level, which decays only to the 1.408-MeV level, are at least partly $1f_{7/2}$ hole states coupled to the core. Our results in Table IX, which show that the E2 transition of the 1.408-MeV level is probably not very enhanced, indicate that this transition might be single particle in nature.

CHAPTER VI

SUMMARY AND CONCLUSION

The Doppler-shift attenuation method has become a very useful tool in the investigation of the properties of nuclear states. In some cases it is the only method which can be used, that is, when the mean life to be measured is less than 10^{-10} sec, the lower limit for electronic measurements, and also when the level does not decay to the ground state, thus ruling out Coulomb excitation and resonance fluorescence measurements. Particularly appealing to the experimentalist is the coincidence version of the Doppler-shift attenuation method with its wide applicability and great enhancement of signal-to-noise. Using this coincidence method we are able, in principle, to measure the Doppler shift of γ rays from any nuclear state which can be populated by means of a reaction of the form $X(a,b)Y^*$ where particle b can be detected by a charged particle detector.

The usefulness of this coincidence method, together with the introduction of the high resolution Ge(Li) γ -ray detector, were the incentives which prompted us to develop several experimental techniques which aid in measuring a large range of mean lives. Three of the most important were the calculation of the full Doppler shift, development of the two-target chamber, and development of the gas backing chamber.

The calculation of the full Doppler shift, which has been described in detail by Wozniak [1], permits us to measure Doppler shifts,

with confidence, up to 90% of the full Doppler shift. Because of the importance of this calculation a great deal of time was spent measuring known lifetimes which would produce an experimental full shift to compare with our calculation. A summary of these comparisons is given by Wozniak [1].

The two-target chamber was developed in order to eliminate the effects of such sources of error as zero and gain changes in our γ -ray spectrometer system. This chamber has reduced the experimental errors to the point where the measurement of the Doppler-shift attenuation factor in the range of $0.1 < F_{\text{expt}} < 0.9$ is now almost routine.

We have developed the gas backing chamber to extend the range of measurable mean lives beyond the range which can be measured using solid backings. In principle there is no definite upper limit to the mean life which can be measured using the gas backing. However, it is not practical to use this method to measure mean lives longer than 5×10^{-9} sec, where electronic methods can easily be used. With these two chambers we are able to measure mean lives in the range of 5×10^{-9} sec $\leq \tau \leq 5 \times 10^{-14}$ sec.

We would like to point out one of the frustrations of making an experimental measurement which depends on other experiments or calculations. While the errors in the Doppler-shift attenuation measurement are limited for the most part by the statistics of the experiment, the calculation of the mean life from the measured attenuation factor is dependent on the stopping power equations. These stopping power equations are uncertain for our region of interest by about 20%. Thus, while our

measurements normally have less than 10% error, we must increase the errors by approximately another 20% to allow for uncertainties in the stopping power equations. This illustrates the need of low energy experimental stopping power measurements.

The methods which we have described have been used to obtain Doppler shifts from 10 states in ^{20}F and 11 states in ^{56}Fe . From these we have obtained three mean lives in ^{20}F and eight in ^{56}Fe . Our ^{20}F results on transition probabilities are not in disagreement with the spin assignments or multipole-mixture measurements of Bissinger et al. [17]. In addition, our measurements, combined with appropriate multipole mixtures, indicate that the spin quantum number of the 0.66-MeV state is 3 and that its parity is positive. Our results on ^{20}F and their analysis strikingly illustrate the difficulty encountered in obtaining unambiguous information about the properties of levels in this nucleus.

Our results on ^{56}Fe are not as informative as they could be, because of the lack of experimental information concerning the multiplicities of the various transitions. At this time only general trends can be indicated. From comparisons with predictions of the unified model and comparisons with ^{63}Cu , which is described quite well by the unified model, it appears that this model could be used for ^{56}Fe , thereby greatly simplifying shell model calculations for this nucleus. In addition, Lerner's [38] calculations of the mean lives for the low-lying levels in ^{56}Fe using the unified model show reasonably good agreement with our measured mean lives. When the experimental multipole mixing ratios become available a more meaningful comparison with the predictions of the unified model will be possible and should prove to be quite interesting.

APPENDIX A

THE CALCULATION OF $\langle \hat{r} \rangle_{\gamma}$

The calculation of $\Delta \langle E_{\gamma} \rangle_0$ for the denominator of Eq. (14),

$$\Delta \langle E_{\gamma} \rangle_0 = \frac{E_0}{c} \langle \vec{v}_0 \rangle_p \cdot \left[\langle \hat{r} \rangle_{\gamma 1} - \langle \hat{r} \rangle_{\gamma 2} \right], \quad (A1)$$

requires the vector $\langle \hat{r} \rangle_{\gamma i}$. This vector is the average of all γ -ray directions, \hat{r} , weighted by the efficiency per unit solid angle for the γ -ray detector in the i^{th} position. This average, which contains all the geometrical information of the γ -ray detector, is given by

$$\langle \hat{r} \rangle_{\gamma} = \frac{1}{N} \int d\mathbf{r} \hat{r} \rho(\hat{r}) = \langle x' \rangle_{\gamma} \hat{i}' + \langle y' \rangle_{\gamma} \hat{j}' + \langle z' \rangle_{\gamma} \hat{k}, \quad (A2)$$

where $N = \int d\mathbf{r} \rho(\hat{r})$, and $\rho(\hat{r})$ is the efficiency function per unit solid angle. The primed coordinate system is chosen so as to simplify the limits of integration as much as possible.

Planes of symmetry in the γ -ray detector, if properly orientated, can greatly simplify the calculation of $\langle \hat{r} \rangle_{\gamma}$ when the proper primed coordinate system is chosen. By inspection of Eq. (A2), it can be seen that if the primed coordinate system is chosen so that any two coordinate axes lie in a plane of symmetry of the γ -ray detector, the average over the third coordinate vanishes. That is, $\langle \hat{r} \rangle_{\gamma}$ lies in the plane of symmetry.

Thus if a cylindrical or rectangular γ -ray detector with two perpendicular planes of symmetry is positioned in such a way that both planes of symmetry contain any two of the coordinate axes, $\langle \hat{r} \rangle_{\gamma}$ must lie along the intersection of the planes of symmetry. Wozniak [1] has discussed the calculation of $\langle \hat{r} \rangle_{\gamma}$ in detail for this case. In this appendix we will give a method for calculating $\langle \hat{r} \rangle_{\gamma}$ when the primed coordinate system can be chosen so that at most only one plane of symmetry contains two coordinate axes. Such a case is illustrated by the two-target chamber in Fig. 2, where the plane of symmetry is parallel to the paper and includes the beam. We will choose the primed coordinate system such that the origin lies at the target position and the x' - y' plane lies in the symmetry plane of the γ -ray detector with the x' -axis lying along the beam direction.

Fig. 21 is an enlarged view of the γ -ray detector which illustrates the limits of integration for spherical coordinates. For this case the z' -component vanishes and Eq. (A2) becomes

$$\langle \hat{r} \rangle_{\gamma} = \frac{1}{N} \int_{\theta'_{\min}}^{\theta'_{\max}} d\theta' \int_{\theta'_{\min}}^{\theta'_{\max}} d\theta' [(\sin\theta' \cos\varphi') \hat{i} + (\sin\theta' \sin\varphi') \hat{k}] \rho(\theta', \varphi') \quad (\text{A3})$$

Since the integral of θ' is symmetric about $\theta' = \pi/2$, we can set $\int_{\theta'_{\min}}^{\theta'_{\max}} d\theta' = 2 \int_{\pi/2}^{\theta'_{\max}} d\theta'$. Because Eq. (A3) must be integrated numerically, this last step increases the accuracy of the integration for a given number of integration points.

We do this numerical integration by the method of Gaussian Quadratures. The change of variables is as follows:

Fig. 21. A three-dimensional view of the γ -ray detector crystal.

This enlarged view of the γ -ray detector crystal is shown in the geometry of the two-target chamber. Planes of symmetry in the detector crystal as well as ϕ'_{\min} , ϕ'_{\max} , and θ'_{\max} are indicated.

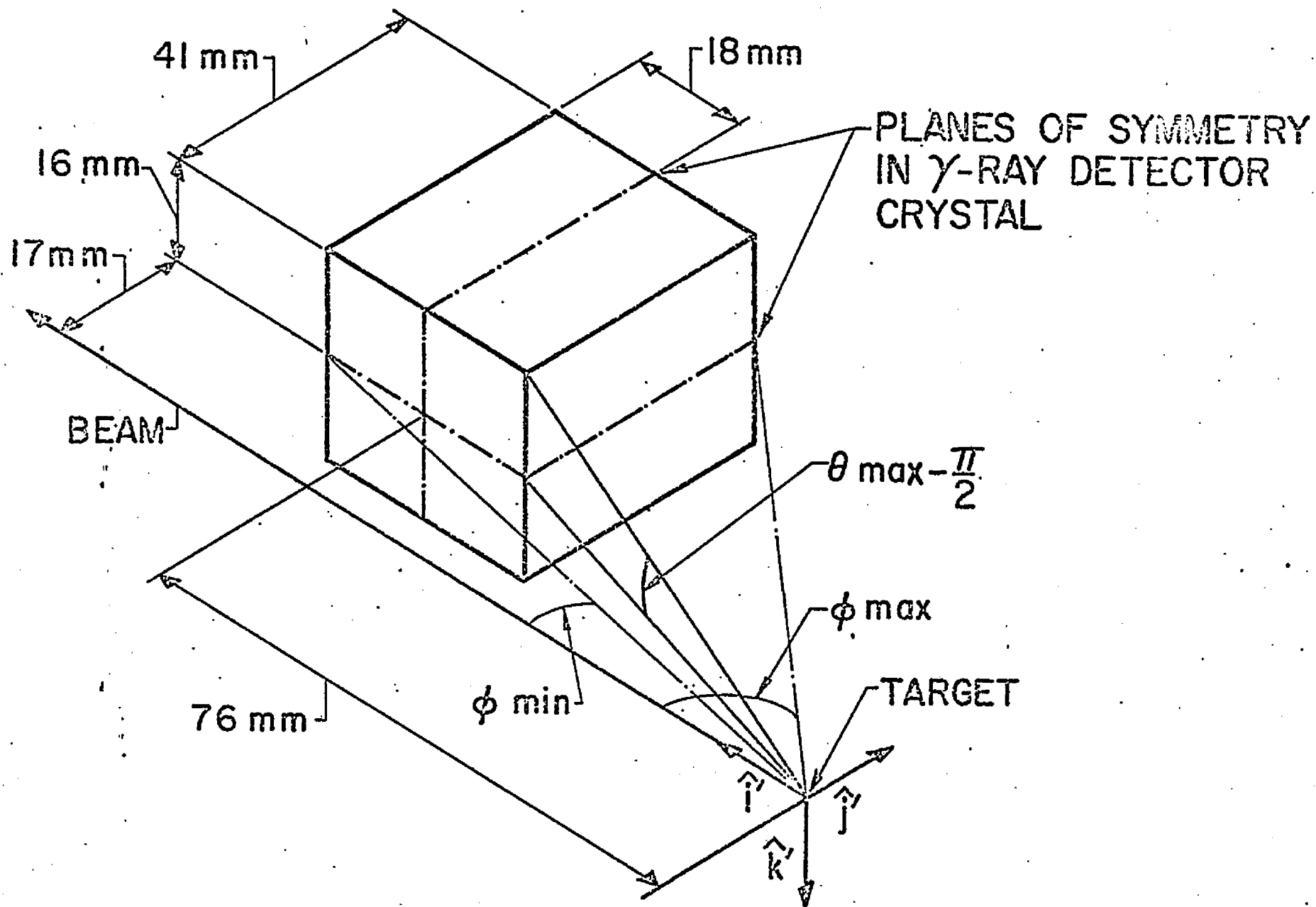


Fig. 21. A three-dimensional view of the γ -ray detector crystal.

$$\theta'_i = \frac{\theta'_{\max} - \frac{\pi}{2}}{2} x_i + \frac{\theta'_{\max} + \frac{\pi}{2}}{2}, \quad (\text{A4})$$

and

$$\theta'_j = \frac{\theta'_{\max} - \theta'_{\min}}{2} x_j + \frac{\theta'_{\max} + \theta'_{\min}}{2}, \quad (\text{A5})$$

where the x_i are the Gaussian integration points which have a range of $-1 < x_i < 1$. These points together with their weighting functions are tabulated [39] for values of n up to $n = 96$. We have chosen to use $n = 5$ so that there are five θ'_i , five θ'_j , and twenty-five $\rho(\theta'_i, \varphi'_j)$. These $\rho(\theta'_i, \varphi'_j)$ are taken to be the thickness of the detector crystal as seen by a γ ray emitted at that particular θ'_i and φ'_j .

The method for calculating $\langle \hat{r} \rangle_\gamma$ is as follows. The values of θ'_{\max} , φ'_{\min} , and φ'_{\max} are found from Fig. 21. The Eqs. (A4) and (A5) are used to calculate the θ'_i and φ'_j . These angles, together with a scale drawing of the detector crystal, are used to calculate the values for the $\rho(\theta'_i, \varphi'_j)$. Finally, Eq. (A3) is integrated numerically.

For the limit of high energy γ rays, the $\rho(\theta'_i, \varphi'_j)$ are found by measuring the distance that a particular ray traverses in the crystal at that particular θ'_i and φ'_j . The measurements are taken from an enlarged view of the crystal looking down along the $-z'$ direction. Such a drawing is shown in Fig. 22. The φ'_j are represented by lines and the θ'_i are represented by arcs that a cone of a particular θ'_i will make as it comes through the surface of the detector. The dashed arcs are at the surface of the inner dead region. Since the measured distance is a

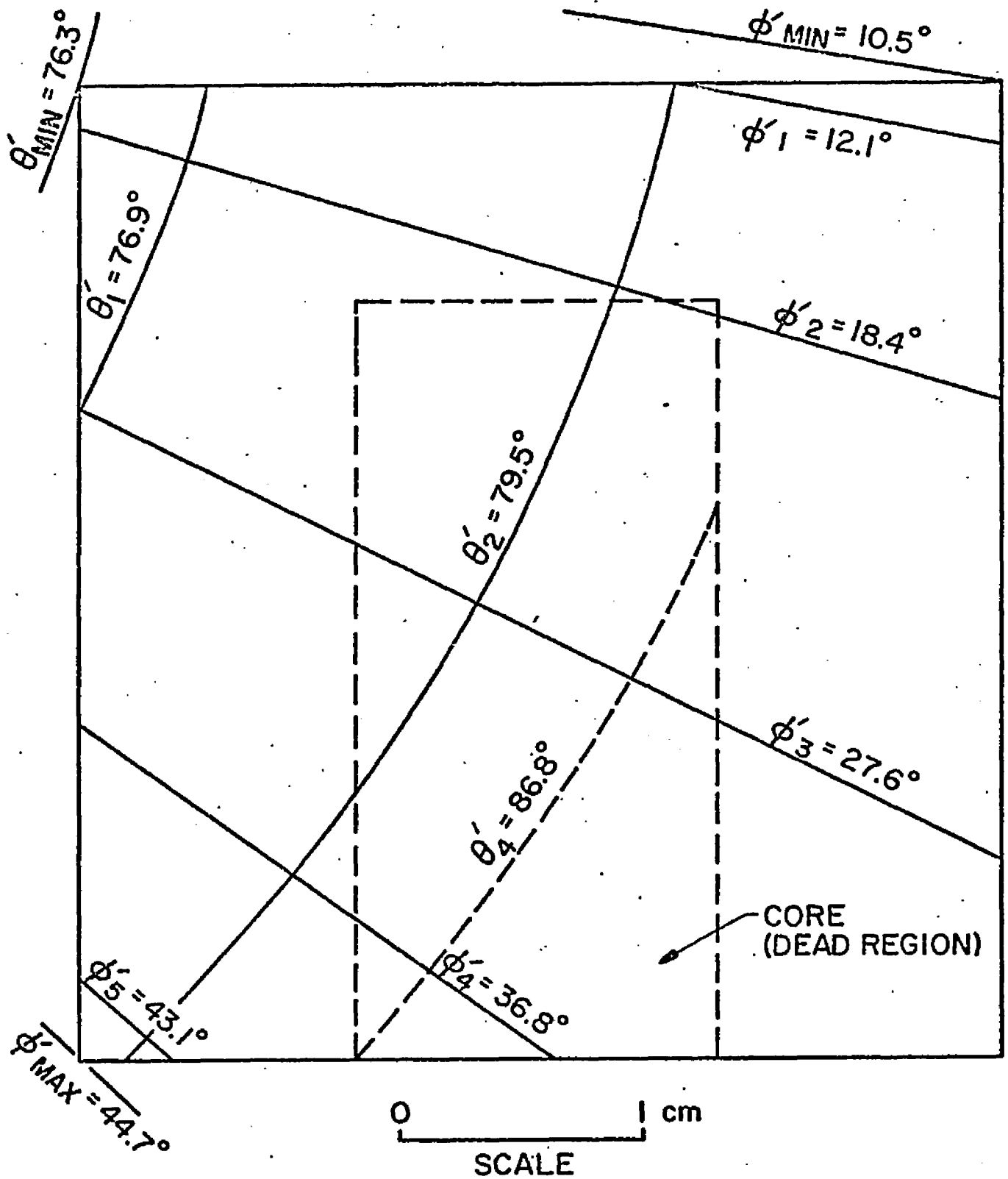


Fig. 22. An enlarged top view of the γ -ray detector crystal.

Some of the integration points, θ'_i and ϕ'_j , as well as ϕ'_{min} , ϕ'_{max} , and θ'_{max} are indicated.

projection of the true distance onto a plane, the true distance is found by dividing the measured distance by $\cos(\theta'_i - (\pi/2))$. Table XIIIa gives the distances measured from Fig. 22, where any distance traversed in the dead region has not been included. Table XIIIb gives the corrected distances which are taken as the values of $\rho(\theta'_i, \varphi'_j)$.

This procedure gives $\langle \hat{r} \rangle_\gamma$ in the limit as the γ -ray energy becomes very high. The low energy limit is found by setting all non-zero $\rho(\theta'_i, \varphi'_j)$ equal to 1. The final value for $\langle \hat{r} \rangle_\gamma$ is chosen to be somewhere between these two limits.

The results for the high energy limit and low energy limit are given in Table XIII. The effective position of the γ -ray detector is $((\pi/2), R_\gamma)$ where $R_\gamma = \arctan \left[\frac{\langle y' \rangle_\gamma}{\langle x' \rangle_\gamma} \right]$. The magnitude of $\langle \hat{r} \rangle_\gamma$ is given by

$$|\langle \hat{r} \rangle_\gamma| = \left\{ \left[\langle x' \rangle_\gamma \right]^2 + \left[\langle y' \rangle_\gamma \right]^2 \right\}^{\frac{1}{2}} \quad (\text{A6})$$

Table XII. Measured and corrected distances traversed by a γ ray in the detector crystal.

		Measured Distance (Relative)					Corrected Distance = $\rho(\theta'_i, \varphi'_j)$ (Relative)				
$\theta'_i \backslash \varphi'_j$		φ'_1 12.1°	φ'_2 18.4°	φ'_3 27.6°	φ'_4 36.8°	φ'_5 43.1°	φ'_1 12.1°	φ'_2 18.4°	φ'_3 27.6°	φ'_4 36.8°	φ'_5 43.1°
θ'_1 76.9°		0.0	2.3	0.0	0.0	0.0	0.0	2.4	0.0	0.0	0.0
θ'_2 79.5°		0.0	19.1	14.6	7.4	2.9	0.0	19.4	14.8	7.5	3.0
θ'_3 83.1°		14.7	39.5	42.0	25.6	6.4	14.8	39.8	42.3	25.8	6.4
θ'_4 86.8°		14.7	39.4	39.2	25.6	6.4	14.7	39.5	39.3	25.7	6.4
θ'_5 89.4°		14.7	37.7	25.1	14.0	6.4	14.7	37.7	25.1	14.0	6.4

(a)

(b)

Table XIII. Results of the numerical integration for the low and high energy limits.

Low Energy Limit	High Energy Limit
$\langle x^2 \rangle_Y = 0.866$	$\langle x^2 \rangle_Y = 0.887$
$\langle y^2 \rangle_Y = 0.456$	$\langle y^2 \rangle_Y = 0.428$
$ \langle \hat{r} \rangle_Y = 0.978$	$ \langle \hat{r} \rangle_Y = 0.985$
$R_Y = 27.8^\circ$	$R_Y = 25.7^\circ$

APPENDIX B

A COMPARISON OF THE FAST-SLOW AND SLOW-FAST COINCIDENCE SYSTEMS

In the process of changing from cross-over-pick-off timing to leading-edge timing we went from a slow-fast to a fast-slow coincidence system. An analysis follows which shows that, while the two systems are different, under most experimental conditions the difference is negligible.

Fig. 23 gives the block diagrams of the two systems showing the counting rates in the various legs. The notation is as follows: The particle counting rate is R_p . The γ -ray counting rate is R_γ . The particle rate through the window is R_w .

In the derivations which follow we will need the following additional notation. The rate of particles through the window which are (are not) in true coincidence with a γ ray is $R^{p\gamma}$ ($R^{p\bar{\gamma}}$). The rate of particles not through the window which are (are not) in true coincidence with a γ ray is $R^{\bar{p}\gamma}$ ($R^{\bar{p}\bar{\gamma}}$). The rate of γ rays not in true coincidence with a particle is $R^{o\gamma}$. With these definitions the following equations result:

$$R_\gamma = R^{p\gamma} + R^{\bar{p}\gamma} + R^{o\gamma} \quad , \quad (B1)$$

$$R_p = R^{p\gamma} + R^{\bar{p}\gamma} + R^{p\bar{\gamma}} + R^{\bar{p}\bar{\gamma}} \quad , \quad (B2)$$

$$R_w = R^{p\gamma} + R^{p\bar{\gamma}} \quad . \quad (B3)$$

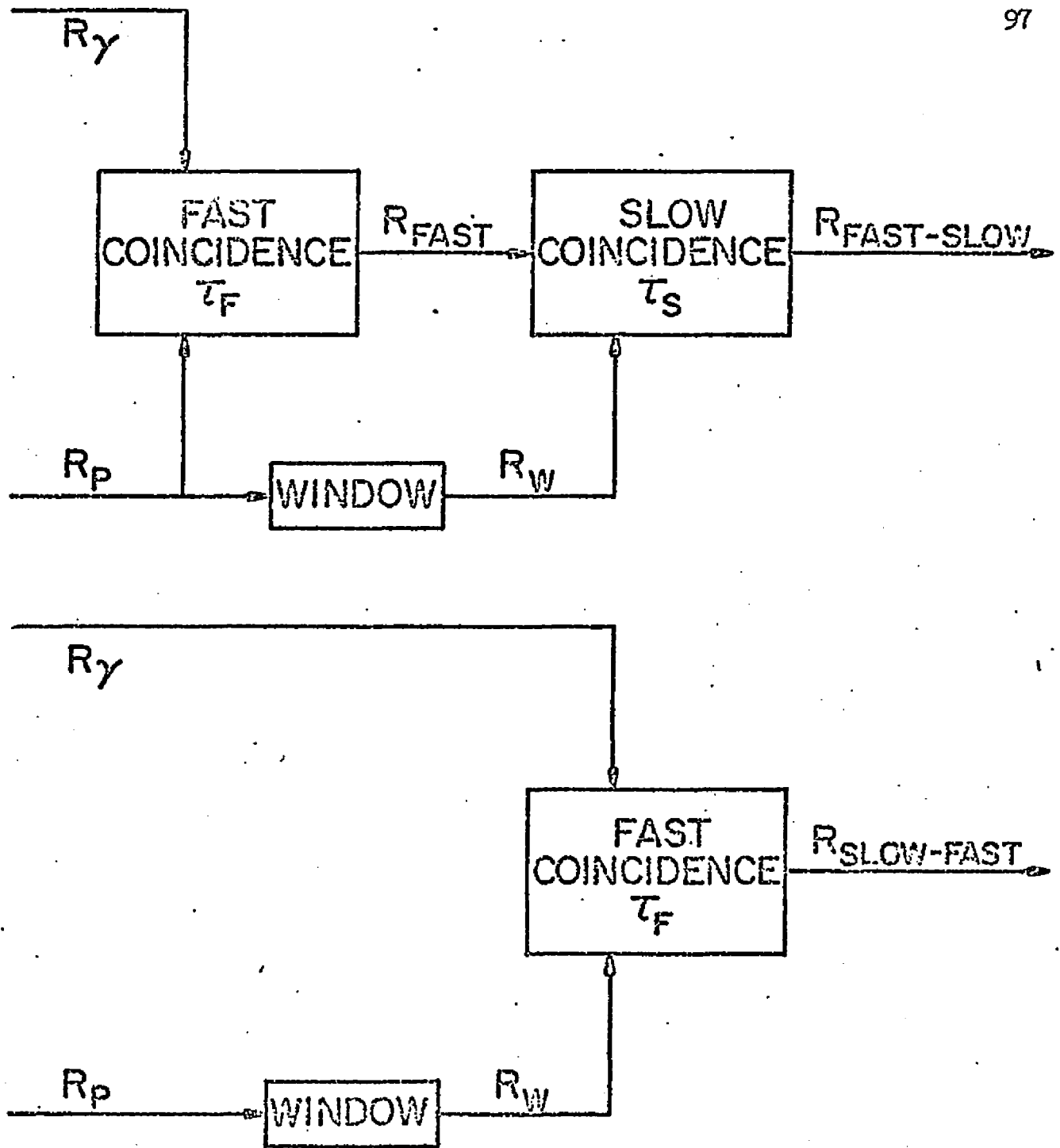


Fig. 23. A block diagram of the fast-slow and slow-fast coincidence systems.

τ is the time resolution of the coincidence circuit.

Taking the chance rate to be two times τ , the resolving time of the coincidence circuit, times the product of the two rates in coincidence, we obtain

$$R_{\text{fast}} = R^{\text{PY}} + R^{\bar{\text{PY}}} + 2\tau_{\text{F}} R^{\text{OY}} [R^{\text{PO}} + R^{\bar{\text{PO}}}] , \quad (\text{B4})$$

$$R_{\text{fast-slow}} = R^{\text{PY}} + 2\tau_{\text{F}} R^{\text{OY}} R^{\text{PO}} + 2\tau_{\text{S}} R^{\text{PO}} [R^{\bar{\text{PY}}} + 2\tau_{\text{F}} R^{\text{OY}} R^{\bar{\text{PO}}}] , \quad (\text{B5})$$

and

$$R_{\text{slow-fast}} = R^{\text{PY}} + 2\tau_{\text{F}} R^{\text{PO}} [R^{\bar{\text{PY}}} + R^{\text{OY}}] . \quad (\text{B6})$$

The difference in rates between $R_{\text{fast-slow}}$ and $R_{\text{slow-fast}}$ is then

$$\Delta R = 2 R^{\text{PO}} R^{\bar{\text{PY}}} [\tau_{\text{S}} - \tau_{\text{F}}] + 4\tau_{\text{S}} \tau_{\text{F}} R^{\text{PO}} R^{\bar{\text{PO}}} R^{\text{OY}} . \quad (\text{B7})$$

Under typical conditions $R^{\text{Y}} \approx 200$ cts/sec, $R^{\bar{\text{PY}}} \approx \text{TAC rate} \approx 100$ cts/sec, $\tau_{\text{S}} \approx 5 \times 10^{-7}$ sec, $\tau_{\text{F}} \approx 5 \times 10^{-8}$ sec, $R^{\bar{\text{PO}}} \approx 15,000$ cts/sec, and $R^{\text{OY}} \approx 10,000$ cts/sec. Using these values in Eq. (B7) gives $\Delta R \approx 2 \times 10^{-2}$ cts/sec.

However, this calculation is experimentally unrealistic because it has not taken into account the finite dead time of the window. This finite dead time results from the fact that if a count from $R^{\bar{\text{PY}}}$ or $R^{\bar{\text{PO}}}$ reaches the window before a count from R^{PO} , the window is occupied, rejecting the count from $R^{\bar{\text{PY}}}$ or $R^{\bar{\text{PO}}}$, and ignores the count from R^{PO} . Thus the rate ΔR of Eq. (B7) must be reduced by at least a factor of two.

Taking $\Delta R \approx 10^{-2}$ cts/sec means that for a 4096 channel ADC approximately 10^{-2} cts/channel per hour, on the average, will be stored.

At this rate it would take approximately 100 hours to get an average of one additional count in each channel due to the use of a fast-slow over a slow-fast coincidence method.

APPENDIX C

A DESCRIPTION OF THE "AND", "OR" AND "ROUTING-TO-MEMORY" BOXES

The circuits to be discussed use almost entirely electronic logic circuits. Therefore logic diagrams will be used frequently to amplify the discussion. Fig. 24 gives the basic logic and logical symbols to be used in the following discussion.

The Routing-to-Memory Box

The routing-to-memory box performs three separate functions of digital gain conversion of the ADC output address, routing of this address to various block address selectors, and selection of blocks of addresses to be stored in the memory. These basic functions are shown in block form in Fig. 25.

The digital gain conversion section takes the twelve binary bits from the ADC and gives out the $12-k$ most significant bits, where $k = 0$ to 4 is the position of the digital gain conversion switch. This serves to reduce the 4096 maximum input address to $4096/2^k$ by, in effect, adding every set of 2^k channels together.

The block address selector looks at any one of $16/2^k$ consecutive blocks of 256 addresses to see if the address from the digital gain conversion selector falls within that block. If it does and if the routing conditions have been met by the external routing signals, a count is added to a channel in the quarter of the memory which is governed by

Fig. 24. Basic logic and logical symbols.

Left side: three logical operations, a combination of these operations known as de Morgan's theorem, and the corresponding truth tables are shown.

Right side: two logical symbols which represent two of the basic logical operations together with four combinations of these symbols and the operations these combinations represent are shown.

A signal is "true" or "yes" when in the higher voltage state, and "false" or "no" when in the lower voltage state.

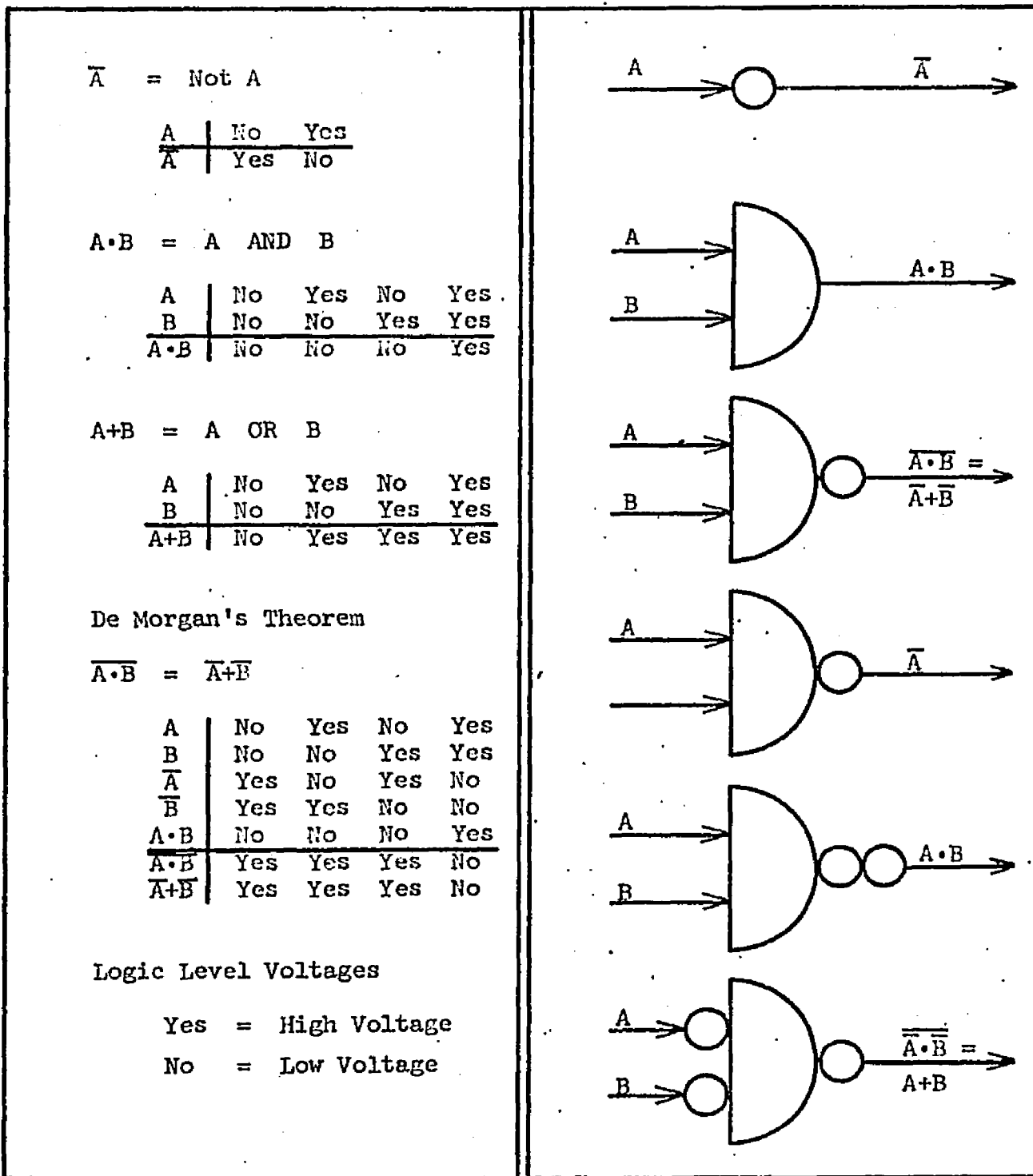


Fig. 24. Basic logic and logical symbols.

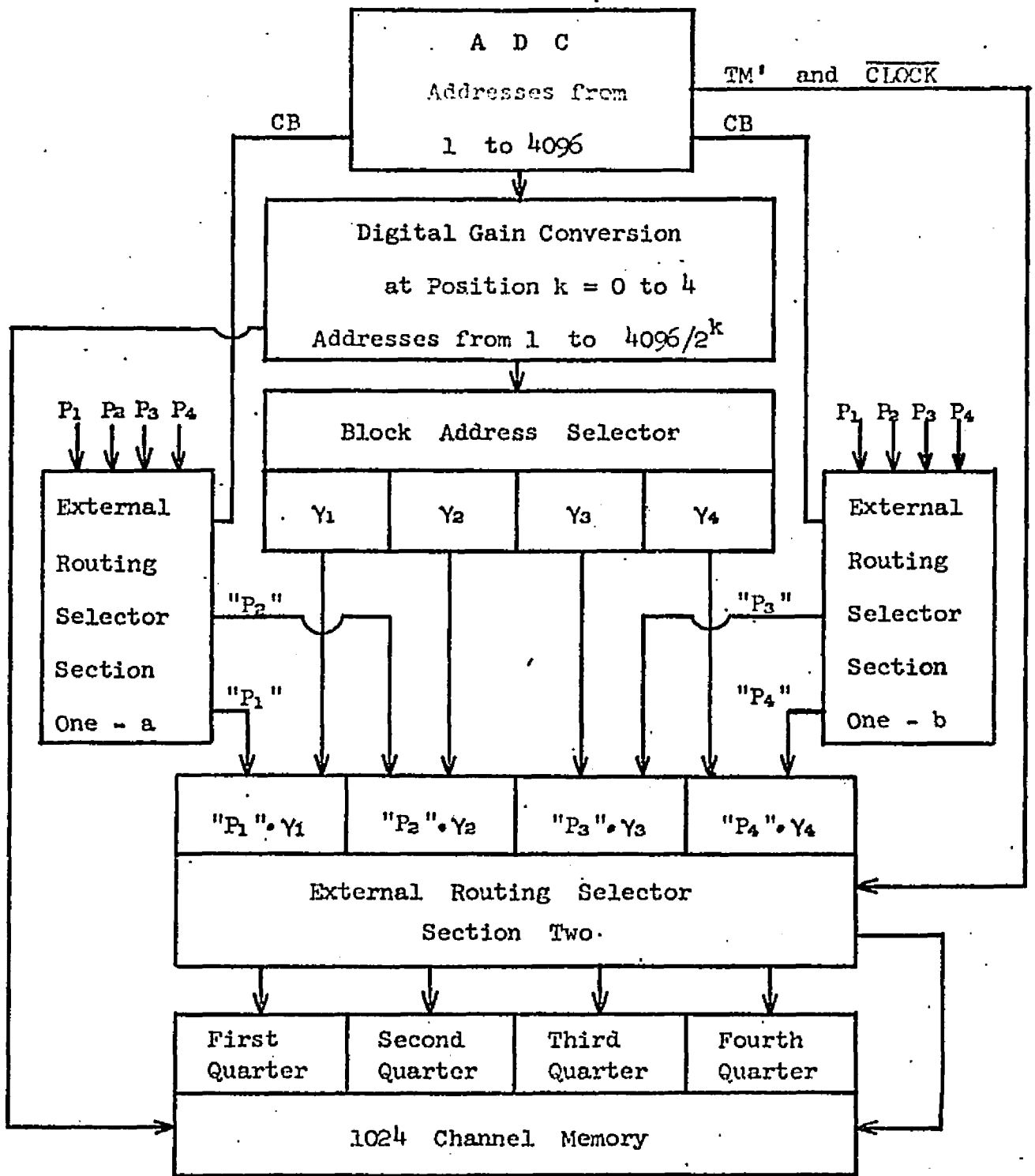


Fig. 25. Functional block diagram of routing-to-memory box.

that block address selector. The address of the channel in the 256-channel quarter of the memory is the same as the relative address in the block of 256 addresses seen by the block address selector.

The external routing selector permits a count to be stored in the i^{th} quarter of the memory if an address appears in the proper block of the i^{th} block address selector and a routing pulse has appeared at the proper routing input. For the first position of the external routing selector switches, this routing pulse must appear at the i^{th} input. Other positions permit a count to be stored if routing pulses appear at the first or second inputs, or at the third or fourth inputs.

To facilitate the reading of the diagrams which are to follow, Fig. 26 gives a block diagram of the routing-to-memory box with each signal indicated where it appears in the circuit. Reference to this figure while looking at each individual circuit will help keep in mind what that particular circuit does. The signals, as they leave or enter the box or the circuit board, and their logical yes and no voltages, are given in Table XIV.

The digital gain conversion selector consists of a 12-gang, 5-position switch. The logical wiring of the switch is shown in Fig. 27. The outputs are the wipers of the switch. The signal in the i^{th} column of the j^{th} row is the signal which appears at the j^{th} wiper when the switch is in the i^{th} gain conversion position.

The block address selector consists of four logic-level converters and inverters, four 4-gang, 16-position switches, and four 4-input AND circuits. The i^{th} block address selector is shown in Fig. 28. The

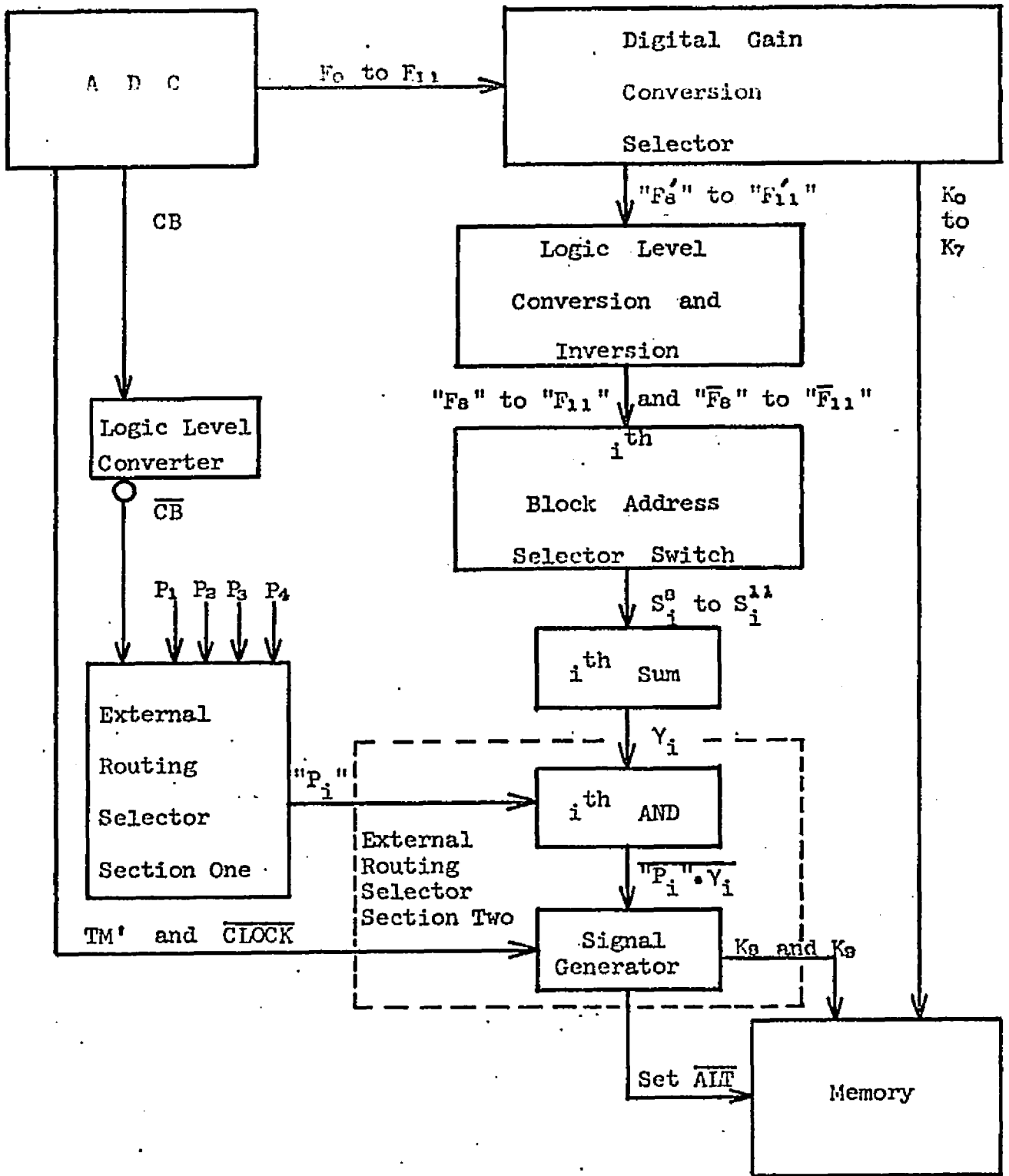


Fig. 26. Signal block diagram of routing-to-memory box.

Table XIV. Signals with their routing and logical voltage levels.

Signal	From	To	YES Voltage	NO Voltage
F_k	ADC ^a	DGCS ^b	+ 8	- 4
K_1 to 7	DGCS	Memory	+ 8	- 4
" F_k "	DGCS	board ^c	+ 8	- 4
" F_k "	board	BASS ^d	0	- 4
" F_k "	board	BASS	0	- 4
S_{ij}	BASS	board	0	- 4
$\overline{P_i}$	BNC ^e	board	0	- 4
P_i and $P_i + P_j$	board	ERSS ^f	0	- 4
" P_i "	ERSS	board	0	- 4
K_8 and 9	board	Memory	+ 8	- 4
$\overline{\text{Clock}}$	ADC	board	+ 8	- 4
TM'	ADC	board	+ 8	- 4
CB	ADC	board	+ 8	- 4
Set \overline{ALT}	board	ADC	+ 8	- 4

^aAnalog-to-Digital Converter

^bDigital Gain Conversion Switch on front panel

^cCircuit board

^dBlock Address Selector Switch on front panel

^eBNC connector on front panel

^fExternal Routing Selector Switch on front panel

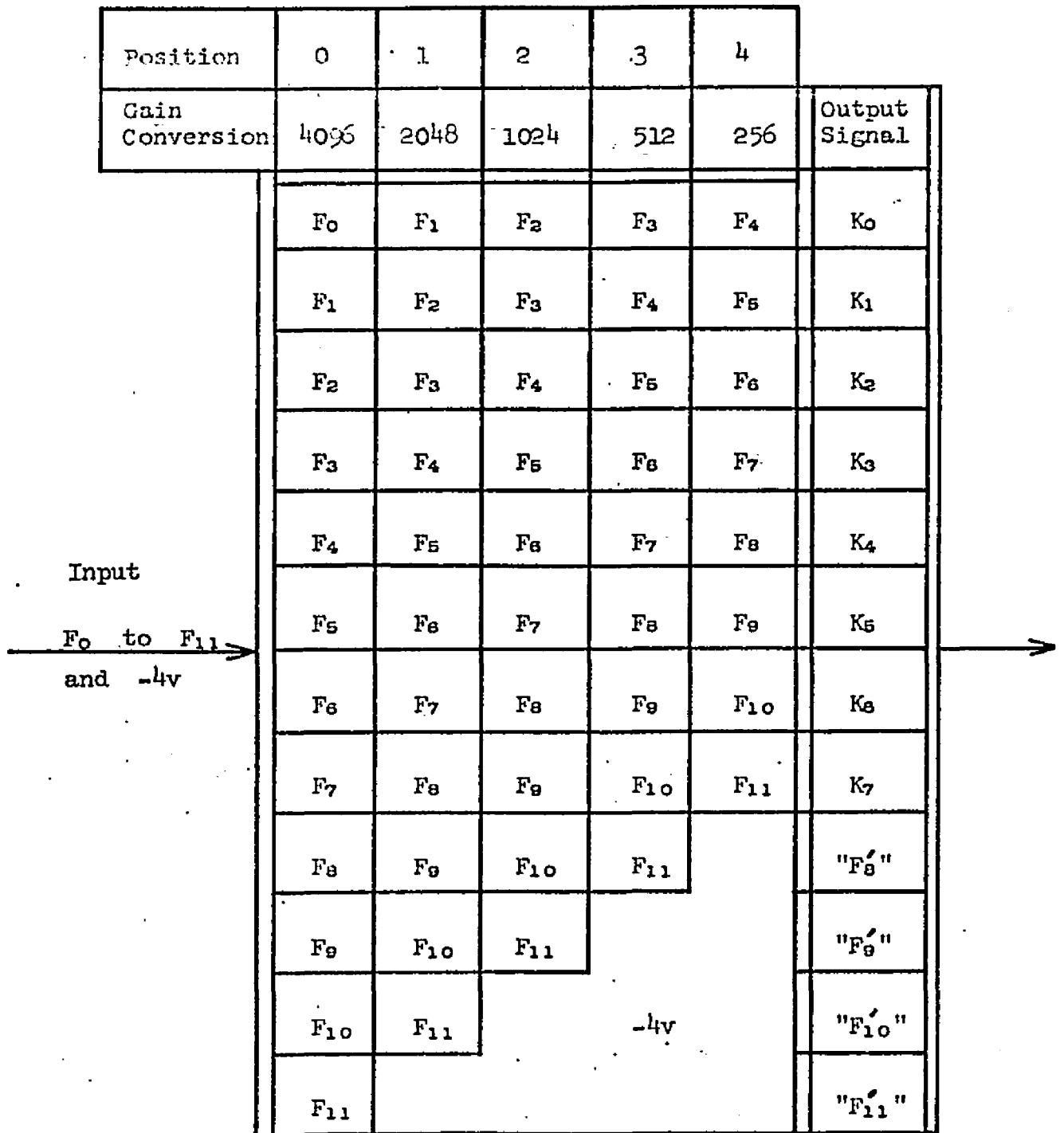


Fig. 27. Logic diagram of digital gain conversion selector.

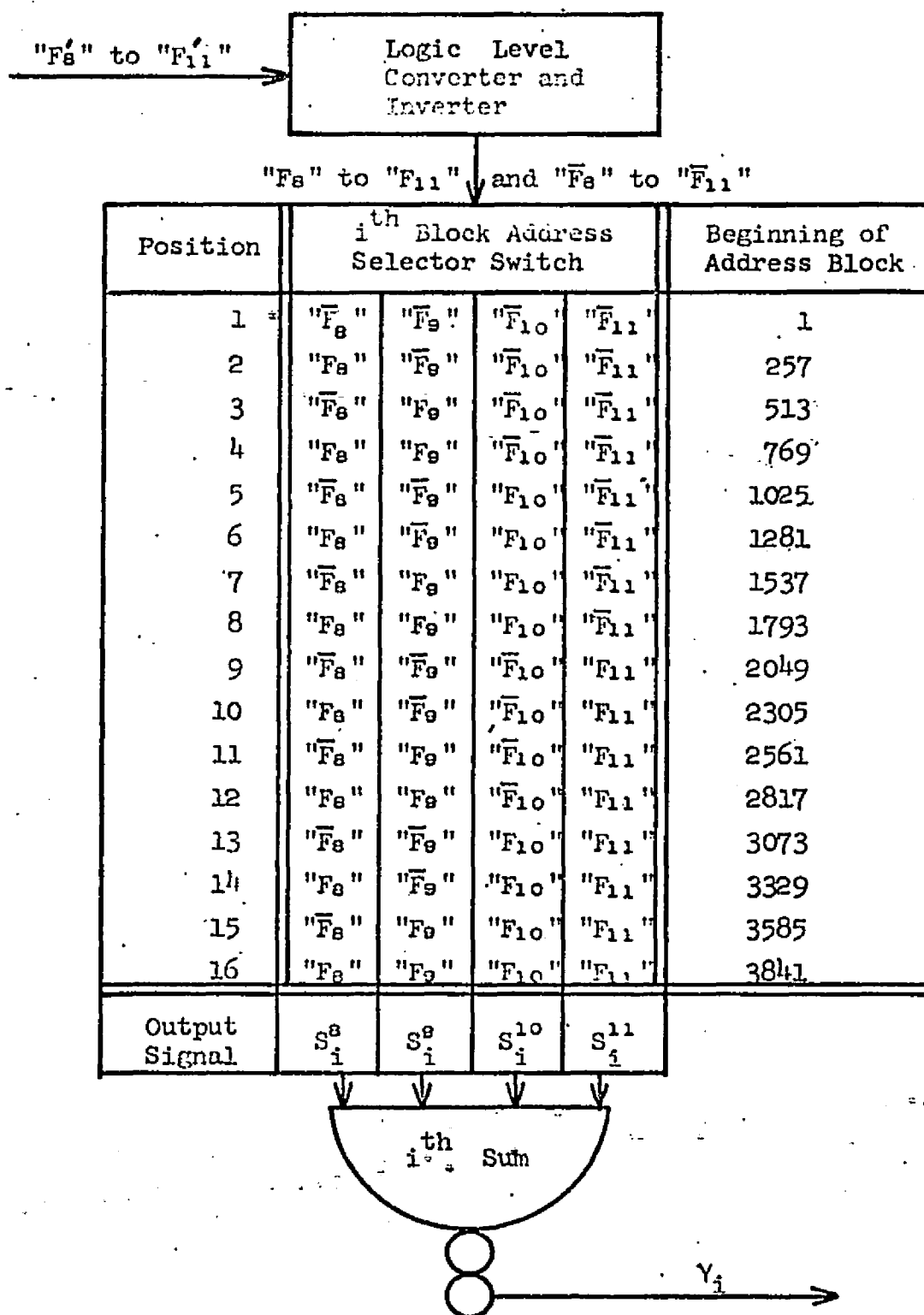


Fig. 28. Logic diagram of block address selector.

positions of each selector switch are meaningful up through $16/2^k$, where $k = 0$ to 4 in the position of the digital gain selector switch.

The first section of the external routing circuit is shown in Fig. 29. This circuit takes the pulses, \overline{P}_i , from the front BNC connectors if the analyzer is not busy, converts them from pulses to d.c. levels, and makes sure only one P_i is set to a logical one position.

The R-S flip-flop is an unambiguous type, i.e., both inputs high leave R_{out} high and S_{out} low. However, if two inputs do not overlap completely the flip-flop will set to the position which was high last. Since it remains set after the pulse is gone, this flip-flop is the element which converts the input pulses to d.c. levels.

The signals, $P_1, P_2, P_3, P_4, P_1 + P_2, P_3 + P_4$, are sent to the external routing selector switch on the front panel. These two switches are of the 2-gang, 5-position type. The switching diagram gives what is connected to the wiper output, " P_i ", in any given switch position. The " P_i " are sent back to the circuit board and are used in the second section of the external routing circuit.

The second section of the external routing circuit, shown in Fig. 30, decides whether or not a count should be added to the memory. If so, it tells the memory to store the count and in which quarter of the memory it should be stored. The memory is told to store a pulse unless Set \overline{ALT} is true. Set \overline{ALT} is true when

$$\overline{((\overline{P_1} \cdot \gamma_1) + (\overline{P_2} \cdot \gamma_2) + (\overline{P_3} \cdot \gamma_3) + (\overline{P_4} \cdot \gamma_4)) \cdot (\overline{CLOCK}) \cdot (TM')}$$

is true.

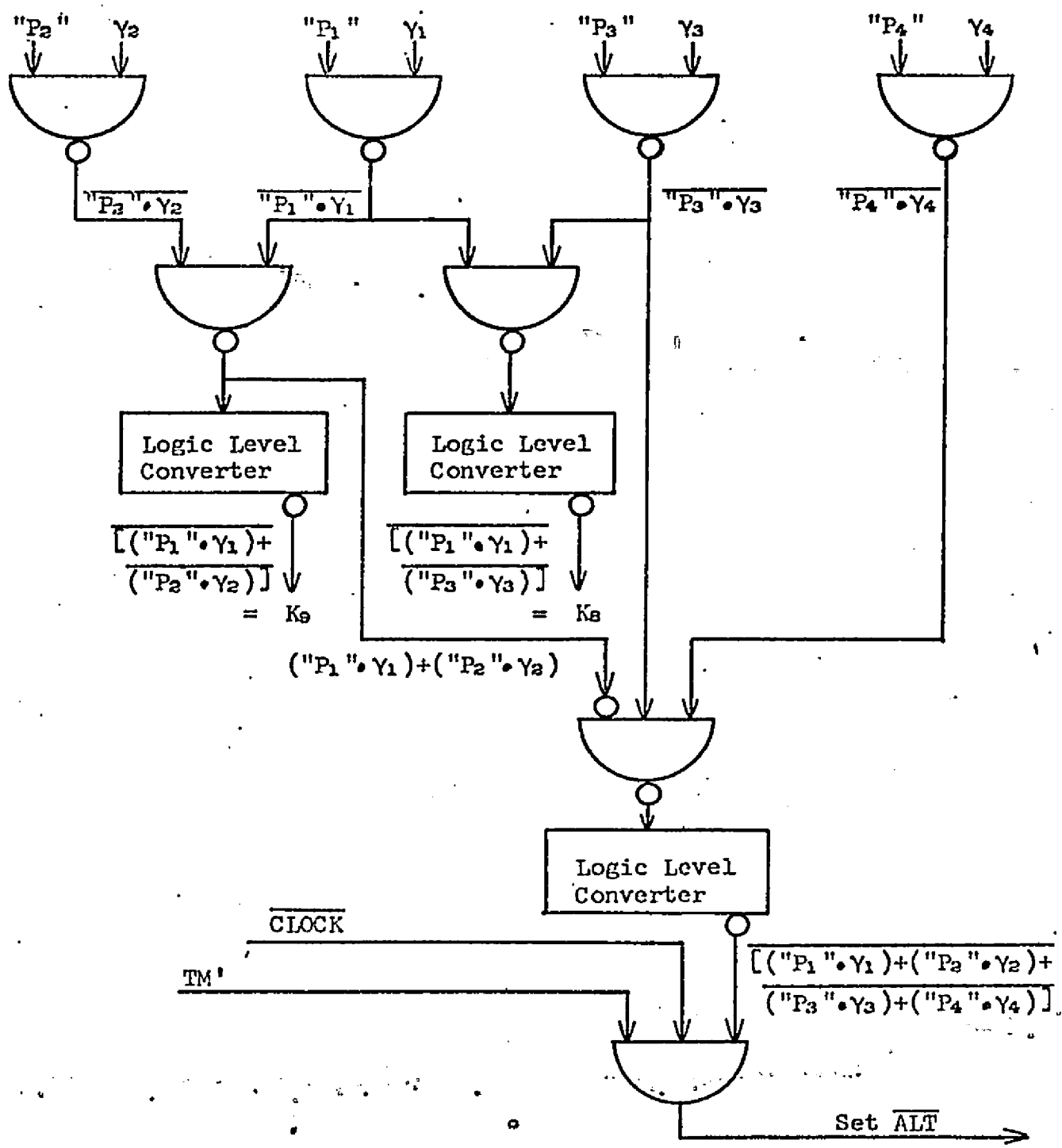


Fig. 30. Logic diagram of external routing selector section II.

The "AND" and "OR" Boxes

Fig. 31 shows the logic diagrams of the four 2-input AND circuit and the 5-input OR circuit. Note that the inputs to the AND circuits must be d.c. coupled. If they are not, they will float at a logical high level. An a.c. coupled input may be used by terminating it in 50 ohms. This makes the input stay at a logical low level. The d.c. outputs of the AND circuits are compatible with the input requirements of the OR circuit. The a.c. outputs of the AND circuits are compatible with the inputs of the routing-to-memory box. The pulser input on the OR circuit must be terminated in 50 ohms when it is not used.

Fig. 32 shows the schematics of the Motorola MDTL integrated circuits and logic level converters. The circuits use two types of integrated circuits, the 830P, a two 4-input nand gate, and the 846P, a four 2-input nand gate. The logic level converter from +8V, -4V to 0V, -4V is identical to the logic level converter from 0V, -4V to +8V, -4V with the exception that the collector voltage of the former is 0V, while the collector voltage of the latter is +8V. Note that these logic level converters also invert. Note also that the nature of the integrated circuits makes them high impedance devices in the logical one state, and low impedance devices in the logical zero state. Therefore, if an output in the logical one state must drive a low impedance device such as the logic level converter, then the output must be connected by a resistor of approximately 500 Ω to the logical one voltage. This has the effect of lowering the impedance of this output in the logical one state to the impedance of the resistor.

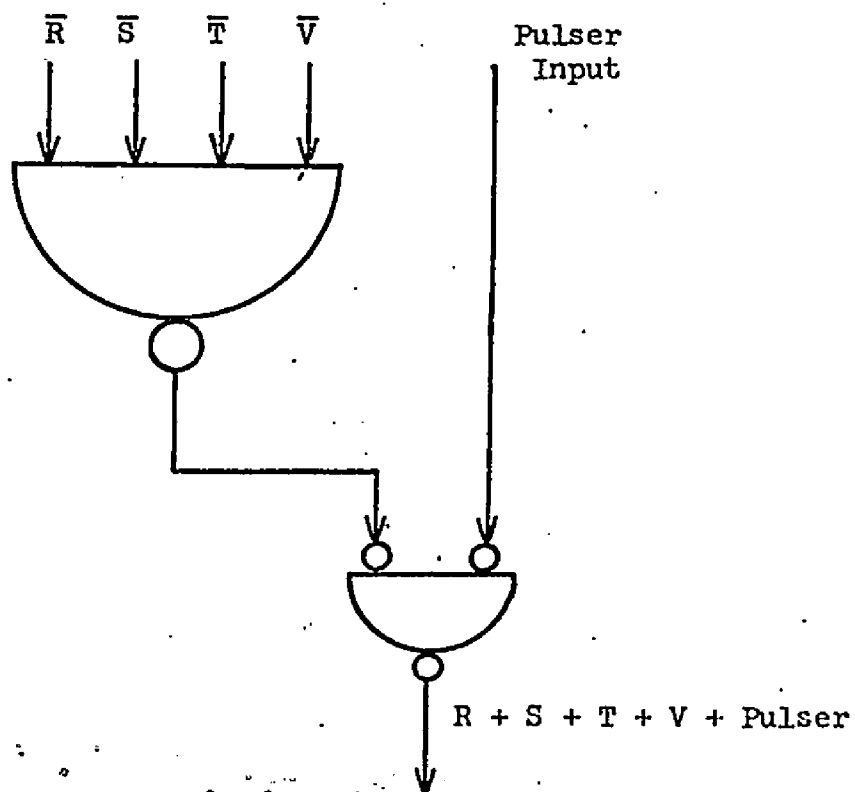
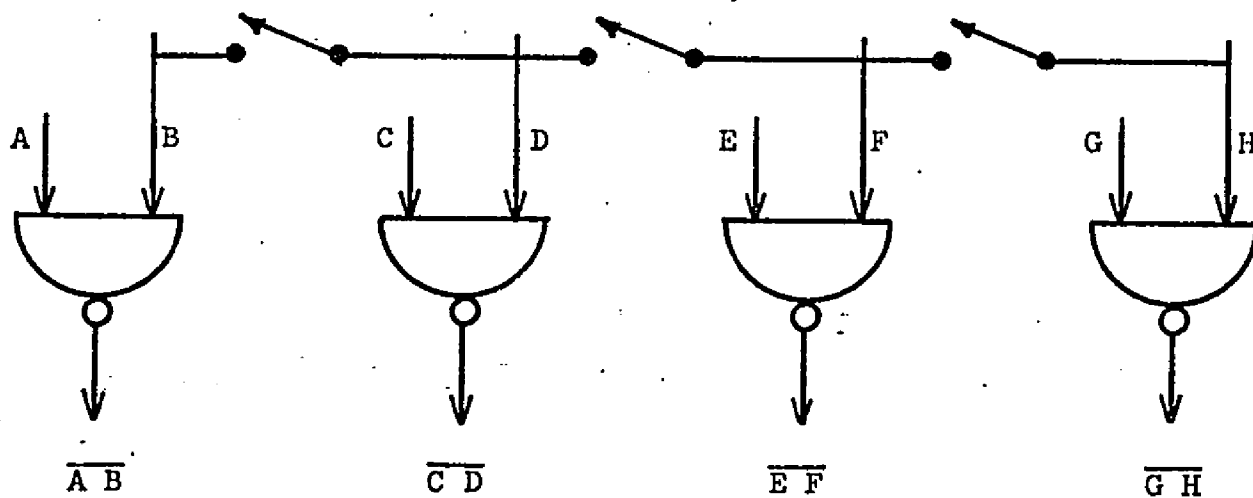


Fig. 31. Logic diagrams of the four 2-input AND circuits and the 5-input OR circuit.

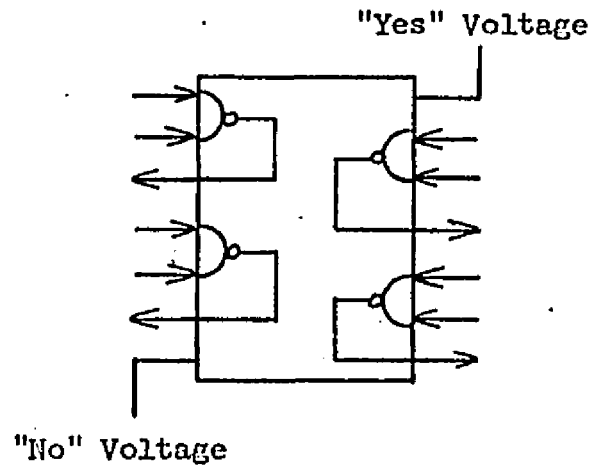
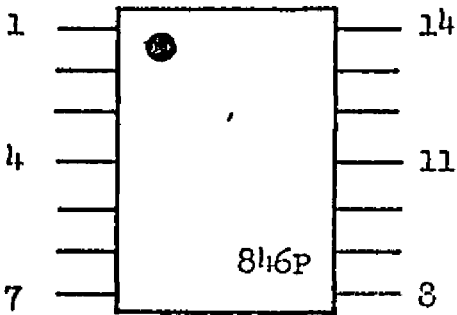
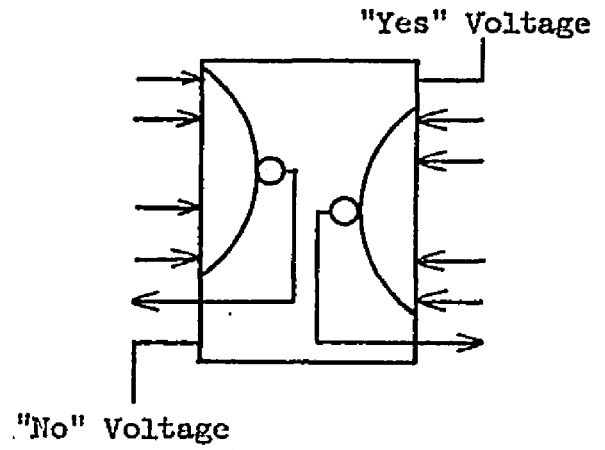
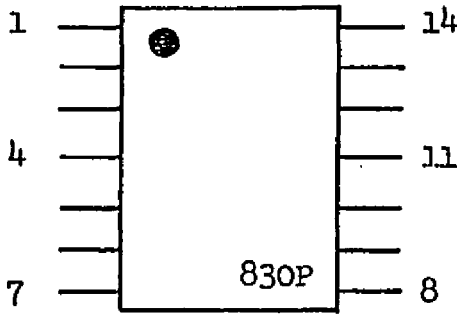
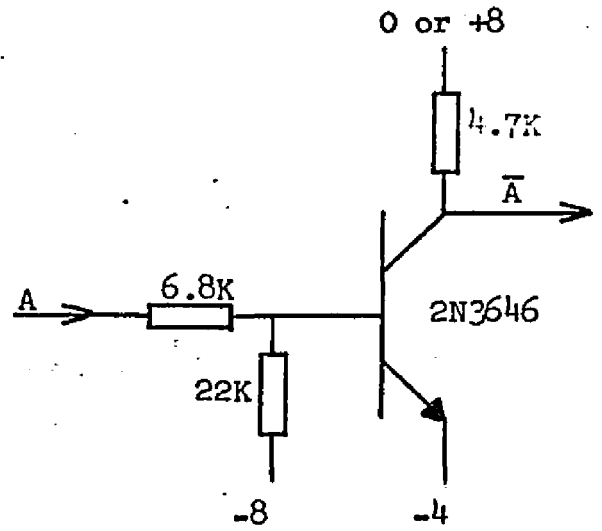
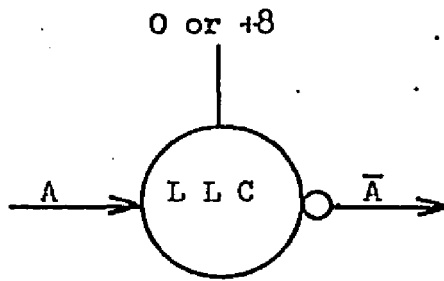
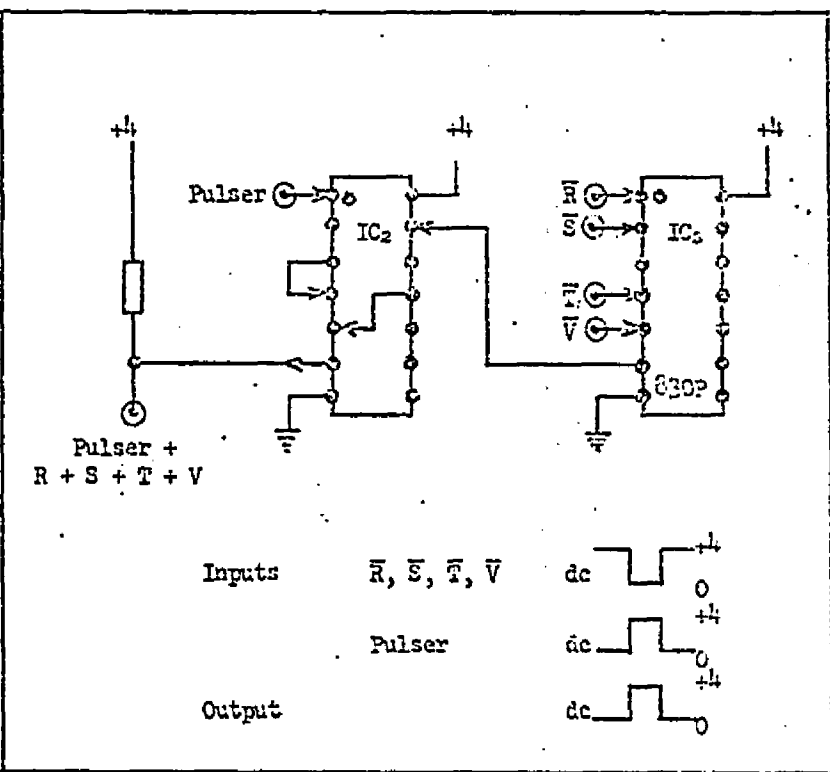
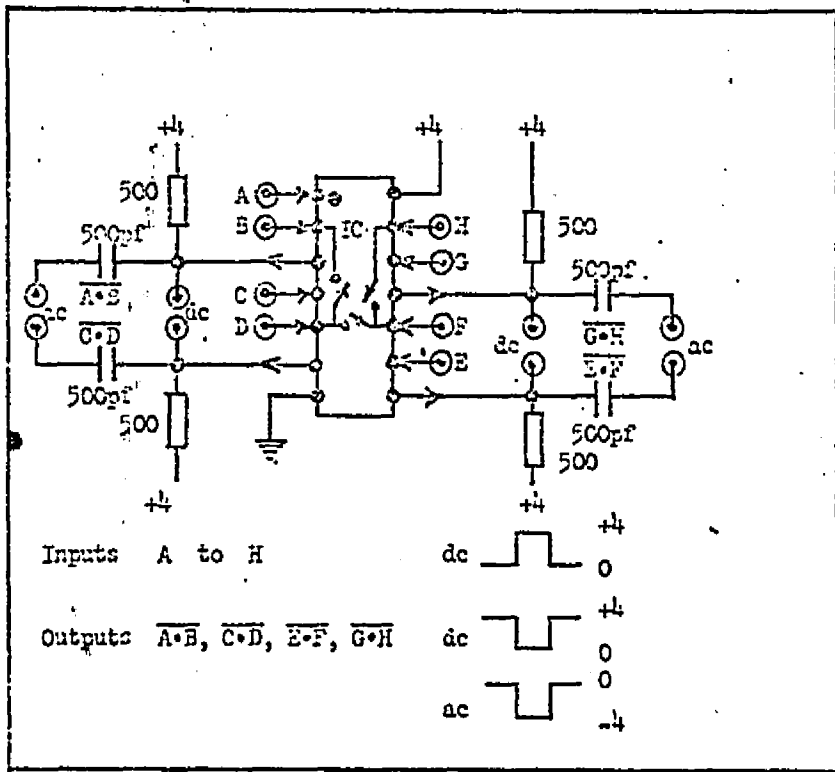


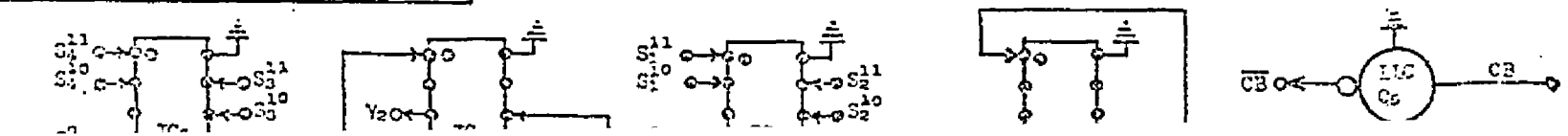
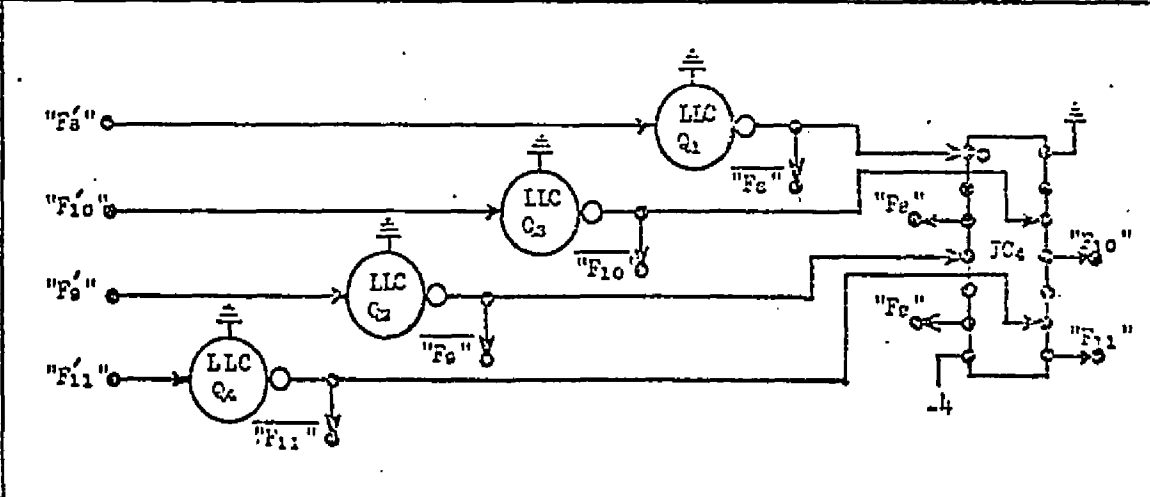
Fig. 32. Schematic diagrams of a logic-level converter and two integrated circuits.

The schematic diagrams of all three circuits are given in Fig. 33. Fig. 34 shows the position of all integrated circuits and transistors as seen from the top of the circuit boards.



Transistors are 2N3546.
 Integrated Circuits are 846P unless otherwise marked.
 Diodes are any good silicon type.

- Signal goes off the board.
- ⊙→ Signal comes onto the board.
- Signal goes to somewhere else on the board.
- ⊙→ Signal comes from somewhere else on the board.
- ⊙— DDC connector on front panel.



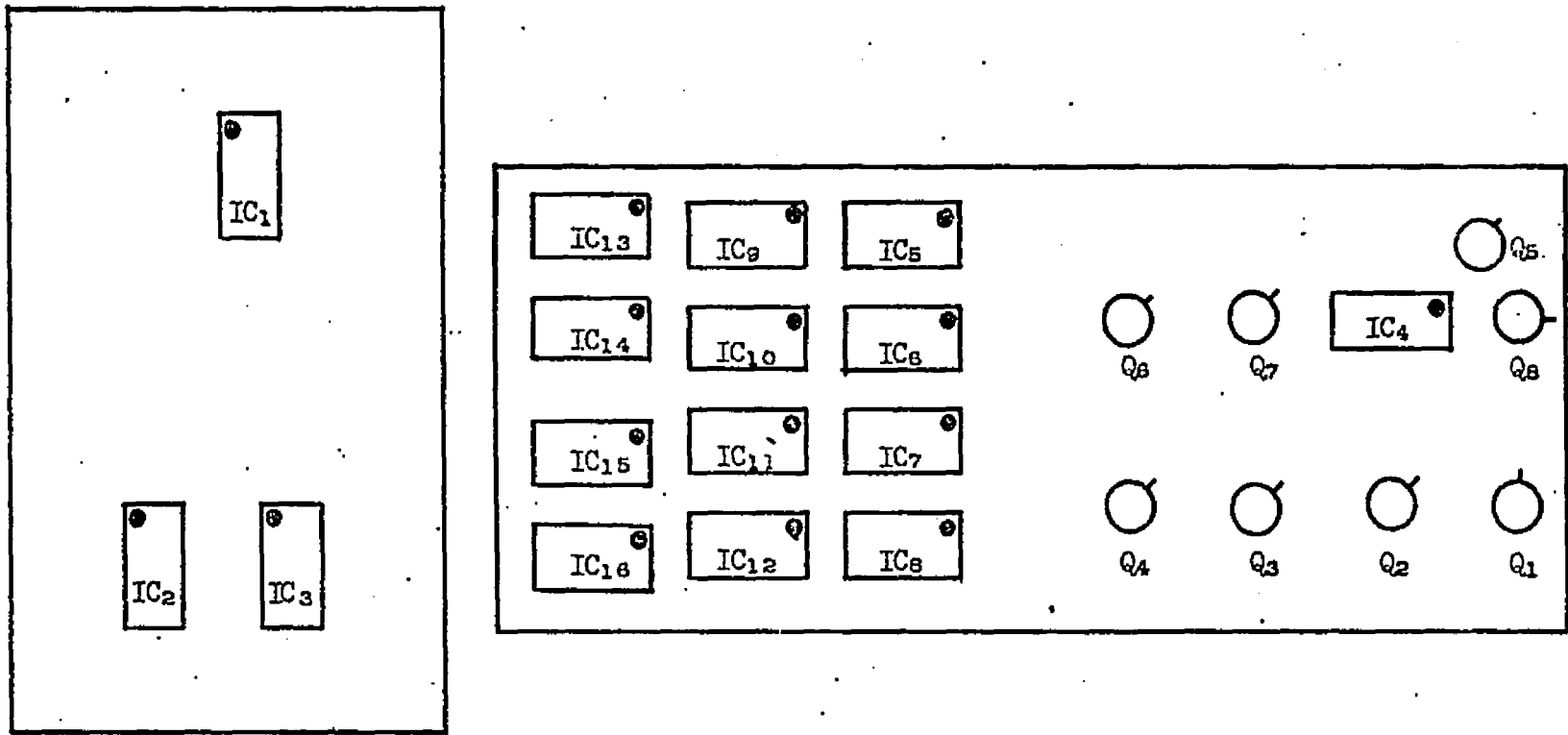


Fig. 34. Top view of circuit boards for the AND, OR, and routing-to-memory boxes.

APPENDIX D

THE MEAN LIFE CALCULATION FOR A LEVEL WHICH IS POPULATED BY TRANSITIONS FROM ABOVE

In the process of measuring mean lives by the Doppler-shift attenuation coincidence method, the situation often arises that a level, upon which a measurement is being made, is fed wholly or in part by an upper level. When the upper level has a very short mean life this situation presents no problem. But when the mean life comes within a factor of ten of the mean life of the level that is being measured, a correction must be made in the measured attenuation factor, F_{meas} .

Let us first assume that level 1, with an original population of N_0 , decays entirely to level 2. Further, let us assume that this is the only method of populating level 2. Since the decay rate from a given level is proportional to the instantaneous population of the level over its mean life, we can write

$$\left(\frac{d N_1(t)}{dt}\right)_{1 \rightarrow 2} = -\frac{N_1(t)}{\tau_1}, \quad (D1)$$

and

$$\left(\frac{d N_2(t)}{dt}\right)_{2 \rightarrow 3} = -\frac{N_2(t)}{\tau_2}. \quad (D2)$$

Since Eq. (D1) represents the only change in the population of level 1, it can be integrated to give

$$N_1(t) = N_0 e^{-t/\tau_1} \quad (D3)$$

Thus

$$\left(\frac{d N_1(t)}{dt}\right)_{1 \rightarrow 2} = -\frac{N_0}{\tau_1} e^{-t/\tau_1} \quad (D4)$$

Therefore the rate of change in the population of level 2 is

$$\frac{d N_2(t)}{dt} = \left(\frac{d N_2(t)}{dt}\right)_{1 \rightarrow 2} + \left(\frac{d N_2(t)}{dt}\right)_{2 \rightarrow 3} \quad (D5)$$

where

$$\left(\frac{d N_2(t)}{dt}\right)_{1 \rightarrow 2} = -\left(\frac{d N_1(t)}{dt}\right)_{1 \rightarrow 2} \quad (D6)$$

Using Eqs. (D6) and (D2) in Eq. (D5) gives

$$\frac{d N_2(t)}{dt} + \frac{1}{\tau_2} N_2(t) = \frac{N_0}{\tau_1} e^{-t/\tau_1} \quad (D7)$$

Eq. (D7) is of the form

$$\frac{dy}{dt} + P(t) Y = Q(t) \quad (D8)$$

which has a solution of the form

$$Y = e^{-\int P dt} \left\{ \int e^{-\int P dt} Q(t) dt + C \right\} \quad (D9)$$

Noting that $N_2(t) = 0$ at $t = 0$, the solution of Eq. (D7) is

$$N_2(t) = \frac{\tau_2 N_0}{\tau_1 - \tau_2} \left[e^{-t/\tau_1} - e^{-t/\tau_2} \right]. \quad (D10)$$

Thus from Eq. (D2) we have

$$\left(\frac{dN_2(t)}{dt} \right)_{2-3} = - \frac{N_0}{\tau_1 - \tau_2} \left[e^{-t/\tau_1} - e^{-t/\tau_2} \right]. \quad (D11)$$

The definition of the attenuation factor from Eqs. (3) and (10) in Chapter II is

$$F = \frac{1}{N_0} \int_0^{\infty} dt \left(- \frac{dN}{dt} \right) \frac{v(t) \cos \varphi}{v_0} \quad (D12)$$

Substitution of Eq. (D11) into (D12) gives

$$F_{2-3} = \frac{1}{\tau_2 - \tau_1} \left\{ \tau_2 F(\tau_2) - \tau_1 F(\tau_1) \right\}. \quad (D13)$$

In practice, τ_1 and $F(\tau_1)$ are known, F_{2-3} is measured, and τ_2 is found graphically from

$$\tau_2 = \tau_1 \left[\frac{F_{2-3} - F(\tau_1)}{F_{2-3} - F(\tau_2)} \right]. \quad (D14)$$

In the case where level 2 is fed directly by a fraction P_D as well as a fraction P_C by a cascade, the measured energy shift is given by

$$\Delta E_{\text{meas}} = P_D \Delta E_D + P_C \Delta E_C, \quad (\text{D15})$$

where $P_D + P_C = 1$. The shifts ΔE_D and ΔE_C are given by

$$\frac{\Delta E}{\Delta E_{\text{full}}} = F. \quad (\text{D16})$$

Thus

$$\Delta E_{\text{meas}} = P_D F_D \Delta E_{D_{\text{full}}} + P_C F_C \Delta E_{C_{\text{full}}}, \quad (\text{D17})$$

where $F_C = F_{2 \rightarrow 3}$ given by Eq. (D13). Substitution of Eq. (D13) into (D17) with some rearrangement gives

$$\tau_2 = \tau_1 \cdot \left\{ \frac{\Delta E_{\text{meas}} - P_D F_D(\tau_2) \Delta E_{D_{\text{full}}} - P_C F_C(\tau_1) \Delta E_{C_{\text{full}}}}{\Delta E_{\text{meas}} - P_D F_D(\tau_2) \Delta E_{D_{\text{full}}} - P_C F_C(\tau_2) \Delta E_{C_{\text{full}}}} \right\}. \quad (\text{D18})$$

Note that when $P_D = 0$ Eq. (D18) reduces to Eq. (D14), as it should.

LIST OF REFERENCES

1. Wozniak, M. J., Jr., Dissertation, The University of Arizona, 1969.
2. Ramavataram, K., Phys. Rev. 132, 2255 (1963).
3. Maxwell, J. R. and W. C. Parkinson, Phys. Rev. 135, B82 (1964).
4. Ohnuma, H., Nucl. Phys. 88, 273 (1966).
5. Vervier, J., Nucl. Phys. 78, 497 (1966).
6. Larner, D., Phys. Rev. (to be published).
7. Thankappan, V. K. and W. W. True, Phys. Rev. 137, B793 (1965).
8. Lindhard, J., M. Scharff, and H. E. Schiott, Kgl. Danske Videnskab. Selskab, Mat. Fys. Medd. 33, No. 14 (1963).
9. Blaugrund, A. E., Nucl. Phys. 88, 501 (1966).
10. Blaugrund, A. E., D. H. Youngblood, G. C. Morrison, and R. E. Segel, Phys. Rev. 158, 893 (1967).
11. Marion, Jerry B., University of Maryland Department of Physics and Astronomy, Technical Report 656 (unpublished).
12. Endt, P. M. and C. van der Leun, Nucl. Phys. A105, 1 (1967).
13. Nuclear Data Sheets, Sheet NRC 60-5-24, Printing and Publishing Office of the National Academy of Sciences, National Research Council.
14. Hardell, R., and A. Hasselgren, Nucl. Phys. A123, 215 (1969).
15. Chagnon, P. R., Nucl. Phys. 59, 257 (1964).
16. Bergqvist, I., J. A. Biggerstaff, J. H. Gibbons, and W. M. Good, Phys. Rev. 158, 1049 (1967).
17. Bissinger, G. A., R. M. Mueller, P. A. Quin, and P. R. Chagnon, Nucl. Phys. A90, 1 (1967).
18. Holtebekk, T., R. Strømme, and S. Tryti, Nucl. Phys. A142, 251 (1970).

19. Preston, M. A., Physics of the Nucleus, Addison-Wesley Publ. Co., (Reading, Mass., 1962).
20. Wilkinson, D. H., Nuclear Spectroscopy, ed. F. Ajzenberg-Selove, Academic Press, Inc., (New York, 1960).
21. Rout, V. M., W. M. Jones, and D. G. Waters, Nucl. Phys. 45, 369 (1963).
22. de López, M. E. O., J. Rickards, and M. Mazar, Nucl. Phys. 51, 321 (1964).
23. El-Behay, A. Z., M. A. Farouk, V. J. Gontchar, V. A. Loutsik, M. H. Nassef, and I. I. Zaloubovsky, Nucl. Phys. 56, 224 (1964).
24. Kurath, Dieter, Phys. Rev. 132, 1146 (1963).
25. Gunye, M. R., and Chindhu S. Warke, Phys. Rev. 156, 1087 (1967).
26. Halbert, E. C., J. B. McGrory, and B. H. Wildenthal, Phys. Rev. Letters 20, 1112 (1968).
27. Quin, Paul, University of Notre Dame, Notre Dame, Indiana, private communication.
28. Quin, Paul, and P. R. Chagnon, University of Notre Dame, Notre Dame, Indiana, private communication.
29. Fulmer, R. H., and A. L. McCarthy, Phys. Rev. 131, 2133 (1963).
30. Sperduto A., and W. W. Buechner, Phys. Rev. 134, B142 (1964).
31. Uchida, Akira, Kanetada Nagamine, Minoru Imaizumi, Hiromichi Kamitsubo, and Shinsaku Kobayashi, J. Phys. Soc. (Japan) 21, 2115 (1966).
32. Gemmell, D. S., L. L. Lee, Jr., A. Marinov, and J. P. Schiffer, Phys. Rev. 144, 923 (1966).
33. Pilt, A. A., D. M. Sheppard, P. J. Twin, and W. C. Olsen, in Contributions International Conference on Properties of Nuclear States, Montreal, Canada, August, 1969, Univ. of Montreal Press, (Montreal, Canada, 1969), p. 101.
34. Nuclear Data Sheets, B3, Nos. 3-4 (1970).
35. de-Shalit, A., Phys. Rev. 122, 1530 (1961).
36. Gove, H. E., Phys. Letters 4, 249 (1963).

37. de Pinho, A. G., and J. M. F. Jeronymo, Nucl. Phys. A116, 408 (1968).
38. Larner, D., University of Kansas, Lawrence, Kansas, private communication.
39. Abramowitz, Milton, and Irene A. Stegun, eds., Handbook of Mathematical Functions with Formulas, Graphs, and Mathematical Tables, NBS Appl. Math. Series 55, (Washington, D.C., 1964), p. 887.